n° d'ordre : 2014ISAL0088 Année 2014

THESE

LUBRICATED PISTON RING CYLINDER LINER CONTACT: INFLUENCE OF THE LINER MICROGEOMETRY

présentée devant

L'INSTITUT NATIONAL DES SCIENCES APPLIQUEES DE LYON

pour obtenir

LE GRADE DE DOCTEUR

ECOLE DOCTORALE DES SCIENCES POUR L'INGENIEUR DE LYON :
MECANIQUE, ENERGETIQUE, GENIE CIVIL, ACOUSTIQUE (M.E.G.A.)
SPECIALITE : MECANIQUE

par

Hafedh BOUASSIDA
Ingénieur E.N.I.Tunis

Soutenue le 16 septembre 2014 devant la commission d'examen :

Jury :	**MAZUYER, Denis**	**Professeur**	**Président**
	MONTEIL, Guy	**Professeur**	**Rapporteur**
	FILLON, Michel	**Directeur de recherche**	**Rapporteur**
	TIAN, Tian	**Principal Research Engineer**	**Examinateur**
	BIBOULET, Nans	**Maître de Conférences**	**Examinateur**
	CHARLES, Pierre	**Docteur**	**Invité**
	LUBRECHT, Antonius A.	**Professeur**	**Directeur de thèse**

LaMCoS - UMR CNRS 5514 - INSA de Lyon
20, avenue Albert Einstein, 69621 Villeurbanne Cedex (FRANCE)

Foreword

During my PhD study, I have had support from many people which I would like to thank.

First of all, I profoundly thank my supervisor Pr. Ton Lubrecht for offering me this PhD position and for his constant guidance, help and encouragement throughout this work.

This work is mainly the result of the collaboration between LaMCoS (Contact and Structure Mechanics Laboratory - INSA de Lyon) and PSA Peugeot-Citroen. I would like to thank Pr. Combescure and Pr. Dureisseix for the welcome at LaMCoS. I also would like to thank PSA members: Dr. Cavallaro, Dr. Charles, Mr. El Fassi, Mr. Mermaz Rollet and Dr. Messé for their precious technical and financial aid.

I sincerely thank the jury members: Pr. Mazuyer (LTDS Ecole Centrale de Lyon), Pr. Monteil (Femto-st, ENS2M Besanon), Dr. Fillon (Institut Pprime, CNRS Universit de Poitier), Dr. Tian (Sloan Automotive Laboratory, MIT) and Dr. Charles (PSA) for accepting to evaluate my work.

There are many people who greatly contributed to the completion of this work, particularly Dr. Nans Biboulet who has supported me all along this work not only with valuable comments and suggestions but also with a lot of tips and tricks in coding. Dr. Philippe Sainsot and Mr. Jerôme Cavoret also helped me with measurements and surface analysis. Mr. Drouvin and Mr. Tanguy from Toyota Motorsport GmbH, greatly improved my understanding of PRCL contact with our fruitful discussions. Mrs. Sophie De Oliveira was always ready for assistance. I would like to express my gratitude to them.

I would like to thank the members of the LaMCoS Laboratory, who not only created a pleasant work environment but also gave me lots of support in my work during the last four years: Lamia, Mathieu, Hugo, Florian, Ghizlane, Laure, Amina, Florence, Bachir, Mohamed, Hanfeng, Eliza and Hassen to name but a few.

More generally speaking, I thank wholeheartedly all of my friends and relatives who were always there for me.

Finally, my wholehearted thanks are given to my wife Houda, my parents Souad and Moncef, my brother Hassen and my sister Fatma for their love. They have always supported and helped me in my study and arranged everything in my life.

Résumé

La microgéométrie de la surface de la chemise joue un rôle très important dans les pertes par frottement et dans la consommation de l'huile dans un moteur à combustion interne. Une des texturations classiques de cette surface est celle créée par pierrage. Elle se compose de plateaux plus ou moins lisses et de profondes stries croisées. L'épaisseur du film d'huile est influencée fortement par cette texturation.
Un modèle simplifié du contact segment chemise a été créé en la présence de la microgéométrie. Puis, un code de calcul basé sur la méthode numérique multigrille a été développé. Ce code a été utilisé pour des études paramétriques avec des jeux de paramètres très variés. Les calculs quantifient l'influence de cette microgéométrie particulière sur la relation film d'huile - portance.
Les résultats mettent en évidence deux mécanismes distincts de génération de portance selon le type du segment. Le segment parabolique porte par son convergent et les stries ne font que diminuer cette portance. Inversement, le segment plat ne porte pas et ce sont les stries qui génèrent la portance. Deux modèles de prédiction ont finalement été déduits, un pour les segments paraboliques et un pour les segments plats. Ces deux prédictions ont ensuite été validées par des calculs sur des surfaces mesurées.

Mots clés: Texturation, lubrification hydrodynamique, contact segment-chemise, prédiction

Abstract

The liner microgeometry influences the friction losses and the oil consumption in IC engines. The cross-hatched texturing, created by the honing process, plays an essential part in the load carrying capacity - film thickness relation. This work studies the influence of the cross-hatched groove parameters on the piston ring load carrying capacity.
First, a simplified model of the hydrodynamic contact has been created. Thus a Multigrid based code was developed. Calculations with different sets of microgeometric parameters have been performed. These calculations quantify the load carrying capacity for both parabolic and flat rings.
The results show that the load carrying capacity is generated differently in both cases. For the parabolic case, the pressure is build up by the wedge in the inlet zone and the grooves decrease the global load carrying capacity. In the flat case the grooves generate the total load carrying capacity.
Finally, two prediction models were deduced for the parabolic ring and for the flat ring. These predictions were validated by measured surface calculations.

Keywords: Cross-hatching, hydrodynamic lubrication, PRCL contact, prediction

Contents

Notation

a	Groove depth at the centre[m]
c	z axis dimensionless parameter[m]
d_1	Distance between crossovers in y direction[m]
f	Starvation fit factor[.]
h	Film thickness [m]
h_0	Clearance [m]
h_x	X direction mesh size [.]
h_y	Y direction mesh size [.]
p	Pressure [Pa]
t	Time [s]
u	Velocity[m/s]
u_m	Mean velocity[m/s]
w	Load carrying capacity[N]
w_1	Load carrying capacity per unit length[N/m]
x	Axial coordinate[m]
x_a	Inlet meniscus position[m]
x_b	Outlet position[m]
y_a	Left limit of the domain[m]
y_b	Right limit of the domain[m]
y	circumferential coordinate[m]
A	Dimensionless groove depth [.]
D_1	Dimensionless distance between crossovers in Y direction[.]
H	Dimensionless film thickness[.]
N	Dimensionless distance between two parallel grooves[.]
P	Dimensionless pressure[.]
P_M	Dimensionless maximum pressure[.]
R	Dimensionless groove depth function [.]
R_x	Ring profile radius [m]
T	Dimensionless time[.]
TTS	Total number of the time steps
W	Dimensionless load carrying capacity[.]
W_1	Dimensionless load carrying capacity per unit length[.]
X	Dimensionless axial coordinate (sliding direction) [.]
X_a	Dimensionless inlet meniscus position[.]
X_b	Dimensionless outlet position[.]
Y	Dimensionless circumferential coordinate[.]
Y_a	Dimensionless left limit of the domain[.]
Y_b	Dimensionless right limit of the domain[.]

α	Cross angle[rad]
ϵ	Groove density[.]
η	Fluid viscosity[Pa.s]
λ	Groove width[m]
ω_1	The pressure zone
ω_2	The cavitation zone
ρ	Fluid density[.]
Δ	Single abscissa[.]
Λ	Dimensionless groove width[.]
Ω_1	The pressure zone in dimensionless domain
Ω_2	The cavitation zone in dimensionless domain
Φ	Ring nominal diameter[m]

AS	Analytical Surface
BC	Boundary conditions
BDC	Bottom Dead Center
EHL	ElastoHydrodynamic Lubrication
FT	Film Thickness
HL	Hydrodynamic Lubrication
IC	Internal Combustion
IS	Intermediate Surface
LCC	Load Carrying Capacity
MS	Measured Surface
MST	Mid-STroke
NGOs	Non Governmental Organisations
NOx	mono-Nitrogen Oxides
OCR	Oil Control Ring
PM	Particulate Matter
PN	Particles Number
PRCL	Piston Ring Cylinder Liner
TDC	Top Dead Center
THC	Total Hydro Carbons

Introduction

According to "The International Organization of Motor Vehicle Manufacturers" [1], over 80 millions motor vehicles were produced worldwide in 2012, including passenger cars, light commercial vehicles, heavy trucks, buses and coaches.These vehicles are almost equipped with internal combustion engines (IC engines). The produced engines are subject to particular requirements. In fact, the energy saving is of major concern. Customers and NGOs are more and more hard to please. The engines have to consume increasingly less fuel. As an example, the Global Fuel Economy Initiative[2] aims 4 l/100km by 2030 for light-duty-vehicle oil consumption (halving the 8 value of 2005). Almost 3 % of fuel consumption reduction are needed each year to reach this value. The thermal efficiency is scrutinized and the energy losses are deeply explored by manufacturers. The way to reach these ambitious goals is to increase the engine efficiency. In fact, the efficiency of a diesel engine is only about 29.5% tank to wheel and 22% for spark ignition engines typically gasoline engines [GOS 07].

Figure 1 shows the distribution of the energy losses in a diesel engine. It highlights the im-

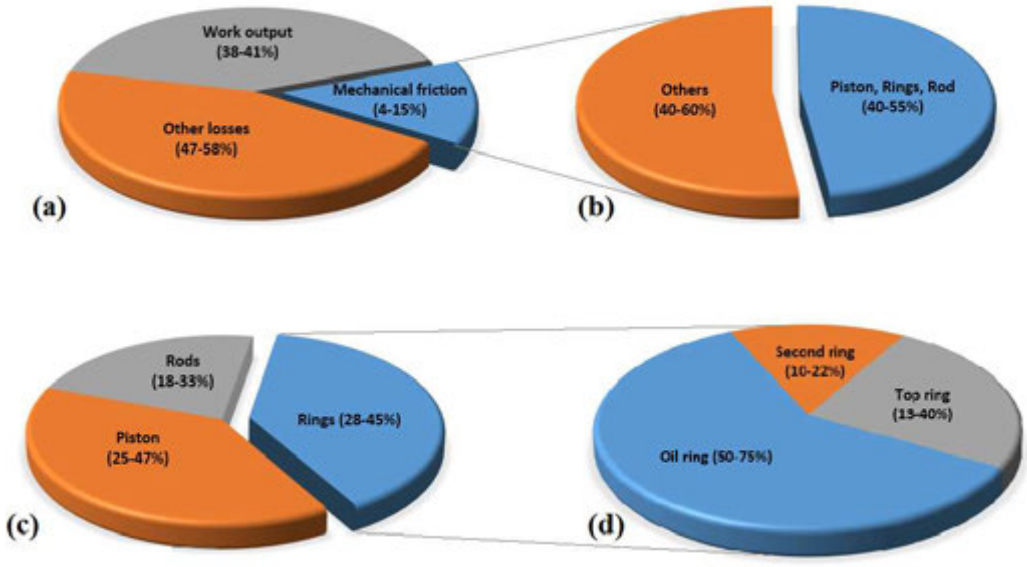

Figure 1: *Energy distribution in a diesel engine:(a) Total energy (b) Mechanical friction (c) Piston, rings and rod friction (d) Rings friction [RIC 00]*

portance of the mechanical friction and then focuses the weight of the piston ring - cylinder

[1] www.oica.net

[2] www.globalfueleconomy.org

liner (PRCL) friction in energy losses. According to this figure, the ring friction removes 0.5 % to 4 % of the engine efficiency. Consequently, reducing the PRCL friction is a straightforward way to increase the tank to wheel efficiency. There are several ways to reduce this friction but they are directly related to the PRCL clearance which means to the lubricant film thickness.

In addition to the energy saving issue, pollution and health are of major concern. The

	NOx		**Tot.HydroCarb.**		**THC+NOx**		**PM**		**PN in**	$\sharp/km$
STAGE & DATE	*Diesel*	*Petrol*	*Diesel*	*Petrol*	*Diesel*	*Petrol*	*Diesel*	*Petrol*	*Diesel*	*Petrol*
Euro 1 07-1992	–	–	–	–	970	970	140	–	–	–
Euro 2 01-1996	–	–	–	–	700/900	500	80/100	–	–	–
Euro 3 01-2000	500	150	–	200	560	–	50	–	–	–
Euro 4 01-2005	250	80	–	100	300	–	25	–	–	–
Euro 5a 09-2009	180	60	–	100	230	–	5	5	–	–
Euro 5b 09-2011	180	60	–	100	230	–	5	5	6e11	–
Euro 6 09-2014	80	60	–	100	170	–	5	5	6e11	–

Table 1: *EU Emission Standards for Passenger Cars in mg/km.*

pollution standards in European legislation [3], as an example, are getting more and more tough toward the car emissions. Table 1 shows clearly that not only the limit line has been approaching the zero emission limit, but also new requirements or criteria are added progressively such as the particle number per kilometre criterion added to the $Euro5$ stage. These emissions come directly from the combustion chamber exhaust which contains notably the combustion by-products, the unburned hydrocarbons and a certain amount of lubricant. A post-treatment does exist. The catalyst converts toxic pollutants to less toxic pollutants by means of redox reaction. However, this solution is expensive due, among others, material cost. Ideally, the pollutants have to be removed from the source which is the combustion chamber and notably the lubricant leakage. The amount of lubricant that is present during combustion has to be reduced. This quantity is controlled by the PRCL clearance.

From above it is clear that, the lubricant film thickness acts directly on both the energetic and the environmental issues. It is important to understand the parameters that are inherent to the film forming (examples: ring shape, rheology, starvation, working conditions ...). The liner microgeometry is a predominant parameter that influences the film thickness and consequently the tribological performance. The liner surface features a special microgeometry. The scope of the thesis is to study the effect of this particular microgeometry on the load carrying capacity - film thickness relation.

A classical texturing is the cross-hatching pattern obtained by the honing process. This texturing is highly directional with two major components: the plateaux and the cross-hatched grooves. The classical parameters as R_a, R_q or valley/peak statistics may be unable to correctly describe this kind of microgeometry. Functional hydrodynamic analysis using statistical methods, notably Patir and Cheng's method, lumps the different components of the surface. There are methods decoupling these components (notably the homogenization method). Another alternative is to use a deterministic model. To correctly describe the roughness, the number of points has to be very large, impacting the computing time.

[3] *www.europa.eu*

Solutions using direct method are not feasible and iterative methods will require a huge computing time. The use of the Multigrid method drastically reduces these calculational costs.
A code based on the multigrid method is developed. It is based on the deterministic model of the PRCL contact. This tool serves to study the influence of microgeometric parameters. The resulting analysis permits one to quantify the importance of each parameter notably on the Load Carrying Capacity(LCC)-Film thickness relation. As a result, the prediction of the LCC is established. It gives an instantaneous approximation of the LCC for a given set of microgemetric parameters and for a range of film thicknesses.
Chapter 1 gives the technical context and enumerates the general considerations concerning the the piston-ring-cylinder-liner contact (PRCL). It introduces the lubrication and focuses particularly on the ring lubrication. The role of the ring pack is explained and the operating conditions are cited. The liner texture is presented and its influence on PRCL contact is shown via the literature.
Chapter 2 deals with the PRCL deterministic modelling and the numerical method that is used (smooth, analytical and measured surfaces). It starts with the geometrical description then the different models that are used. The equations governing the problem are shown. Finally, the multigrid method is introduced.
Chapter 3 studies three PRCL cases: the smooth case, the compression ring lubrication and the oil control ring lubrication. An analytical surface model is used to scrutinise the influence of the microgeometric parameters on lubrication. Predictions of the LCC are obtained.
Chapter 4 links predictions to the real surface measurements.

Chapter 1

Piston Ring Cylinder Liner Contact: State of the Art

Contents

1.1 Introduction

The contact between the piston ring and the cylinder liner is governed by complex laws. In fact, several phenomena occur in this contact impacting the whole behaviour of the engine and consequently its performance. These phenomena are various and are generally related to the geometry and to the operating conditions. Common engines have three rings that are geometrically different. They consequently have different behaviour and carry more or less load. In addition, the cylinder liner surface features a special micro-geometry. This texturing introduces fluctuations in generated pressure and consequently influences the load carrying capacity.
This chapter precedes the detailed study of the PRCL contact, it introduces the technical context and enumerates the general considerations concerning the piston-ring-cylinder-liner (PRCL) contact.
First, the lubrication phenomenon is explained, focusing on the role that it plays in an IC engine. In addition, the oil supply of the PRCL contact is shown. Thus, the hydrodynamic lubrication is briefly explained and the different regimes are clarified via the Stribeck curve.
The second section focuses on the different types of piston rings and their fundamental role in the IC engines. In the last part of this section, the operating conditions are enumerated. Some of the relevant literature that concerns these conditions is cited.
The third section deals with the cylinder liner texture. It explains how the surface is obtained and describes the specificity of its geometry. Finally, it summarizes some of the existing literature on the influence of texturing on the PRCL contact.

1.2 Engine lubrication

1.2.1 Lubrication purpose

Engines contain components that move with respect to one another under a certain load. The friction between these two components generates a great amount of heat and causes damage to the solid surfaces leading to wear or in some cases to failure. The lubricant purpose is primary to minimize the friction between the moving parts, avoiding direct contact between these parts by interposing a substance between the opposing surfaces (Figure 1.1). The interposed substance is a liquid and is called lubricant. Well lubricated surfaces have low levels of friction, heat generation and wear. Lubrication can also be an easy solution to avoid corrosion. It separates the surface from its corrosive environment (through additive action). The lubricant permits a removal of small debris and dust, these contaminants could damage the surfaces. The fluid film lubrication provides the ability to carry loads, to absorb shocks and vibrations. The lubricant is also used as a coolant.
The previous abilities are more or less pronounced for each different contact. Four stroke IC engine oils must fulfil the previous functions and also meet a lot of requirements. Stepina and Veseley [STE 92] and also Mortier and Orszulik [MOR 97] detailed the requirements of such an oil (lubricating power, fluidity, high viscosity, thermal and oxidation stability, engine protection, lubricity...). These requirements are sometimes conflicting. The additives are of great importance for the lubricant. For example, the ZDDP additive is added to enhance the lubricity of the oil (the capacity to carry loads in the boundary regime). In fact, it avoids scuffing occurring generally during the running in process, when the surfaces may come into metal to metal contact and may locally weld.

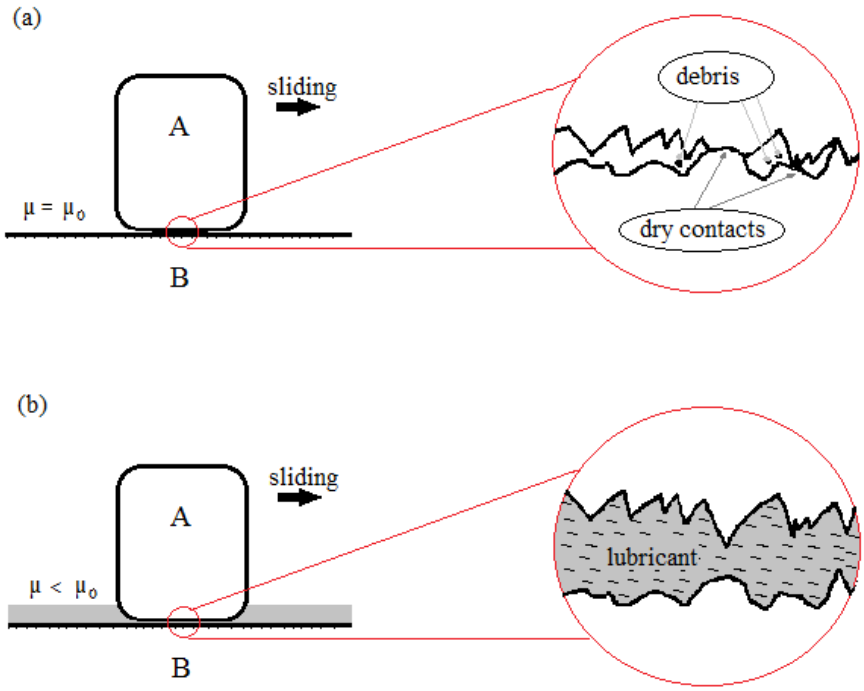

Figure 1.1: *Two bodies A and B in contact (a) Dry contact (b) Lubricated contact.*

1.2.2 Engine lubrication system

The moving parts in an engine (Figure 1.2) require a large amount of lubricant. Oil has to be sent to all of these zones to avoid failure (lubricating and cooling). The oil supply system differs from one engine to another but the principle is the same. Figure 1.3(a) illustrates a classical circuit containing a network of passages, in both the structure of the engine and its individual components. This circuit is the main method to lubricate the bearings, the crankshaft, the camshafts, the valves and sometimes the piston pin (Figure1.3(b)). The cylinder wall and the piston skirt are lubricated by the oil flung of the big end of the connecting rod using the centrifugal force (Figure1.3(c)). Some engines uses several jet spray points to enhance the oil distribution on the wall.

The oil supply to the PRCL contact is not abundant, only a very small quantity reaches the top ring. Moreover this supply is not uniform circumferentially. In fact, the oil flung and the jet spray points do not distribute the lubricant uniformly due to their preferential directions. The rings operate under a starved regime and especially the top ring which is the farthest from the oil supply.

1.2.3 Hydrodynamic lubrication

Nowadays, lubrication is used in a multitude of domains notably in the machine elements like journal bearings, rolling elements, PRCL, cam tappets... The comprehension of the lubrication has permitted a great advance in engine design. To understand lubrication, one has to go back to 1883. In that year independent experimental work by Tower (U.K.) [TOW 83]

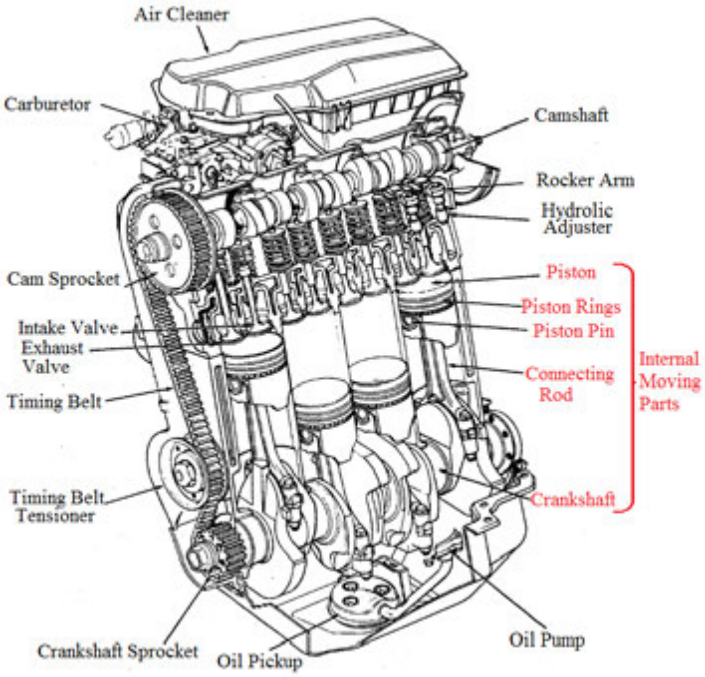

Figure 1.2: *IC Engine: the moving parts [HEY 88]*

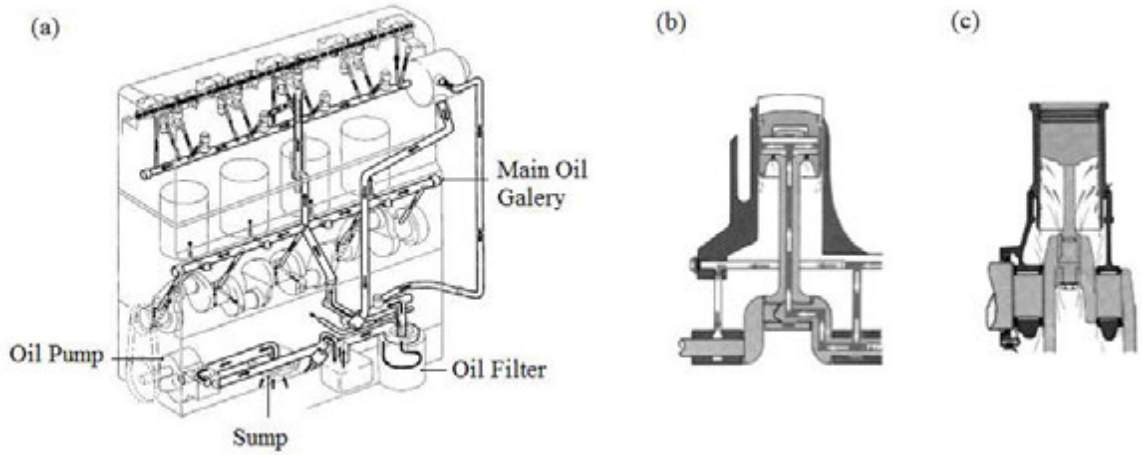

Figure 1.3: *Engine lubrication: (a) Lubrication circuit (b) Internal galleries (c) Oil flung*

and Petrov (Russia) [PET 83], demonstrated the existence of a separating fluid film with substantial pressures in journal bearings. The pressure build up was explained by Reynolds through analytical development about thin films in 1886 [REY 86]. These facts initiated the "Hydrodynamic model" of a lubricated contact. Reynolds derived the fundamental equation of HL from the Navier-Stokes equations through simplifying assumptions. Some of these assumptions are:
- the flow is laminar,
- the fluid is newtonian,
- the fluid is continuous and adheres perfectly to the surface,
- the inertia is negligible,
- the pressure is constant over the film height,
- the bodies are rigid,

The Reynolds equation reads:

$$\underbrace{\frac{\partial}{\partial x}(\frac{\rho h^3}{12\eta}\frac{\partial p}{\partial x}) + \frac{\partial}{\partial y}(\frac{\rho h^3}{12\eta}\frac{\partial p}{\partial y})}_{\text{Poiseuille terms}} - \underbrace{\frac{\partial(u_m \rho h)}{\partial x}}_{\text{Couette term}} - \underbrace{\frac{\partial(\rho h)}{\partial t}}_{\text{Transient term}} = 0 \tag{1.1}$$

Where p is the fluid pressure, h the film thickness, x et y the plane coordinates, ρ is the density, η is the viscosity and u_m the mean body velocity (More details can be found in appendix A).
The first and the second terms of this equation are the Poiseuille terms. They represent the flow due to the pressure gradient. The third term is the Couette term or the wedge term. It is derived from the velocity of both surfaces. The last term, the squeeze, is the transient term. It describes the variation of the film thickness as a function of time.
The Reynolds equation allows the pressure solution p to be negative. In reality, the fluid evaporates when the pressure goes below zero. A discontinuity of the film is created in this zone. It is called the cavitation zone and noted ω_2 [BAY 05] [AUS 13]. The problem becomes the complementary problem, it reads :

$$\begin{cases} \frac{\partial}{\partial x}(\frac{\rho h^3}{12\eta}\frac{\partial p}{\partial x}) + \frac{\partial}{\partial y}(\frac{\rho h^3}{12\eta}\frac{\partial p}{\partial y}) - \frac{\partial(u_m \rho h)}{\partial x} - \frac{\partial(\rho h)}{\partial t} = 0 \, (x,y) \in \omega_1 \\ p = 0 \, (x,y) \in \omega_2 \end{cases} \tag{1.2}$$

ElastoHydrodynamic Lubrication (EHL)
The EHL is based substantially on three phenomena, the first is the hydrodynamic effect described in the previous paragraph. The second one is related to the deformation of the surface. The third is the piezoviscous effect relating the viscosity to pressure. The EHL with a neglected deformation and neglected piezoviscous effects, correspond to the hydrodynamic lubrication regime(HL) .

1.2.4 Stribeck curve

The Stribeck curve defines the lubrication regime of a given contact. It represents the friction coefficient as a function of the dimensionless number $\eta\ u/w$ where η is the fluid viscosity, u is the velocity and w is the normal load (per unit length). Each contact has its own Stribeck curve. Figure 1.4 is an illustration of the curve.

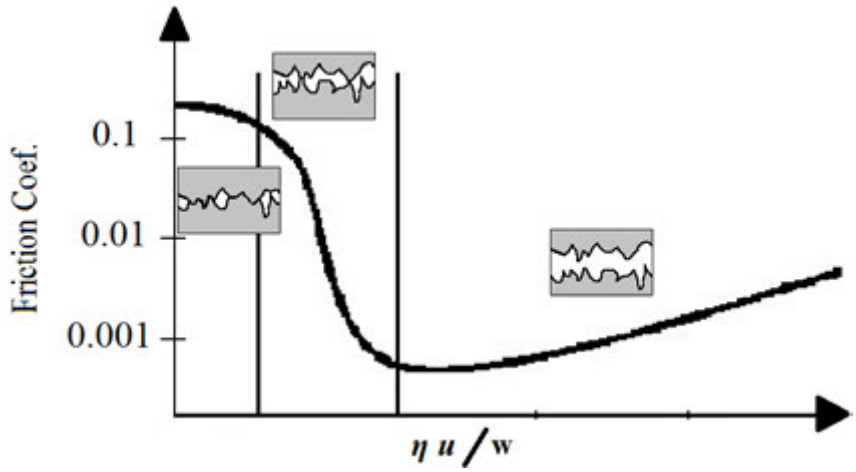

Figure 1.4: *A Stribeck curve with its 3 zones from the left to the right: the boundary regime, the mixed regime and the full film.*

One can distinguish in this curve three zones corresponding to three different lubrication regimes:
- Boundary regime
At low speed, very high load or low viscosity the friction is at its highest value. The regime then is called boundary regime. It is characterised by a high proportion of solid to solid contact. The fluid does not carry any load. This load is entirely supported by the roughness contacts of both solids. The fluid acts as a reservoir for additives
- Mixed regime
Both the asperities and the film carry the load. In the mixed regime the surface roughness plays an essential part, it determines the slope of this part of the curve. In fact, when the surface is smooth the slope becomes high and the transition to the full film zone is fast.
- Full film regime
The load is totally carried by the fluid. The lubrication can be either hydrodynamic or elastohydrodynamic, it depends on the pressure level generated. In fact, the order of magnitude of the maximum pressure is Mega Pascals for the HL against Giga Pascals for the EHL regime.

1.3 Piston rings

1.3.1 The ring pack role

The ring pack has to ensure two main functions:
- **the sealing function**
The combustion gas and the oil sump are the object of sealing. In fact, the unburned fuel and exhaust gas can contaminate the oil through entering the crankcase (blow-by phenomenon). The oil degrades chemically and it loses gradually its ability to lubricate. This sealing function is essentially ensured by the top ring. It avoids also the waste of power due to gas leakage. The oil should not enter the combustion chamber otherwise it burns, creating undesirable combustion results (the environmental constraint). The sealing avoids

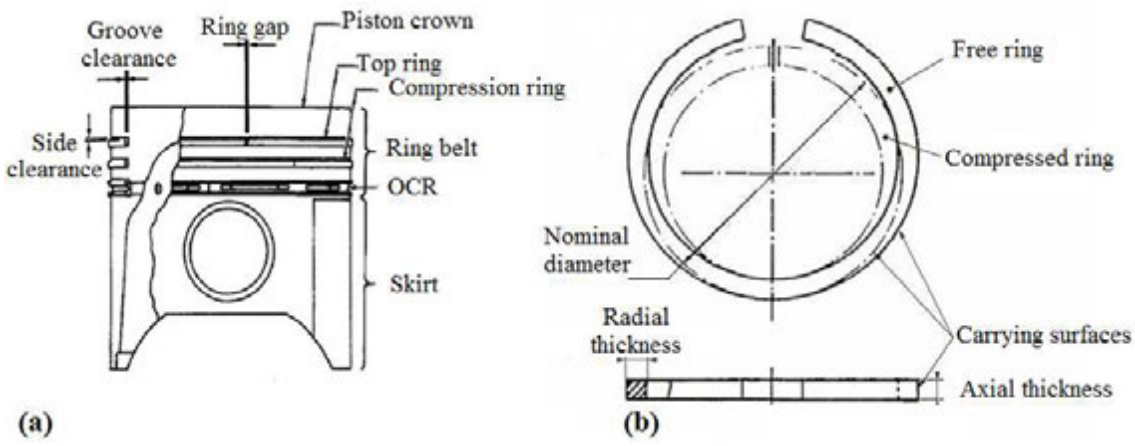

Figure 1.5: *The ring pack: (a) Piston with three rings (b) A ring*

also an over-consumption of oil. The piston ring pack contributes largely to the oil consumption. Complex and coupled phenomena related to this consumption were studied by Yilmaz [YIL 03] and Lecompte [LEC 07].

- the lubrication function

The lubrication has to be maintained when sealing. A minimum oil quantity ensuring lubrication has to reach all the rings. There is a tradeoff between good lubrication and oil consumption (sealing and lubrication functions are contradictory). The oil flow is controlled by the ring pack and especially by the Oil Control Ring (OCR).

1.3.2 The rings

A piston ring is an elastic ring which fits perfectly inside the cylinder by elastic deformation (Figure 1.5(b)). It is placed in a groove in the piston head. In order to enable mounting, a ring gap is provided. The resulting load is the tangential load or pretension and it is noted T. A ring pack contains between 2 and 5 rings but at least one compression ring. The most common car engines contain three rings (Figure 1.5(a)):

- the top ring or the compression ring: its face is in general barrel-shaped or with a rectangular cross-section and it is chrome or molybdenum coated. It ensures the major part of sealing. It faces high temperatures and high pressures during the combustion phase. The pretension for this ring is in general between 5 and 20 N depending on the engine.
- the scraper ring (second compression ring): its profile is rectangular. It ensures more sealing and scrapes some oil at the same time (scraping during down ward motion). Its pretension is between 5 and 30 N.
- the oil control ring: Its geometry is more complex then the other rings. It performs the last task of sealing (or the first regarding the oil). It distributes the oil evenly onto the liner with its slots perforated in the peripheral direction. The oil control rings may have a spring inserted for additional tension to the pre-tension of the ring. The additional force on the oil control rings generates a total pretension of 10 to 60 N.

1.3.3 The operating conditions

1.3.3.1 The oil supply

The oil supply of the ring pack is extremely complex. Each ring is supplied differently. The sealing function forces the rings (notably the compression ring) to function with a limited amount of oil called starvation. The quantity of oil available depends particularly on the oil flows. The oil transport is influenced by multiple factors: the ring gap, the ring groove, the ring geometry, dynamics, liner surface, oil projection on cylinder wall, *etc*...
This problem has been widely studied, one can name the following studies related to oil transport:
- Casey [CAS 98] studied experimentally the oil flow. He concluded that oil transport pathways through gaps and grooves and inertial forces play a significant role.
- Experimental work has been carried out by Thirouard and Tian on oil transport in the ring pack [THI 01][THI 03a][THI 03b]. They used a multiple dye laser induced fluorescence to observe oil displacements in both axial and circumferential directions. The work showed global and detailed oil flows, via a region by region transport analysis.
- Organisciack [ORG 07] uses a starvation model to study the effect of the liner surface finish on oil redistribution. He suggests that the cross-hatched grooves and the discontinuous long grooves are the best microgeometries for good oil redistribution.
- Senzer [SEN 12] focused the oil transport via the OCR groove and the third land oil pattern (region between OCR and flutter ring). He highlighted the importance of the ring design and the operating conditions.

1.3.3.2 Kinematics and dynamics

To evaluate the dynamic effect on a ring, the moving parts have to be considered. Taylor and Dowson detailed the different forces acting on a piston ring [TAY 93]. The main forces acting are:
-the gas pressures behind the ring,
-the normal and tangential forces exerted by the PRCL contact,
-the pretension of the ring,
-the reaction of the piston groove flank (may be cancelled in some cases),
-the inertia of the ring,
-and the axial accelerations.
The reaction of the piston groove flank is sensitive to the dynamic piston tilt (secondary motion), a theoretical model was developed by Tian for a twin land OCR which proves that the minimum oil thickness differ for the two lands especially in both thrust and anti-thrust sides [TIA 00]. Some transient phenomena can interfere on the equilibrium of the ring and on the oil distribution. Tian studied the ring flutter and the radial collapse [TIA 02a][TIA 02b]. He shows how the gas pressures can be redistributed and the stability of the ring changed by modifying small geometrical details. He also shows the importance of the coupling between dynamics and gas flow after a ring loses its axial stability.

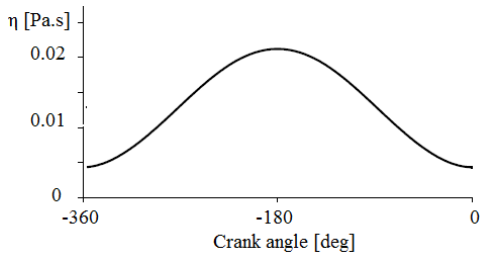

Figure 1.6: *Typical viscosity along the stroke.*

1.3.3.3 Temperature

The temperature on the cylinder wall varies and consequently the viscosity does inversely (McCoull Walther viscosity temperature chart [MCC 21]). A temperature gradient exists between the top and the bottom of the stroke. A typical viscosity along the stroke is shown in Figure 1.6

1.4 Cylinder liner texture

1.4.1 The process

The honing process (Figure 1.7 (a)) is used in mass production for internal combustion engines. It is the final surface finish using an abrasive finishing process. Small abrasive stones rotate and oscillates creating plateaued surfaces (example in Figure 1.7 (b)). This process has been widely used for mass production in IC engines. Other processes, namely laser texturing [ETS 05] [VIN 08], are used for more advanced engines. These processes have the advantage to be more flexible in defining the micro geometry.

1.4.2 Surface description

The honing process gives the cylinder liner a special surface texturing. It features a special micro geometry, with plateaux and cross-hatched grooves. Figure 1.8 (a) shows a new liner cut-up. The liner surface is totally honed and the cross hatching pattern is evenly distributed. On the run-in surface (1.8 $(b), (c)$) the plateaux are smoother. Measurements (Figure 1.8 $(d), (e), (f)$) show that the cross hatching parameters differ. In fact, the width, the depth of the grooves varies and discontinuities may occur. Reynolds equation remains valid for this kind of grooves, since the groove width is very large compared with the depth ($cf.$ Organisciack [ORG 07] and Dobrica *etal.* [DOB 09]). The marking feature of this surface is the directionality. Figure 1.8 (g) shows two preferential directions.

1.4.3 The influence of the texture

The texturing acts as a micro-bearing, oil reservoir and debris trap [ETS 05]. These functions are crucial to avoid failure. Many experimental works on the influence of textured surfaced have been carried out over the previous years. They permit a better understanding but sometimes they are contradictory.

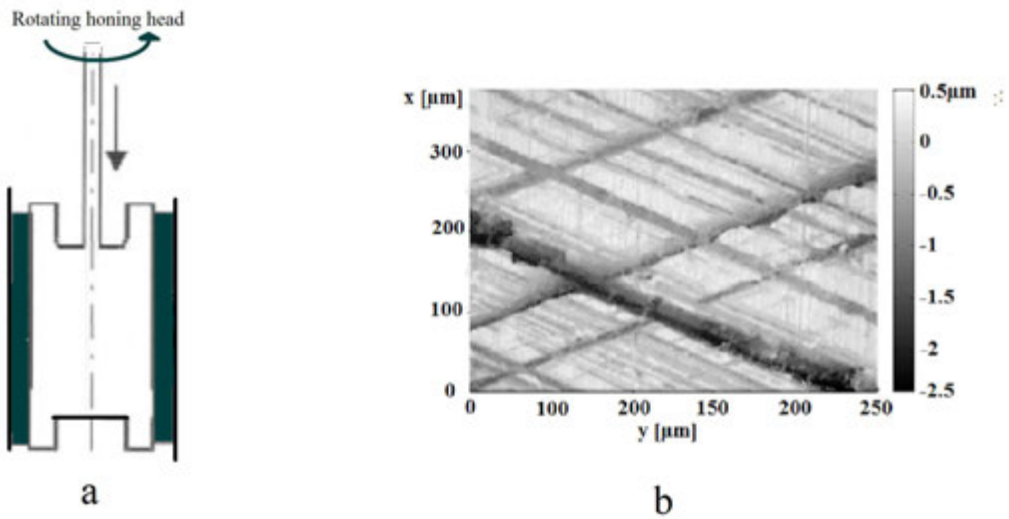

Figure 1.7: *(a) Schematic representation of the honing process (b) Typical measured honed surface*

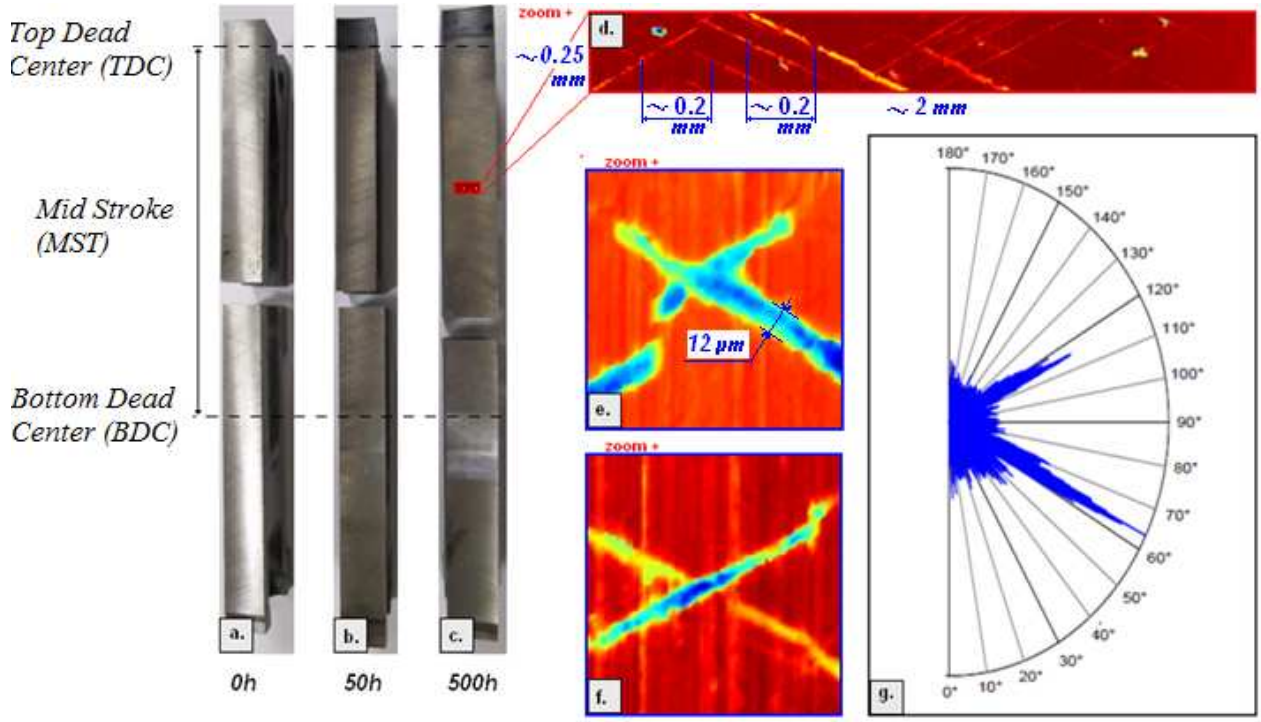

Figure 1.8: *(a) New liner cut up (b) 50 hours running liner cut up (c) 500 hours running liner cut up (d) Measured surface (e) cross-hatched groove (f) cross-hatched groove (g) Preferential directions of the grooves*

Theorically, different approaches to deal with the influence of the texture are found in the literature. The first one is the stochastic approach. It is based on the random hypothesis of the roughness. Patir and Cheng [PAT 78] [PAT 79] have initiated this method which permits to derive an averaged Reynolds equation. In fact, the average influence of the roughness in a direction is reflected by a flow factor in that direction. The flow factors are determined by precalculations. This method has permitted to take into account the surface texturing with a fast approximation. In 1980, Rohde [ROH 80] presented a two-dimensions contact model of a rough liner and calculated for a whole cycle. He highlighted the effect of the roughness on the friction. Michail and Barber [MIC 95a][MIC 95b], using flow factors, assert that for the same operating conditions, angles below 45 degrees enhance the hydrodynamic effect by increasing the film thickness. Bolander et al. [BOL 05] correlated experimental results using Patir and Cheng model [PAT 78] [PAT 79]. They identified lubrication regime transition areas. Tian and Wong [TIA 00] inserted this model in a more complicated system and studied dynamic effects considering the piston tilt. Many works are based on the flow factor model, namely the work of Takata [TAK 06a][TAK 06b] for dimples action for large bore IC engines, McClure [MCC 07] on the secondary motion of the piston... This approach lumps the different components of the surface (grooves and plateaux) and does not consider the roughness directionality.
Methods decoupling both components (grooves and plateaux), like the homogenization method [BAY 05] [ALM 11] are also used. Spencer [SPE 10] coupled the homogenization method with the flow factor method.
Another alternative is to use a deterministic model of measured surfaces. This method is based on direct measurements of the liner. Caciu [CAC 06] filtered the micro-geometry and did not consider the curvature of the ring. Organisciak [ORG 07] studied the effect of starvation without considering the roughness on plateaux. He suggests to use narrower and denser cross-hatched grooves for better redistribution of the lubricant and to reduce friction. Pascovici *et al.* [PAS 09] investigated the partially textured surface effect. They highlighted the potential of the partial texturing in the lift off effect (contributing to the load carrying capacity). Dobrica *et al.* [DOB 10] demonstrated, using dimples, the importance of the grooves parameters and their aspect in pressure generation. They concluded that the full texturing can generate hydrodynamic lift for parallel surfaces while it has a negative effect for convergent plane-inclined surfaces. They also concluded that the texture effect seems proportional to the texturing density. Dobrica *et al.* [DOB 12] simulated scratched journal bearings. They performed a parametric study and concluded that the deeper / denser / more numerous the scratches, the poorer the bearing performance. Chen [CHE 08] [CHE 11] correlated experimental results with a deterministic model. He highlighted the importance of the roughness in the load carrying capacity for the flat ring. For the compression rings he found that the liner microgeometry is as important as the ring profile and the starvation degree.

1.5 Conclusion

This chapter presented the environment of the piston ring cylinder liner (PRCL) contact and enumerated the different phenomena that act on its tribological performance. These phenomena are various and are extremely coupled. The chapter started by presenting the engine lubrication, focusing on the role that it plays in an IC engine. The lubrication regimes

were explained and the Stribeck curve shown. The second part of the chapter was dedicated to the rings. It highlighted the importance of these rings and the role that they play in lubrication and sealing at the same time, functions that are contradictory. Thus, some of the important operating conditions were enumerated such as the oil supply and the dynamics. The last part of the chapter showed the surface finish of the liner, second part of the PRCL contact. The literature was scrutinized to sum up the different models and results inherent to PRCL contact. These results are important in the understanding of the microgeometry effect on lubrication but only few studies deal with the texture effects in PRCL contact and especially the quantification and generalisation of the effect of the classical cross hatching parameters. The results in the next chapters contributes to the understanding of this effect whilst predicting the load carrying capacity - film thickness relation as a function of the cross hatching parameters.

Chapter 2

Deterministic modelling and numerical method

Contents

2.1 Introduction

A full understanding of the phenomena taking part in the PRCL contact is necessary to enhance the contact performance. This understanding is established through modelling. Modelling is the art of transforming a real complex problem to "simple" mathematics. Modelling requires a precise knowledge of the real geometries and the real operating conditions, presented in Chapter 1. Chapter 2 links the previous chapter to the following ones.
The first section presents the different models used in Chapters 3 and 4. Many simplified models are created corresponding to the main objective which is the understanding of the influence of the microgeometry. This first section contains the different assumptions involved in the PRCL contact model. It describes also how the rings and the liner are modelled, leading to equations governing the problem. Generally in lubricated contact problems three equations are obtained:
- the Reynolds equation describing the lubricant flow,
- the film thickness equation describing the geometry including the ring and the liner surface,
- the force balance equation which is the fundamental equation of mechanics.
The second section of the chapter is dedicated to the numerical tool, the key to solve the mathematical problem. First, the dimensionless equations are derived. Then the problem is discretized to obtain the numerical formulation. The numerical tool is based on the multigrid method. The multigrid method permits a fast and efficient transient calculation. The basics of this method are explained. Finally, the calculational algorithm is presented and an example of calculation is shown.

2.2 Model

2.2.1 General assumptions

Generally the PRCL contact is assimilated to a hydrodynamic lubricated contact (in contrast with an ElastoHydrodynamic lubricated contact). This fundamental assumption is based on the low pressures generated by low loads. In fact, these pressures generally do not exceed 100 MPa. Consequently, the lubricant density is considered to be constant all over the range of pressures. In addition the temperature is locally constant. The viscosity is then constant too (because of low pressure).
As mentioned in paragraph 1.3.3, the ring is submitted to different loads. All is neglected but the action of normal forces (radial forces). The force balance is quasi static and the only forces acting are
-the ring pretension and the gas pressure behind the ring from a side,
-the load carrying capacity from the other side and the asperity contact resulting force (if considered).
Locally, neglecting the acceleration, the velocity is constant and its direction is x.

2.2.2 Geometric model

2.2.2.1 The domain

The x direction
The contact occurs between the three ring carrying faces and the liner surface (Figure 2.1) .

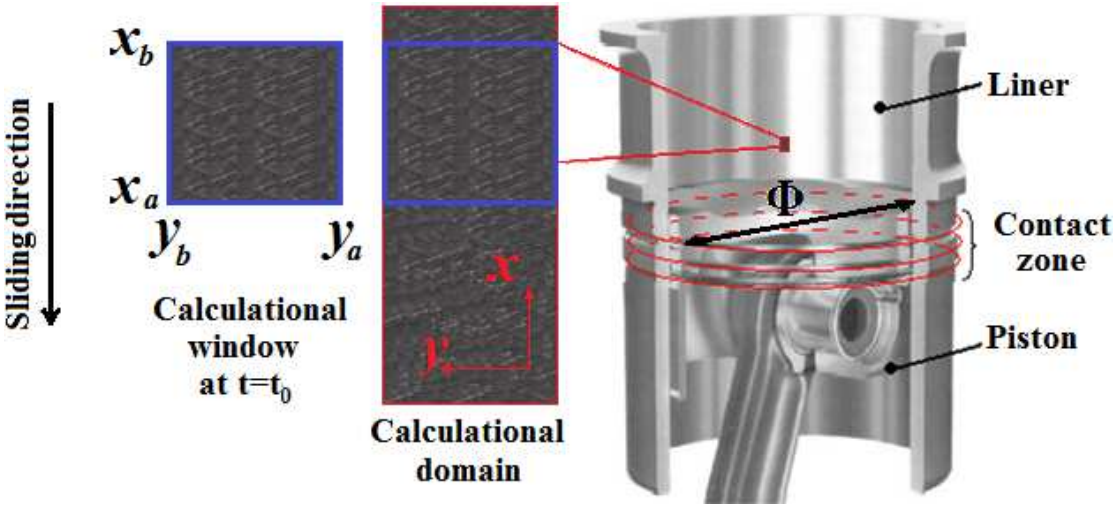

Figure 2.1: *Calculational domain*

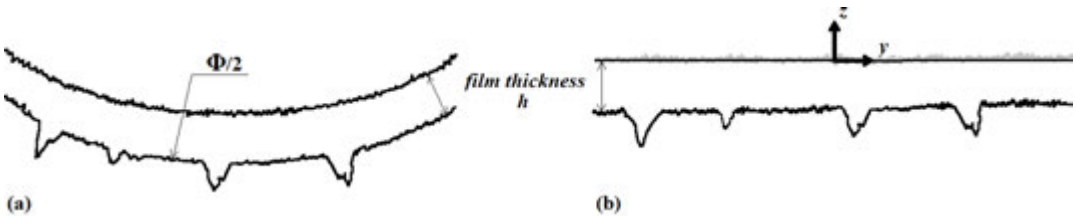

Figure 2.2: *Flattened surface in y direction*

Each of the faces is independent of the others. This contact is time dependent due to the ring sliding motion (x direction). The pressurized zone is then moving. This zone corresponds to the calculational window and is noted $[x_a, x_b]$. x_a is the inlet meniscus position and x_b is the outlet position. x_a and x_b are limited by geometrical considerations which is the ring axial thickness. They can also vary with the starvation degree (cf. paragraph 1.3.3.1). In fact, the amount of available oil can vary along the liner in both directions. It is assumed that x_a corresponds to the starvation degree. The whole calculational domain is the domain where the window is moving for a given short period of time t_f. The initial position is 0 (corresponding to 0 in time) and the last position is x_f (corresponding to t_f). The calculational domain corresponds to a tiny zone of the liner surface. In fact, the period has to be short for two reasons: the first is purely numerical (huge number of points) and the second is for modelling purposes (parameters as the velocity, or the temperature are no longer constant). However, the short period remains sufficient for the main objective which is a local characterisation.

The y direction

The orthoradial direction can be flattened y (Figure2.2). In fact, the film thickness is very small compared to the ring nominal radius $\Phi/2$ allowing such an assumption. Moreover, the conformability of the ring to the liner surface maintains the thin film assumption. The calculation window is $[y_a, y_b]$ in y direction. The values of y_a and y_b depend on the liner surface modelling and the boundary conditions.

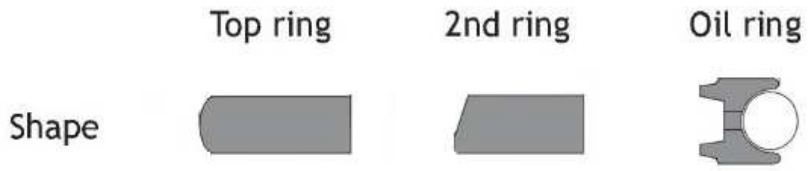

Figure 2.3: *Piston ring shapes*

2.2.2.2 Rings

The rings are perfectly circular, neglecting the end gaps. Figure 2.3 roughly shows the piston ring shapes. The top ring and the second ring are quite similar. Their carrying surface profile is parabolic with a radius of curvature R_x. It ranges between 5 and 25 cm.

The twin land OCR has two carrying surfaces. Both of them are considered flat. In fact their radius are about 10 m.

The three rings have smooth surfaces, their surface roughness is neglected.

2.2.2.3 Liner surface

Paragraph 1.4.2 described the liner surface. The cross-hatched surface obtained by honing is modelled in this paragraph. $r(x, y)$ expresses the microgeometry of the surface. Three models are kept for use: the measured surface, the analytical model of the surface and the smooth surface.

The measured surface

A $Sensofar$® microscope with a confocal objective is used to measure the surface. The $\times 50$ magnification allows $1mm^2$ measurements with a high accuracy. In fact, beyond this area of $1mm^2$ two main problems occur:

-Stitching become difficult. It consists of automatically overlapping pieces of $200 \times 200\mu m$ measured, obtaining the $1mm^2$ surface.

-The number of points measured becomes very large (larger than 9 000 000).

A magnification lower than $\times 50$ would solve the previous problems. Unfortunately, the maximum slope that can be measured by a such lower magnification diminishes. Consequently the grooves, would be poorly measured.

Considering the dimensions of the measurement and knowing that the ring conforms in the y direction, one can neglect the curvature in the y direction. Consequently the surfaces are flattened, the macro-curvature is not considered. Figure 2.4 shows two measured surfaces, the resulting useful surface and the removed macro-curvature. The macro-curvature in this figure is due to measurement (parallelism between the objective and the measured surface) and the initial y curvature.

$r(x, y)$ corresponds to the measurement values if (x, y) coincides with the measured point. Otherwise it corresponds to the interpolated value of the nearest four measured points.

The analytical surface

The measured surface contains smooth plateaux and relatively regular grooves (at least anglewise). The analytical model admits both assumptions: the perfectly smooth plateaux and the regular grooves. Only four parameters describe a full pattern:

-α the half angle (called angle to simplify),

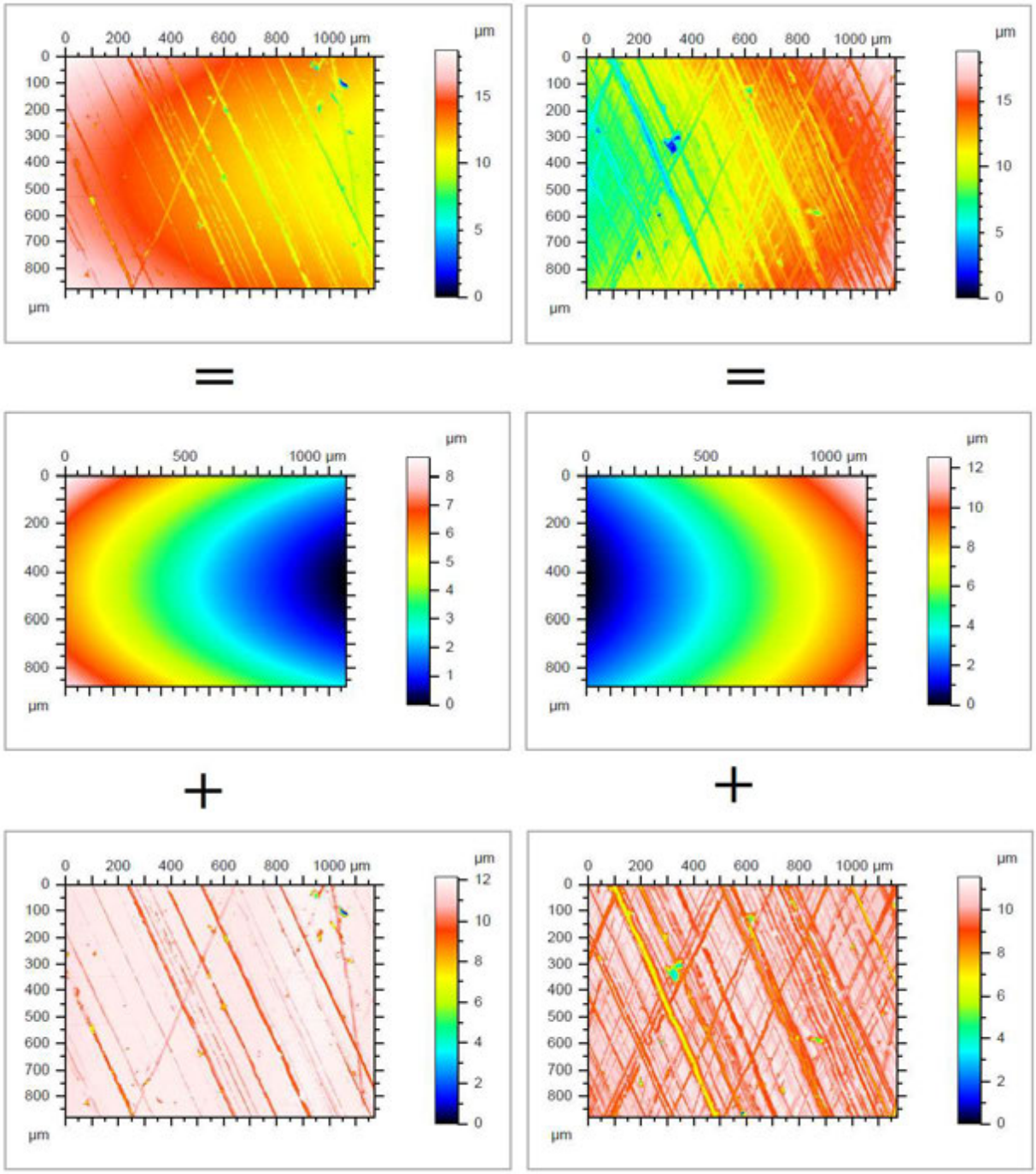

Figure 2.4: *Flattened measured rough surfaces*

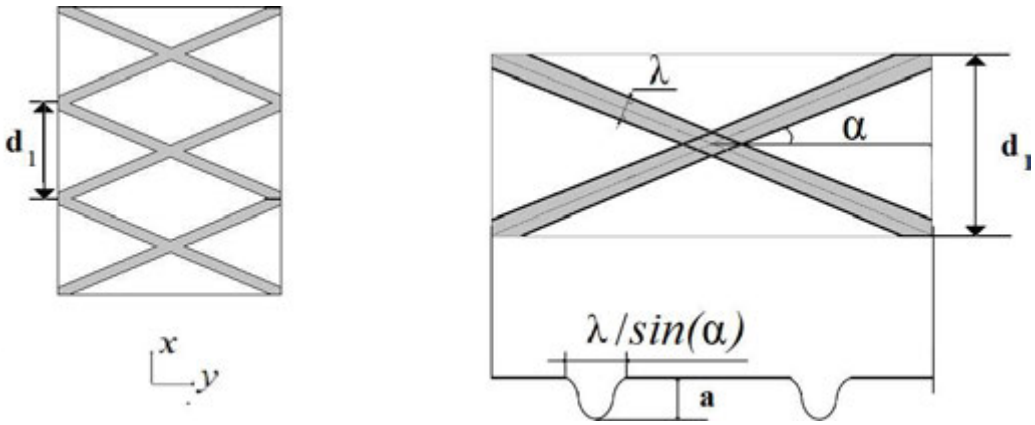

Figure 2.5: *Cross hatching pattern*

-λ the groove width,
-a the groove maximum depth (called depth to simplify),
-d_1 the distance between the cross-overs in x direction defining the density of the grooves.
The grooves are sinusoidally shaped. Figure 2.5 shows the geometry of the cross-hatching pattern and the parameters. $r(x, y)$ defines the surface topography.

$$\begin{cases} r\left(x,y,t\right) = \dfrac{-a}{2}\left[\cos\left(\dfrac{2\pi}{\lambda}|x\cos\alpha \pm y\sin\alpha|\cos\alpha\right)+1\right] \\ \quad if \quad |x\cos\alpha \pm y\sin\alpha|\cos\alpha < \dfrac{\lambda}{2} \\ r\left(x,y,t\right) = 0 \\ \quad elsewhere \end{cases} \tag{2.1}$$

Smooth surface
$r(x, y)$ is zero everywhere, this surface is simply taken as a reference, since the results of this surface are easy to obtain or already known.

2.2.3 Equations

2.2.3.1 Film thickness equation

Figure 2.6 regroups the ring model and the surface model. The film thickness at each point (x, y) is the sum of three terms:
- the nominal film thickness h_0 which is constant unless in imposed load mode,
- the ring profile for the x position, which is $x^2/(2R_x)$ for a parabolic shaped ring and zero for the flat one,
- the $r(x, y, t)$ term explained in subsection 2.2.2.3 .
The film thickness equation reads:

$$h\left(x,y,t\right) = h_0\left(t\right) + \frac{x^2}{2R_x} + r\left(x,y,t\right) \tag{2.2}$$

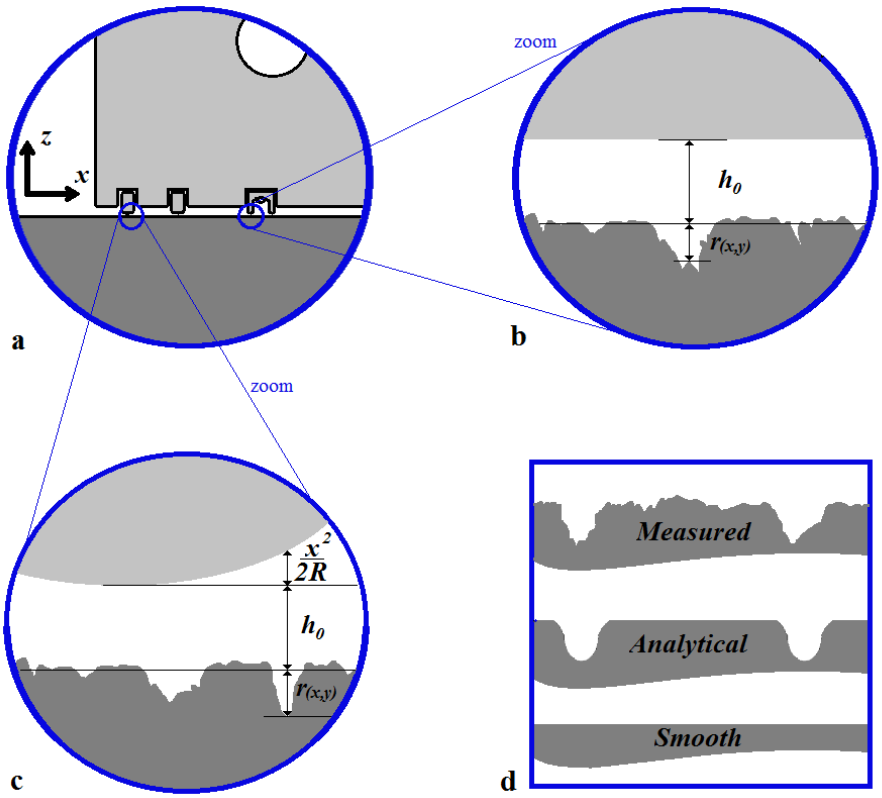

Figure 2.6: *The film thickness (a) Three ring contact (b) OCR film (c) Top ring film (d) Liner surfaces*

2.2.3.2 Reynolds equation

Considering the general assumptions, equation 1.2 representing the Reynolds equation and the complementary problem becomes

$$\begin{cases} \frac{1}{12\eta}\frac{\partial}{\partial x}(h^3\frac{\partial p}{\partial x}) + \frac{1}{12\eta}\frac{\partial}{\partial y}(h^3\frac{\partial p}{\partial y}) - u_m\frac{\partial h}{\partial x} - \frac{\partial h}{\partial t} = 0 \quad (x,y) \in \omega_1 \\ p = 0 \quad (x,y) \in \omega_2 \end{cases} \tag{2.3}$$

2.2.3.3 Boundary conditions

The boundary conditions in the x direction are Dirichlet conditions. This means that $p(x_a) = p(x_b) = 0$. In fact, the pressures on both sides of the ring are equal to the pressure of the lubricant saturated vapour. This means that these pressures are negligible compared to the contact pressure and considered nil. In the y direction either periodic conditions or Dirichlet conditions are imposed. In the first case $p(y_a) = p(y_b)$ and for the second $p(y_a) = p(y_b) = 0$. Periodic conditions are used in case of periodic analytical surfaces. For measured surfaces the periodic conditions can not be applied due to the geometry. Imposing Dirichlet conditions can be justified by the fact that geometrical irregularities like very deep longitudinal grooves can occur at those boundary creating a zero pressure condition. Furthermore, if sufficiently distant these BC do not influence the central zone (further explanation will be provided in Paragraph 4.3.1).

2.2.3.4 Force balance equation

The force balance equation represents the load equilibrium. The applied load is balanced by the pressure which is generated on the surfaces.

$$\iint_{\omega=\omega_1\cup\omega_2} p\,(x,y,t)\ \mathrm{d}x\ \mathrm{d}y = w(t) \tag{2.4}$$

w is the resulting normal force and is expressed in N. The normal force per unit length in the y direction is w_1 which is the normal force divided by the width of the calculational window $y_b - y_a$ (Figure 2.1) .

$$w_1 = \frac{w}{(y_b - y_a)} \tag{2.5}$$

To have an order of magnitude and considering the action of the pretension force T only, w_1 reads [BRU 86]:

$$w_1 = \frac{T}{\Phi/2} \tag{2.6}$$

2.2.3.5 Dimensionless equations

The equations are solved using dimensionless variables for two main reasons:
- first, the dimensionless parameters enable one to obtain variables of the order of magnitude of 1 which is crucial for numerical precision,

- second, they enable one to use the opportunity of similarity groups.
The dimensionless variables read

$$X = \frac{x}{x^*} \tag{2.7}$$

$$Y = \frac{y}{x^*} \tag{2.8}$$

$$H = \frac{h}{h^*} \tag{2.9}$$

$$P = \frac{p}{p^*} \tag{2.10}$$

$$W_1 = \frac{w_1}{w_1^*} \tag{2.11}$$

The choice of the appropriate set of dimensionless parameters depends on the studied case. The table 2.1 resumes the different dimensionless parameters used in the four following cases:
- case 1: the measured surface and the ring is parabolic,
- case 2: the analytical surface and the ring is parabolic,
- case 3: the measured surface and the ring is flat,
- case 4: the analytical surface and the ring is flat.

	h^*	x^*	p^*	t^*	w_1^*
Case 1	c	$\sqrt{R_x c}$	$12\eta u_m\sqrt{R_x}/c\sqrt{c}$	$u_m/\sqrt{R_x c}$	$12\eta u_m R_x/c$
Case 2	h_0	$\sqrt{R_x h_0}$	$12\eta u_m\sqrt{R_x}/h_0\sqrt{h_0}$	$u_m/\sqrt{R_x h_0}$	$12\eta u_m R_x/h_0$
Case 3	c	λ	$12\eta u_m\lambda/c^2$	u_m/λ	$12\eta u_m\lambda^2/c^2$
Case 4	h_0	λ	$12\eta u_m\lambda/h_0^2$	u_m/λ	$12\eta u_m\lambda^2/h_0^2$

Table 2.1: *Dimensionless parameters*

The z-axis dimensionless parameter c make the film thickness and the groove depth dimensionless. The order of magnitude of these last physical parameters is $1\mu m$. Thus, the value of c is chosen $1\mu m$.
In all the cases the Reynolds equation 2.3 becomes:

$$\begin{cases} \dfrac{\partial}{\partial X}(H^3\dfrac{\partial P}{\partial X}) + \dfrac{\partial}{\partial Y}(H^3\dfrac{\partial P}{\partial Y}) - \dfrac{\partial H}{\partial X} - \dfrac{\partial H}{\partial T} = 0 \quad (X,Y) \in \Omega_1 \\ P = 0 \quad (X,Y) \in \Omega_2 \end{cases} \tag{2.12}$$

The force balance equation is the same for the four cases. It reads

$$W_1 = \frac{\iint_\Omega P\,(X,Y,T)\ \mathrm{d}X\ \mathrm{d}Y}{(Y_b - Y_a)} \tag{2.13}$$

The film thickness is different depending on cases:
- case 1:

$$H = H_0 + \frac{X^2}{2} - R \tag{2.14}$$

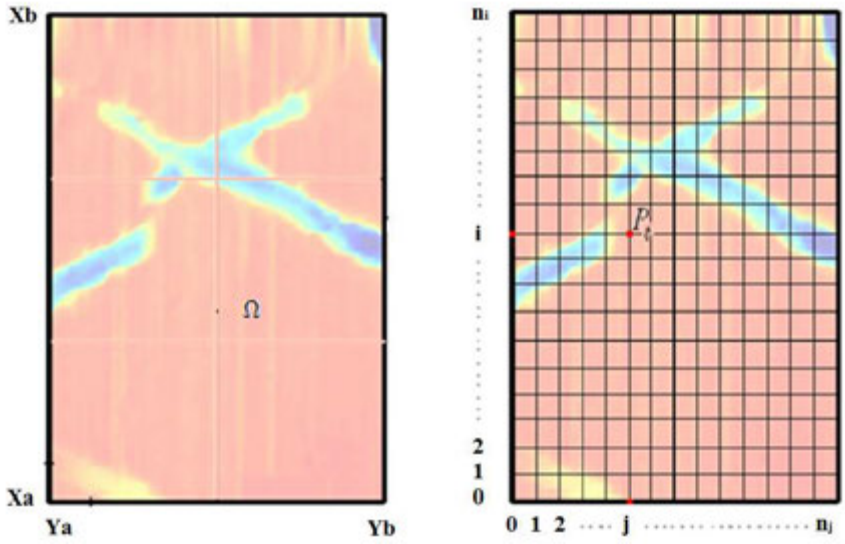

Figure 2.7: *The discretized domain*

- case 2:

$$H = 1 + \frac{X^2}{2} - R \tag{2.15}$$

- case 3:

$$H = H_0 - R \tag{2.16}$$

- case 4:

$$H = 1 - R \tag{2.17}$$

2.3 Numerical Method

2.3.1 Discretizing

The discretization phase transforms the continuous physical model to a discrete system. The discretization concerns the geometry then the parameters and consequently the equations. The space represented by the plane (X, Y) is meshed from 0 to n_i for the X direction and from 0 to n_j the Y direction. So there are $(n_i + 1) * (n_j + 1)$ points and $h_x \times h_y$ corresponds to the mesh size (Figure 2.7).

To each point (i, j) corresponds an approximation of P noted P^h_{ij} (h stands for the mesh size with the assumption $h = h_x = h_y$)[1]. P^h is the solution of Reynolds equation. A finite difference method is used to rewrite the Reynolds equation. The term H^3 reads

$$\xi_{i,j} = H^3_{i,j} \tag{2.18}$$

Since the coefficients ξ are strongly variable a harmonic averaging is used to evaluate intermediate points.

$$\frac{1}{\xi^h_{i\pm1/2,j}} = \frac{1}{2}\left[\frac{1}{\xi^h_{i\pm1,j}} + \frac{1}{\xi^h_{i,j}}\right] \tag{2.19}$$

[1] In this section h and H may refer to mesh sizes, not to film thicknesses

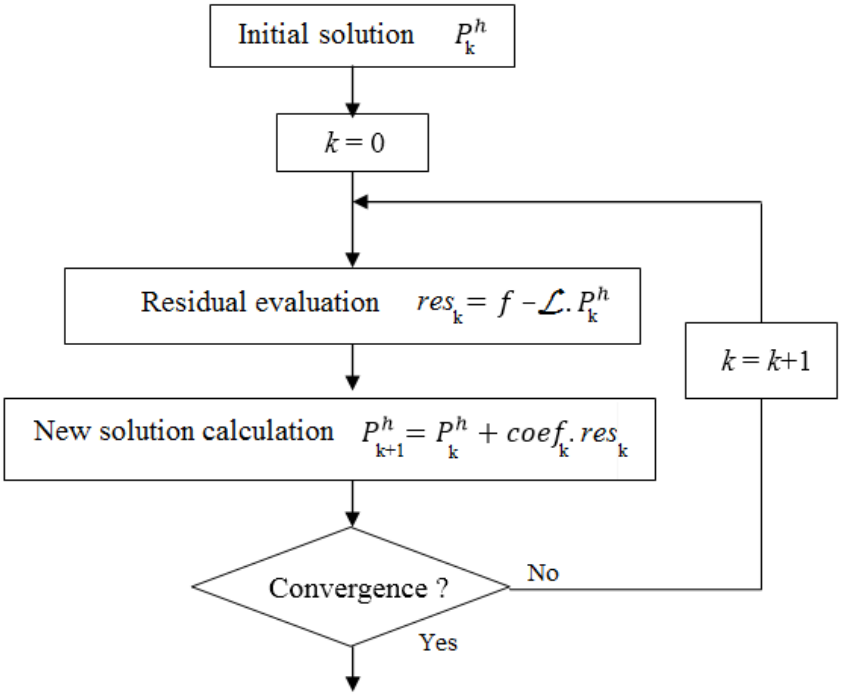

Figure 2.8: *Iterative method*

$$\frac{1}{\xi^h_{i,j\pm1/2}} = \frac{1}{2}\Big[\frac{1}{\xi^h_{i,j\pm1}} + \frac{1}{\xi^h_{i,j}}\Big] \tag{2.20}$$

Using central second order discretization, the stationary Reynolds Equation becomes (cf. [VEN 00])

$$\begin{aligned}\frac{\xi^h_{i+1/2,j}P^h_{i+1,j} - (\xi^h_{i+1/2,j} + \xi^h_{i-1/2,j})P^h_{i,j} + \xi^h_{i-1/2,j}P^h_{i-1,j}}{h_x^2} \\ + \frac{\xi^h_{i,j+1/2}P^h_{i,j+1} - (\xi^h_{i,j+1/2} + \xi^h_{i,j-1/2})P^h_{i,j} + \xi^h_{i,j-1/2}P^h_{i,j-1}}{h_y^2} \\ - \frac{H^h_{i+1,j} - H^h_{i-1,j}}{2h_x} = 0\end{aligned} \tag{2.21}$$

Using the boundary conditions, Equation 2.21 can be written in matrix form as:

$$\mathcal{L}.P^h = r^h \tag{2.22}$$

$\mathcal{L}$ is the operator and r^h is the right hand member (in this case the Couette term). An inversion of $\mathcal{L}$ permits to find the exact P^h solution (direct method such as Gauss pivot). Unfortunately, this method has a huge numerical cost when $n_i \times n_j$ is large. Hence, the system is solved through the use of an iterative method (Figure 2.8).

The iterative method approximates the exact solution iteratively by subtracting a certain amount of the actual solution, proportionally to the residual. The operation of subtracting

is called relaxation. The Gauss-Seidel relaxation is used. From an actual approximation $\tilde{P}^h_{i,j}$, the new approximation $\overline{P}^h_{i,j}$ is derived

$$\overline{P}^h_{i,j} = \tilde{P}^h_{i,j} + \delta^h_{i,j} \tag{2.23}$$

with

$$\delta^h_{i,j} = \frac{-r^h_{i,j}}{(\xi^h_{i+1/2,j} + \xi^h_{i-1/2,j})/h_x^2 + (\xi^h_{i,j+1/2} + \xi^h_{i,j-1/2})/h_y^2} \tag{2.24}$$

and the residual $r^h_{i,j}$ is

$$\begin{aligned} r^h_{i,j} = f^h_{i,j} &- \frac{\xi^h_{i+1/2,j}\tilde{P}^h_{i+1,j} - (\xi^h_{i+1/2,j} + \xi^h_{i-1/2,j})\tilde{P}^h_{i,j} + \xi^h_{i-1/2,j}\overline{P}^h_{i-1,j}}{h_x^2} \\ &- \frac{\xi^h_{i,j+1/2}\tilde{P}^h_{i,j+1} - (\xi^h_{i,j+1/2} + \xi^h_{i,j-1/2})\tilde{P}^h_{i,j} + \xi^h_{i,j-1/2}\overline{P}^h_{i,j-1}}{h_y^2} \\ &+ \frac{H^h_{i+1,j} - H^h_{i-1,j}}{2h_x} \end{aligned} \tag{2.25}$$

The current error is the difference between P^h and $\tilde{P}^h$. With every relaxation sweep this error is reduced. Venner and Lubrecht [VEN 00] indicate that this reduction is grid dependent. The speed of convergence depends on the mesh size h (the larger the h, the faster the convergence). Hence, It is useful to use coarser grids than h to accelerate convergence. This is the purpose of the multigrid method.

2.3.2 Multigrid

2.3.2.1 Introduction

Multigrid methods were developed in the late 70's by Brandt [BRA 77]. Since then Multigrid methods have been widely used and namely in lubrication [BRI 87][VEN 00]. The target is to solve the linear equation 2.22 on the target grid h using multigrid. The multigrid method could be introduced through the coarse grid correction cycle. This cycle contains five steps (Figure 2.9):

- Do ν_1 relaxation sweeps on the target grid h until smoothing the error (the convergence becomes slow). This step is called the pre-relaxation.
- Copy the problem to the coarse grid $H = 2 \times h$ via the transfer operator (restriction).
- Solve the coarse grid problem (eventually using ν_0 relaxations).
- Go back to the target grid, correcting the initial solution via the interpolation of the solved coarse grid problem.
- Do ν_2 relaxation sweeps on the target grid h . This is the post-relaxation.

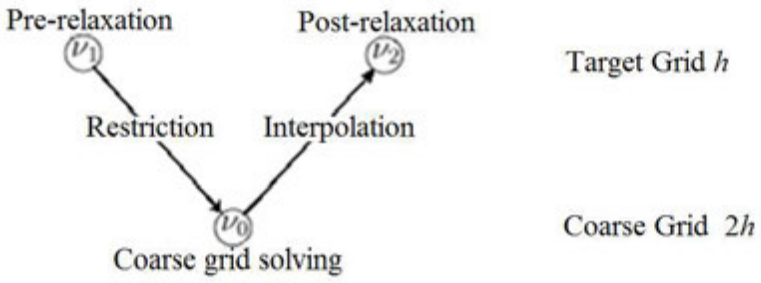

Figure 2.9: *Coarse grid correction cycle*

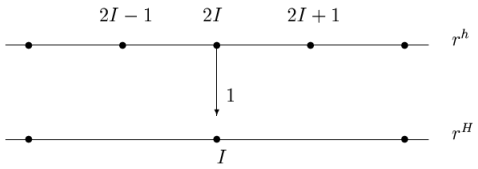

Figure 2.10: *Simple restriction: Injection*

2.3.2.2 Coarse grid correction cycle

Pre-relaxation
The problem reads: $\mathcal{L}^h P^h = f^h$. To simplify the illustration, the problem is assumed linear. Hence, a correction scheme is used. Actually, $\mathcal{L}$ is non linear and a full approximation scheme is used for calculations, *cf.* [VEN 00] for further explanations.
An initial solution P_0^h is introduced and ν_1 relaxations sweeps are performed. The approximation $\tilde{P}^h$ of P^h is obtained. The residual is then calculated $\underline{r}^h = f^h - \mathcal{L}^h \tilde{P}^h$. But $f^h = \mathcal{L}^h P^h$ and the error is $v^h = P^h - \tilde{P}^h$. Thus, $\mathcal{L}^h v^h = \underline{r}^h$.
Restriction
$\mathcal{L}^h v^h = \underline{r}^h$ is transferred to the coarse grid: $\mathcal{L}^H v^h = I_h^H \underline{r}^h$. $\mathcal{L}^H$ is the approximation of $\mathcal{L}^h$ on the coarse grid and I_h^H is the restriction operator.
Generally, two types of restrictions are used : the injection (Figure 2.10)or the full weighting (Figure 2.11).
Coarse grid solving
After the restriction the problem reads: $\mathcal{L}^H v^H = \underline{r}^H$. It can be solved using ν_0 sweeps of relaxations. v^H is obtained.
Interpolation
The initial problem is corrected with the solution v^H. Similar to the restriction, an interpolation operator I_H^h is used. For the coinciding points of both grids, the solution is directly injected from the coarse grid. The intermediate points are interpolated (Figure 2.12). The new target grid solution is $\overline{P}^h = \tilde{P}^h + I_H^h v^H$.
Post-relaxation
Some errors are introduced by the interpolation process. Hence, ν_2 relaxations are performed to eliminate these errors. Finally, an improved approximation is obtained.

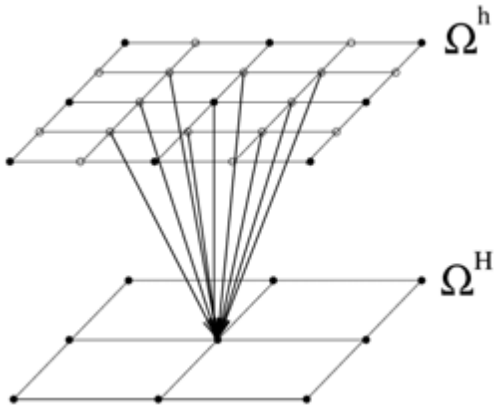

Figure 2.11: *Full weighting restriction*

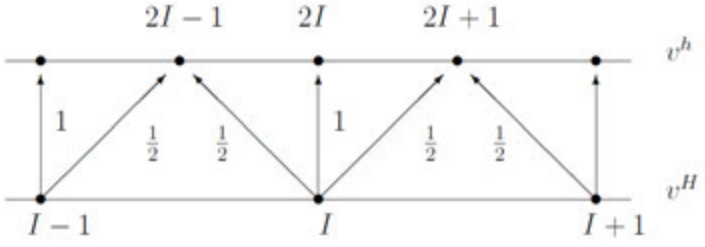

Figure 2.12: *1D linear interpolation stencil*

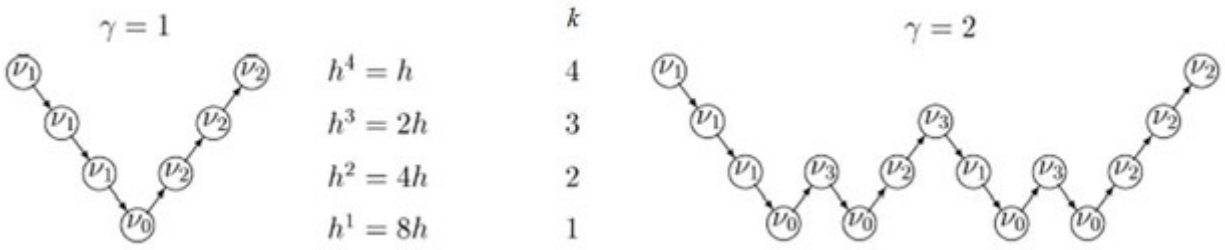

Figure 2.13: *Multigrid schemes: V-cycle and W-cycle*

2.3.2.3 Multilevel cycle

Instead of using two grids, one can use three or more grids. To each level k corresponds a mesh size h^k. $k = 1$ corresponds to the coarsest grid. The multilevel cycle is an algorithm based on recursion [VEN 00]. It reads:

MLC$(k, \nu_1, \nu_2, \gamma)$
If $k > 1$
- perform ν_1 relaxations on the grid k
- restrict to $k - 1$
- do γ times **MLC**$(k - 1, \nu_1, \nu_2, \gamma)$
- interpolate to k
- perform ν_2 relaxations on the grid k

else
- perform ν_0 relaxations

For four levels, Figure 2.13 shows the V cycle for $\gamma = 1$ and the W cycle for $\gamma = 2$.

2.3.3 Calculation algorithm

The developed code is based on successive V-cycles for each time step. The average of the residual over the calculation window on the target grid indicates the convergence and is noted *Res* (Equation 2.26).

$$Res = \Sigma_{i,j} \frac{|res_{i,j}|}{n_i \times n_j} \tag{2.26}$$

The stopping criterion to go to the next time step is $Res < 10^{-5}$. This value ensures a sufficient convergence of the pressure. The algorithm for a measured surface can be written in a simplified way:
Measured surface HL (X_a,X_b,Y_a,Y_b,m_s,max_{lev},ν_1,ν_2)
- create max_{lev} levels
- load measured surface
- interpolate the measured surface on target grid
- Time=0

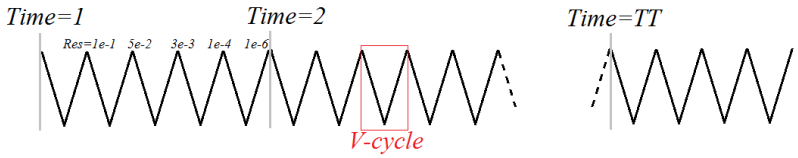

Figure 2.14: *Calculation scheme*

- initialize H(Time)
- for Time=1 to TotalTime
++ Store H in H_{old}
++ Initialize H(Time)
++ Do MLC(max_{lev},ν_1,ν_2,1)
until $Res < 10^{-5}$
- end loop for
- write output files

Figure 2.14 shows a typical calculation scheme.

2.4 Numerical example

In this section, an example of a transient calculation is studied. A parabolic ring slides over a measured patch measuring $1.07 \times 0.8\, mm$. Figure 2.15 shows the surface roughness and the sliding direction. The first case of Table 2.1 shows the dimensionless parameters that are used. Assuming that $c = 1\, \mu m$ and that $R_x = 1\, cm$, a length measuring $100\, \mu m$ corresponds to a 1 dimensionless unit. Thus, the whole domain is 10.70×8.00.

The nominal minimum film thickness, simply called the film thickness, is $h_0 = 0.5\, \mu m$ corresponding to 0.5 dimensionless unit. This value is imposed in all time steps.
A $[-4, 2] \times [-4, 4]$ window represents the zone under pressure (blue boxed in Figure 2.15). The chosen mesh size is $1/128$ in both directions X and Y. Consequently, the nodes number of the finest grid is 769×1025 and the total time steps is $TT = (10.7 - 6)128/2 = 301$. The code calculates the pressure all over the window for each time step. Thus the load carrying capacity (LCC) per unit length is calculated (other quantity can be calculated such as hydrodynamic force [BIB 10a]). Figure 2.16 shows the resulting LCC as a function of the time step T. It shows also the pressure for $T = 1$, 50, 100, 150, 200.

Assuming five levels for the multigrid V cycles solver, the coarsest grid is 49×65. For each level, 8 prerelaxations and 4 postrelaxations are performed, except for the coarsest grid where the problem is "completely" solved with relaxations reducing the residual in this level by a factor of 100 (number limited to 200 relaxations). Figure 2.17 illustrates the V-cycle used for the calculations.

31 hours were necessary for the multigrid code to ensure the desired convergence ($Res < 10^{-5}$) for all the time steps. This computing time is reasonable compared with the one using classical methods. To compare both methods, one has to introduce the work unit [VEN 00]. Assuming that the computing time is proportional to the number of the relaxed points (which is actually not, due to the different operators introduced for particular purposes, more details can be found in appendix B), the work unit is defined as a relaxation sweep. In

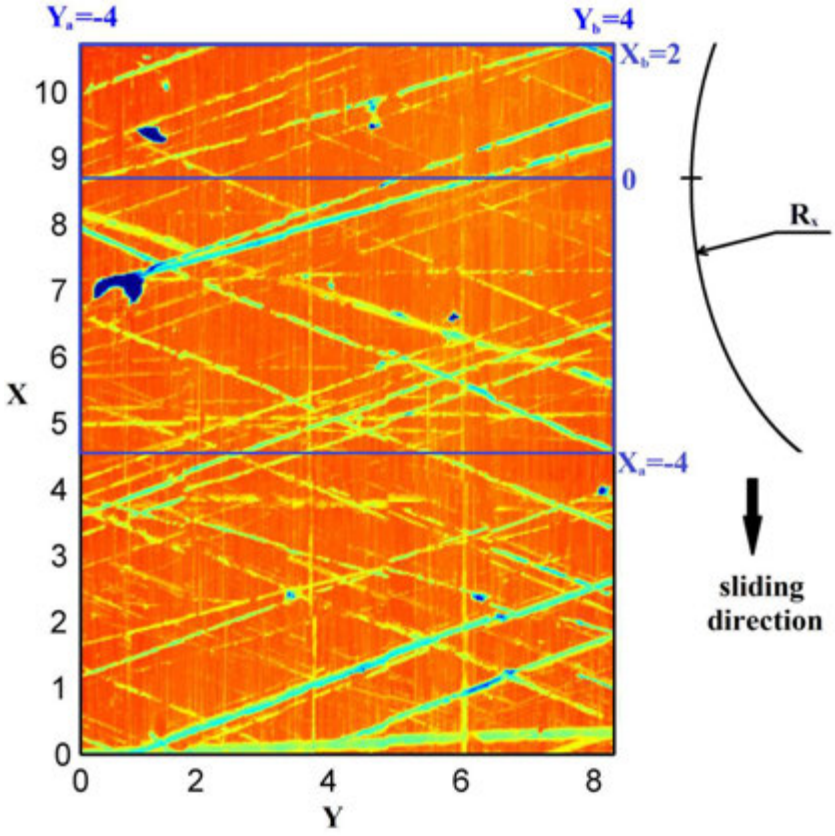

Figure 2.15: *Calculation example: Sliding parabolic ring over a measured surface patch*

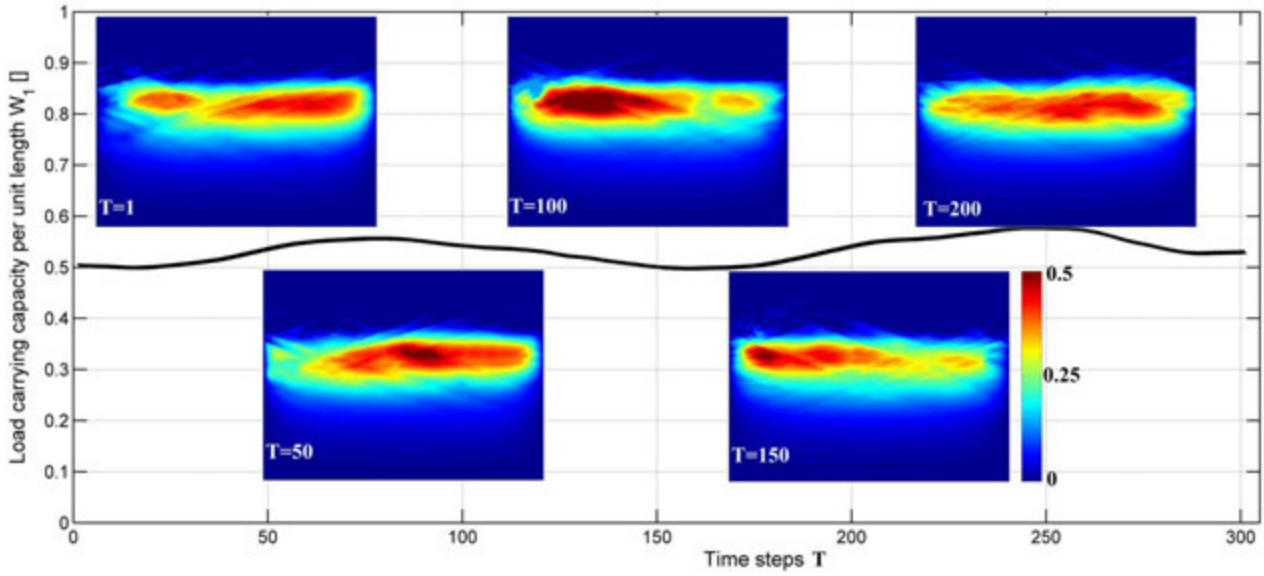

Figure 2.16: *Load carrying capacity per unit length as a function of time with some pressure profiles*

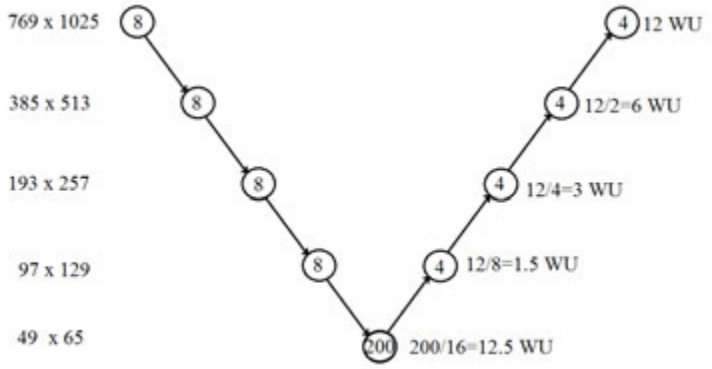

Figure 2.17: *A five levels V-cycle and the corresponding Work units for each grid*

other words, one relaxation of the target grid (769×1025) corresponds to one work unit. A complete V-cycle as presented in Figure 2.17 has 35 work units (WU). The same calculation is done for different number of grids, assuming that for the coarsest grid 200 relaxations are performed. Table 2.2 shows the work units. For a given time step, the comparison between

Max_{lev}	1	2	3	4	5	6	7
WU	200	112	68	46	35	29.5	26.7

Table 2.2: *Work units for different number of grids*

one level grid corresponding to successive relaxations (Gauss Seidel) and more than one level permits one to evaluate the multigrid performance. Figure 2.18 shows the residual recorded at the end of each V-cycle as a function of the work units for different number of grids (7 to 1 from bottom to top). For 600 WU, the four level solver reduces the residual more than 10^6 while Gauss Seidel relaxation reduces it only 10 times. The convergence speed for Multigrid is largely faster. In general, it is clear that the higher the number of grids, the higher the convergence speed.
It seems that one should increase the number of the grids all the time. Actually, the following calculations will be performed with only four grids because of the errors introduced by the coarse grid. In fact, the coarse grid, when it is sufficiently coarse, poorly represents the grooves. Thus, an error is transferred through interpolation and the convergence is not ensured. Not to interpolate locally is a solution for this problem.

2.5 Conclusion

This second chapter concerned the deterministic modelling and the numerical method that will be used in the next chapters. Many assumptions were made to simplify the problem and to focus on the microgeometry influence on hydrodynamic lubrication. Simplified models were created. Thus, the real problem was transformed into equations through the modelling of the geometry and the physical phenomena. Three equations were obtained:
- the Reynolds equation describing the lubricant flow,
- the film thickness equation describing the geometry including the ring and the liner surface,

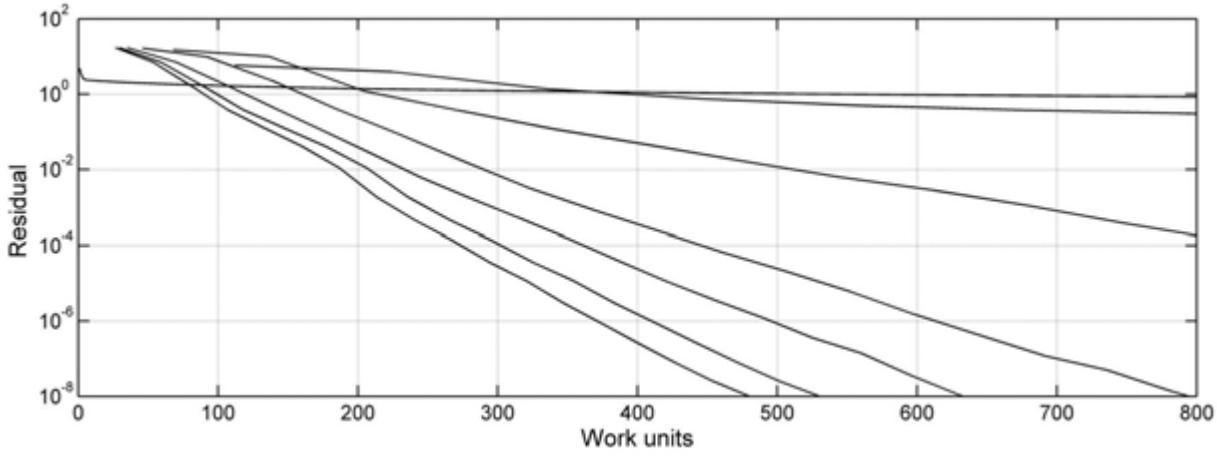

Figure 2.18: *The residual as a function of work units for different number of grids (7 to 1 from bottom to top)*

- the force balance equation which is the fundamental equation of mechanics.

To solve these equations a code was developed based on Multigrid. The use of this method allows one to drastically reduce the computing time allowing a parametric study in the next chapter. The multigrid method was introduced in this chapter. Finally a simplified algorithm of the code is presented and an example is explained.

Chapter 3

Influence of cross-hatched grooves: Load carrying capacity - Film thickness relation

Contents

3.1 Introduction

To optimize the PRCL contact performance, one has to understand the phenomena occurring when the rings are in action. The film thickness is the main parameter, notably to evaluate friction. When looking over the Stribeck curve, one can easily see that the friction can be minimized by having the "right" film thickness. Applying a given load results in a corresponding equilibrium position of the ring. In fact, the film thickness generates enough pressure to sustain the applied load. Thus the load carrying capacity (LCC) - film thickness (FT) relation has to be investigated. The grooves greatly affect the film generation. In fact, the groove parameter dimensions are comparable to the contact dimensions, especially the groove depth that has the same order of magnitude as the FT. The Reynolds equation, the equation governing the film generation, contains a h^3 term explaining this sensitivity to the microgeometry. Two questions are deduced: how do the groove parameters affect the film thickness and by how much?
To answer both questions the models established in Chapter 2 are used. First the smooth surface is investigated without any groove. This case was already studied in both the fully flooded and starved regime by respectively Moes [MOE 00] and Biboulet [BIB 13]. The results are exposed at the beginning of this chapter to serve as references and to validate the developed numerical code.
The second section of this chapter focuses on the top ring with a parabolic shaped profile. More than 2000 transient calculations are performed to explore the effect of the four groove parameters (depth, angle, width and distance between crossovers). At the beginning of this section the objective of these calculations is explained. Then the choice of the mesh size related directly to the calculation accuracy is explained. The results are then exposed, starting with the effect of the depth and then the density. A master parameter Δ is then created, regrouping all the groove parameters. This leads to a single curve regrouping all the results. The master curve quantifies the load carrying capacity in a fixed starvation degree ($X_a = 4$). Finally the effect of the oil starvation degree on the $\Delta - LCC$ relation is investigated and quantified.
The last section of this chapter is dedicated to the oil control ring (OCR). A similar analysis as the top ring is performed.

3.2 Smooth surface

3.2.1 Fully flooded regime

Moes formula
The hydrodynamic lubricated line contact problem has been widely studied in the fully flooded regime. It corresponds to the isoviscous rigid EHL contacts asymptote. A numerical study by Moes [MOE 00] yields the line load as a function of the central film thickness through the following relation.

$$w_1 = 4.896\,\eta u_m R_x / h_0 \tag{3.1}$$

Interpretation
The load carrying capacity per unit length $[N/m]$ w_1 is proportional to the product of the viscosity and the mean velocity and is inversely proportional to the central film thickness

h_0. Figure 3.1 shows the load carrying capacity w_1 as a function of the central film thickness generated by two different ring radii corresponding to the top ring (bottom) and to the OCR (top). Three different conditions are shown in Figure 3.1 corresponding to three extreme

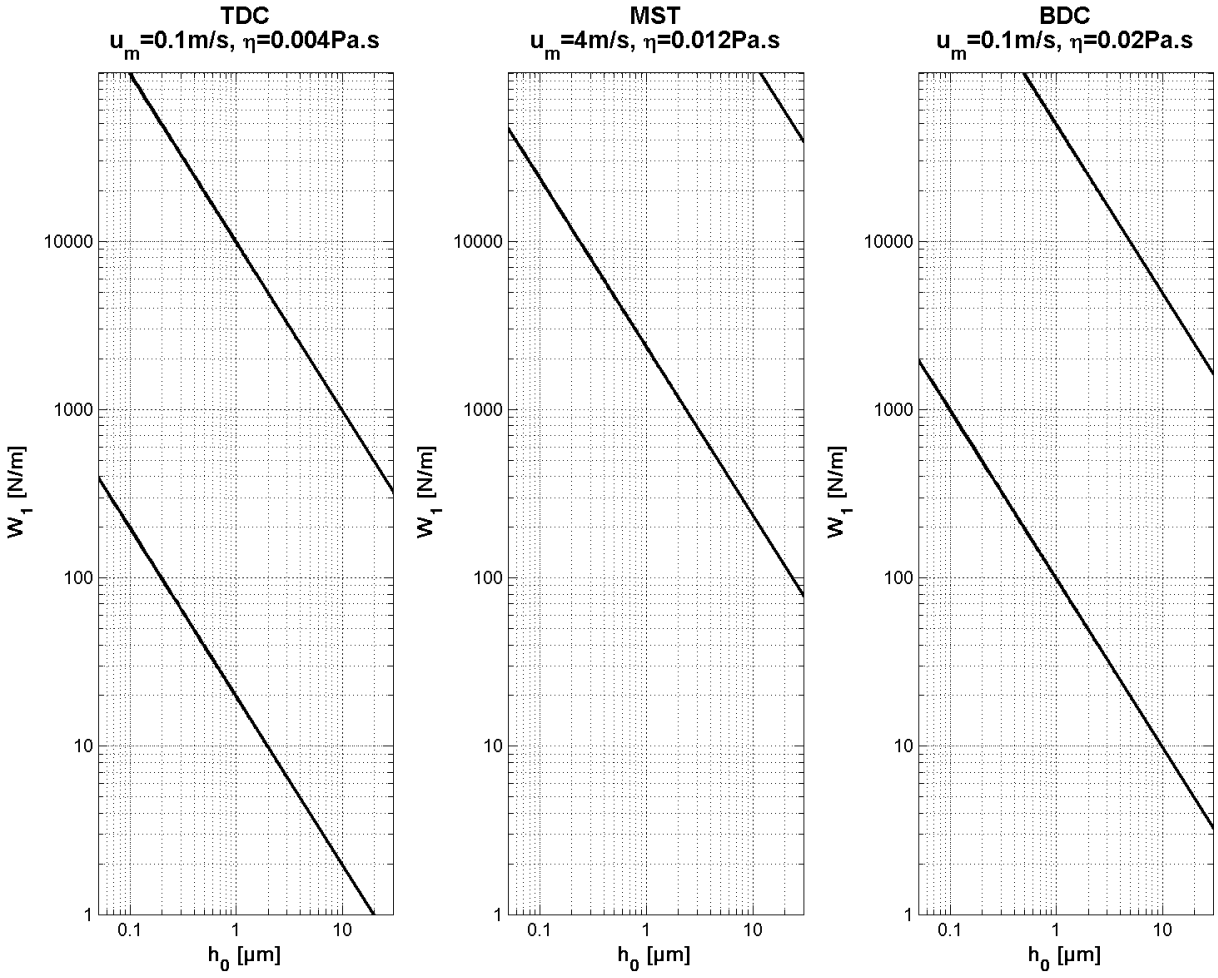

Figure 3.1: *Load carrying capacity per unit length as a function of the film thickness (fully flooded) in three positions: close to Top Dead Center (TDC), MidStroke (MST) and close to Bottom Dead Center (BDC): bottom to top, top ring ($R_x = 10mm$) and OCR ($R_x = 5m$)*

piston positions which are the close to top dead center (TDC), the mid stroke (MST) and the close to bottom dead center (BDC). Due to the temperature gradient, the viscosity η decreases close to TDC. The mean velocity u_m is taken close to zero for TDC and BDC. Table 3.1 shows the different values of η and u_m in these positions.
The load is very high for the fully-flooded model. In fact, the level of $250\,N/m$ corresponds to $10\,N$ of pretension of a ring of $80\,mm$ diameter according to Equation (2.6).
The use of the term $12\eta u_m R_x/h_0$ as the dimensionless parameter for the line load carrying capacity corresponding to the case 2 in Table 2.1 and leads to a simplified form.

$$W_1 = \frac{w_1}{12\eta u_m R_x/h_0} = \frac{4.896\,\eta u_m R_x/h_0}{12\eta u_m R_x/h_0} = 0.408 \tag{3.2}$$

Position	*TDC*	*MST*	*BDC*
η **in Pa.s**	0.004	0.012	0.02
$\mathbf{u_m}$ **in m/s**	0.1	4	0.1

Table 3.1: *Viscosity and velocity at TDC, MST and BDC*

3.2.2 Starved regime

Biboulet *et al.* formula

The fully flooded regime for ring lubrication assumes that the ring is endlessly supplied with oil and that the ring axial thickness is infinitely large (infinite parabola). Actually neither the first assumption nor the second is valid. The starvation is introduced and it acts on relation 3.2 and W_1 is no longer constant. In fact in a completely starved regime, when no oil is available, W_1 is nil. Biboulet et al. [BIB 13] extended relation 3.2 to the starved line contact. The dimensionless relation reads:

$$W_1 = \frac{0.408}{1 + 4.809/X_a^2 + 5.745/X_a^4} \tag{3.3}$$

Interpretation

The dimensionless parameter for x_a is defined as $X_a = x_a/\sqrt{R_x h_0}$. Thus writing in dimensional form w_1 becomes

$$w_1 = \frac{0.408 \times 12\eta u_m R_x}{h_0 + 4.809\, R_x h_0^2/x_a^2 + 5.745\, R_x^2 h_0^3/x_a^4} \tag{3.4}$$

The load in the starved regime remains proportional to the mean velocity and to the viscosity but is no more inversely proportional to h_0. It ranges between inversely proportional to h_0 and inversely proportional to h_0^3. In fact, Equation 3.4 clearly shows that starvation decreases the load carrying capacity. From Equation 3.4, the fully flooded regime corresponds to $x_a = \infty$ and in this case one can find the same expression as 3.1. For very starved conditions, the term with $1/x_a^4$ is predominant and the load becomes inversely proportional to h_0^3. In this case, Equation 3.4 can be simplified to

$$w_1 = \frac{0.852\, \eta u_m x_a^4}{R_x h_0^3} \tag{3.5}$$

Figure 3.2 shows the load w_1 as a function of h_0 as in Figure 3.1 (the six dashed lines in Figure 3.2 are exactly the same lines of Figure 3.1 corresponding to the fully flooded conditions).

Top ring(red lines)

From top to bottom the two solid red lines correspond respectively to $x_a = 1.6\,mm$ and to $x_a = 0.2\,mm$. The first is close to the dashed line that means that 1.6 mm are almost sufficient to obtain fully flooded conditions for a ring radius $R_x = 10mm$. The second line correspond to the starved conditions.

OCR(black lines)

Both black solid lines, corresponding from top to bottom to $x_a = 0.2\,mm$ and to $x_a = 0.1\,mm$ for a ring radius $R_x = 5\,m$, are in very starved conditions. In fact the slope of these lines is approximatively -3 against -1 for the fully flooded regime.

For the OCR, the generated LCC under starved conditions is very low compared with the

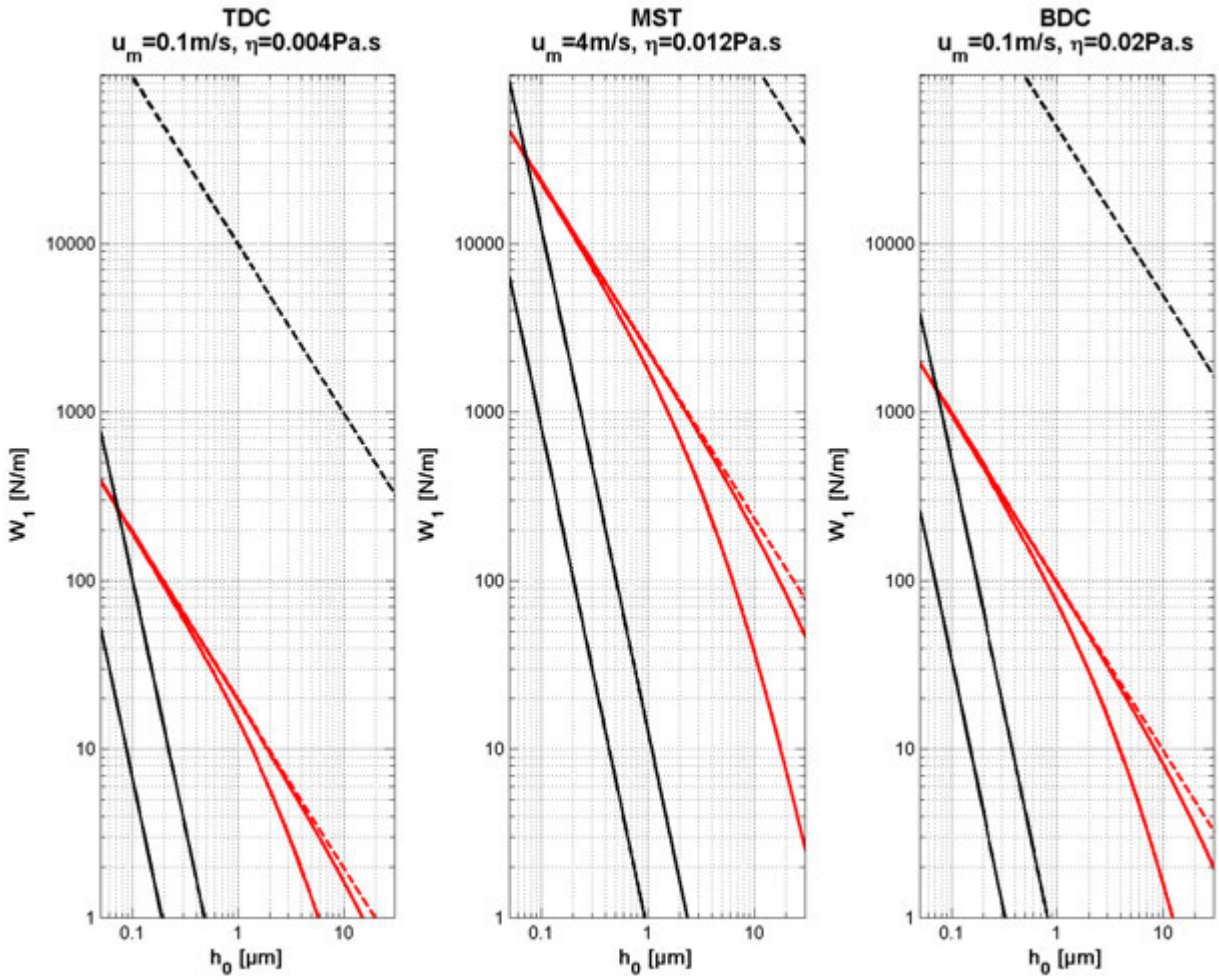

Figure 3.2: *Load carrying capacity per unit length as a function of the film thickness: solid lines (smooth starved) dashed lines (smooth fully flooded), for the top ring in red (bottom to top:* $x_a = 0.2,\ 1.6\,mm$*) and for the OCR in black (bottom to top:* $x_a = 0.1,\ 0.2\,mm$*).*

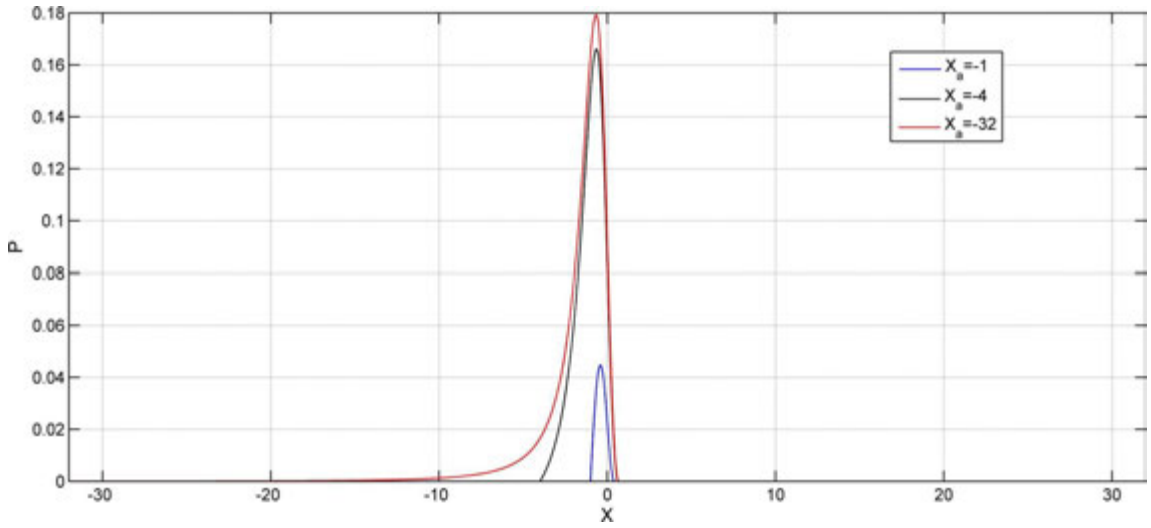

Figure 3.3: *Pressure at the center line Y=0 for a smooth surface with different starvation degree (nearly fully flooded to very starved: $X_a = -32$, $X_a = -4$ and $X_a = -1$)*

fully flooded conditions. In fact, even if the OCR is well supplied with oil, its axial thickness is very thin considering a radius $R_x = 5\,m$. This LCC is also very low compared with the top ring LCC. To sustain the pretension, the film has to be extremely thin ($< 0.1\,\mu m$ close to TDC) which is, actually, not possible in hydrodynamic regime. The metal to metal contact will occur.

3.2.3 Code validation

The developed code, as described in Section 2.3, is a 2D code based on the multigrid method. Given the difficulties of the code implementation, errors may occur. Fortunately, the Biboulet [BIB 13] Equation 3.3 can serve to validate the developed code. To obtain smooth conditions, the roughness is set to zero in the whole domain. The boundary conditions are periodic at Y_a and Y_b and nil for X_a and X_b. Calculations for various degrees of starvation are performed. The pressure at the center line for $Y = 0$ is shown in Figure 3.3 for three different starvation degrees: $X_a = -32$ for a nearly fully flooded case, $X_a = -4$ for an intermediate case and $X_a = -1$ for a very starved case. To validate the developed code, a comparison is made between the results obtained by numerical calculations and the expression 3.3. The calculations shown in Figure 3.4 have a difference less than 0.5% with the Biboulet results which are based on a 1D code (solid line for the expression 3.3 and markers for numerical calculations). These calculations cover a large working domain going from severely starved conditions, corresponding to the left sloped part of the curve, to the fully flooded conditions corresponding to the right horizontal part.

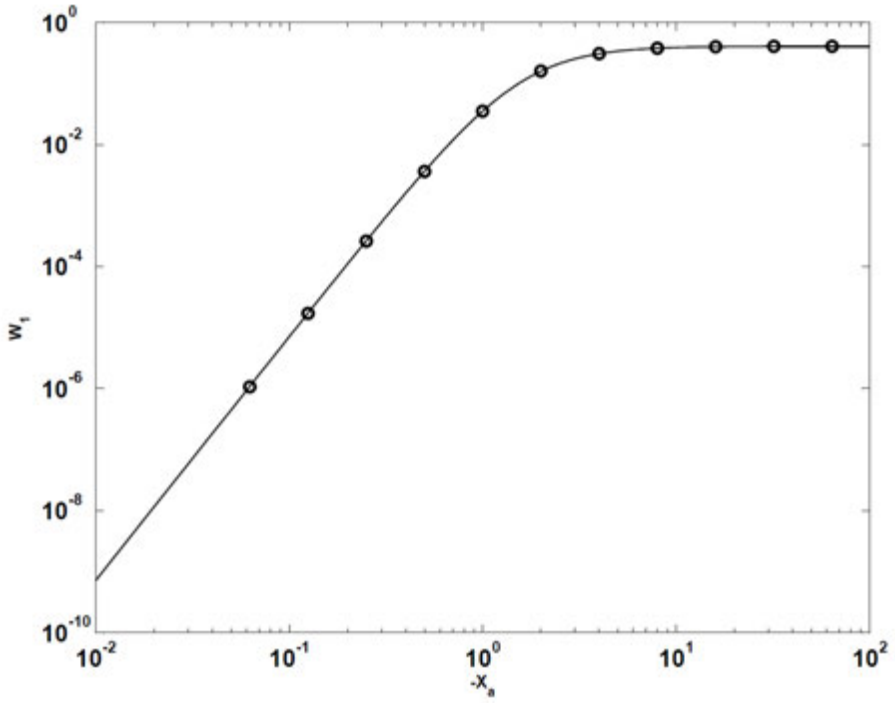

Figure 3.4: *Code validation: Load carrying capacity as a function of the starvation degree: calculation (markers) vs analytical expression (solid line)*

3.3 Top ring: parabolic shape

3.3.1 Objectives

For a parabolic shaped profile, the pressure is build up by the wedge in the inlet zone. The grooves introduce fluctuations in the pressure profile (*cf.* Figure 3.5) causing pressure drops and consequently a global LCC reduction. The objective of this section is to quantify this decrease.

3.3.2 The parameters

The top ring model exposed in Chapter 2 and the analytical surface model are considered. The model is a seven parameters model. That means that these parameter, which are the four microgeometric parameters (*cf.* Figure 2.5), both boundaries of the calculation window X_a and X_b and the time period considered, perfectly describe the problem.
The parameters are dimensionless according to Case 2 of Table 2.1, for instance $A = a/h_0$, $D_1 = d_1/\sqrt{R_x h_0}$, $\Lambda = \lambda/\sqrt{R_x h_0}$, $X_a = x_a/\sqrt{R_x h_0}$ and $X_b = x_b/\sqrt{R_x h_0}$.

3.3.2.1 Time dependency

To reduce the calculation time, two observations are analysed in this paragraph: a perfect periodicity and a known period.
Calculations are performed in the window $[X_a, X_b][Y_a, Y_b]$ for a given period of time. Figure

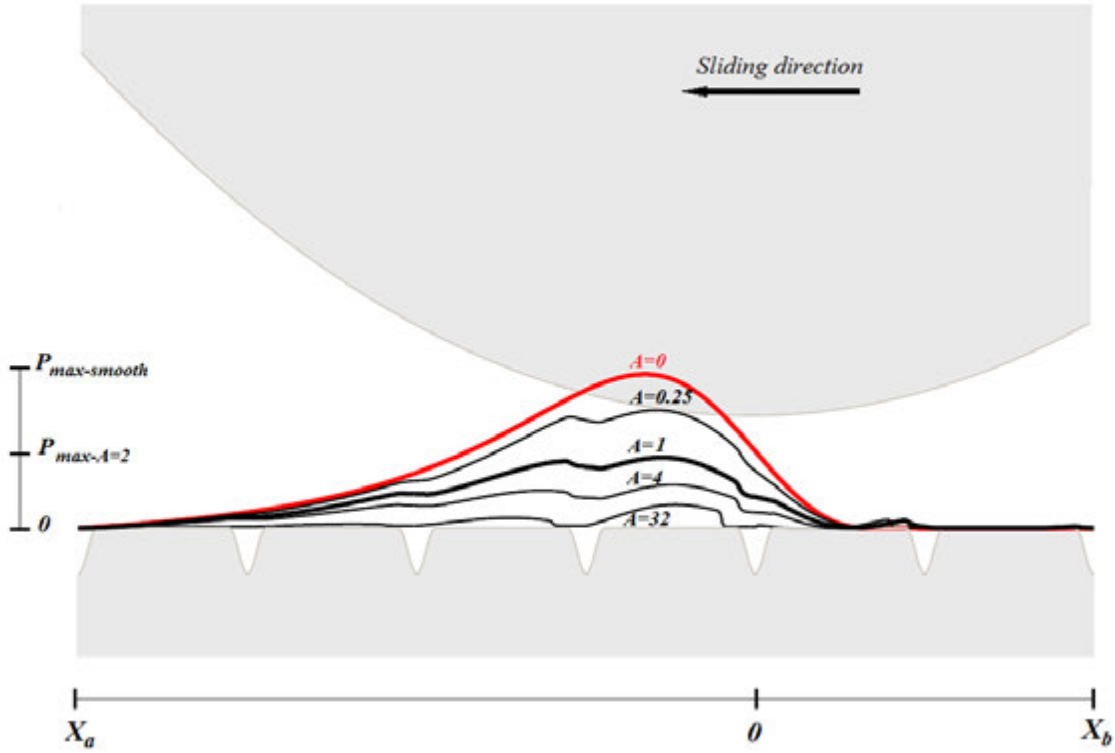

Figure 3.5: *Pressure profile on the center line Y=0: smooth (red) vs grooved (black)*

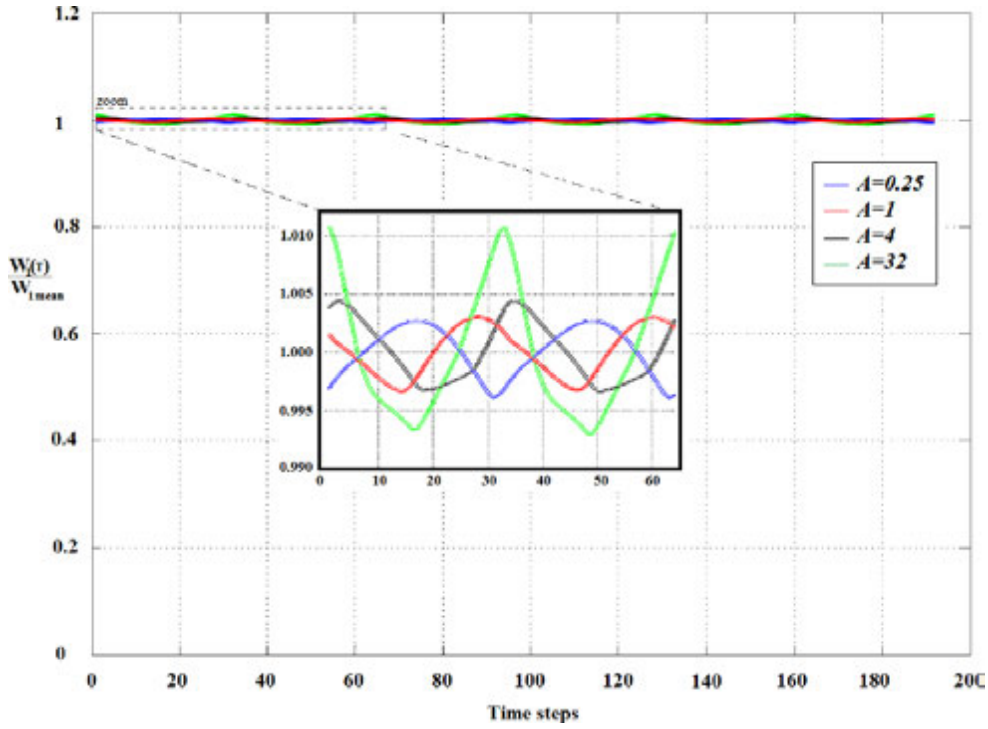

Figure 3.6: *Periodicity of the load carrying capacity over time*

3.6 shows the instantaneous LCC over its mean value for four different groove depths ($A = 1/4, 1, 4, 32$). Variations are relatively small and perfectly periodic. This perfect periodicity is explained by the fact that, the transient term $(H_{i,j}^{old} - H_{i,j})/\Delta T$ is well known since H is imposed. Each time step can be solved independently from the other. In other words, from a crossover to the next which will appear at the same position, the result is the same.

The previous observation suggests that the period is a pattern length (D_1), but actually it is the half of this length. Figure 3.7 shows the pressure profiles all over the period. This period, called TT corresponds exactly to a half pattern length path which means $D_1/2$, in other words half the distance between two consecutive crossovers. In fact, Figure 3.8 clearly shows that the center line of each pressure profile mirrors the right part and the left part. It is the symmetry line of the geometry. That permits to reduce the computing time by two. Knowing that for each time step the ring is moving two meshes h_x, the total number of time steps TTS reads

$$TTS = D_1/(4\,h_x) \tag{3.6}$$

So one can consider a half pattern length problem where the window $[X_a, X_b]$ slides from a position 0 to a position $D_1/2$. The result of each calculation is the pressure profile $P(X, Y, T)$. Integrating the pressure, one obtains the value of the instantaneous line LCC which is $W_1(T)$. Finally the mean value is calculated and is noted simply as W_1.

$$W_1 = \sum_{T=1}^{TTS} \frac{\sum_{j=0}^{jj} \sum_{i=0}^{ii} P_{i,j,T} h_x h_y / (Y_b - Y_a)}{TTS} \tag{3.7}$$

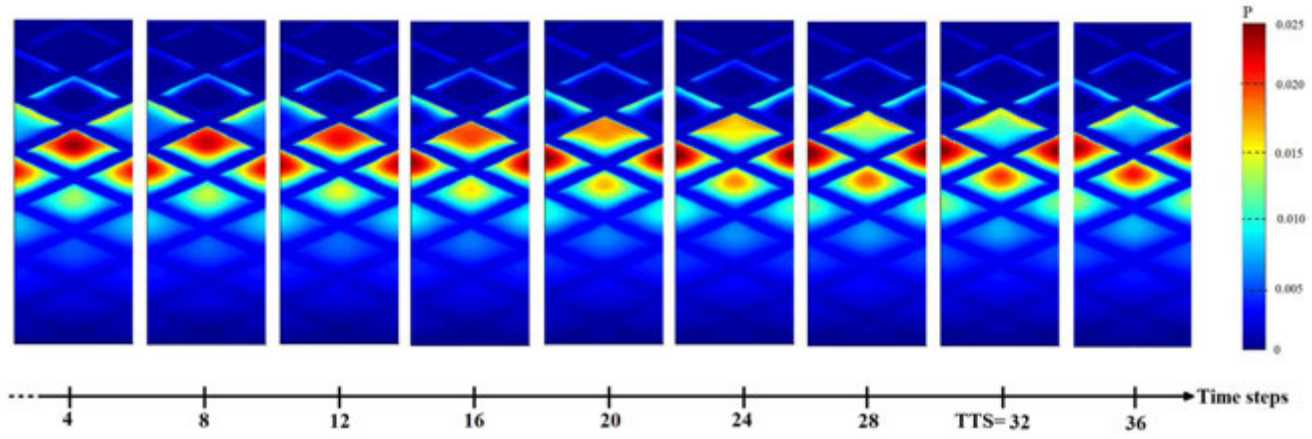

Figure 3.7: *Pressure profiles for* $D_1 = 1$, $\Lambda = 0.2$, $\alpha = 25°$ *and* $A = 0.25, 1, 4, 32$ *for different time steps*

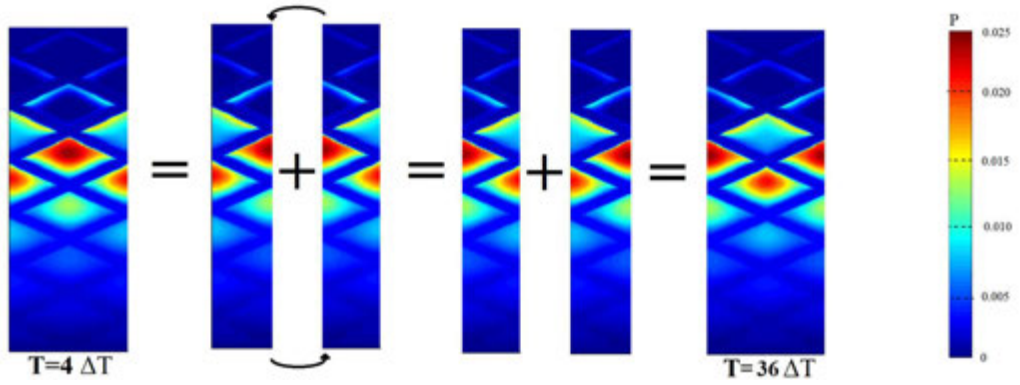

Figure 3.8: *Symmetry in pressure distribution*

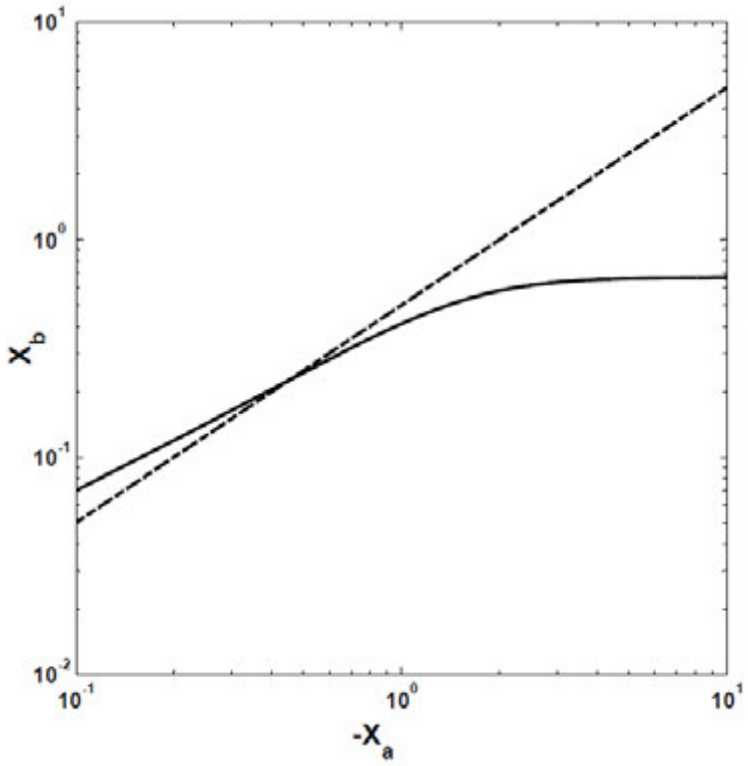

Figure 3.9: *Cavitation abscissa as a function of starvation degree: solid line Equation 3.8, dashed line* $X_b = X_a/2$

3.3.2.2 Eliminating X_b

The relation $X_b = X_a/2$ is assumed. In fact, way before this position, cavitation has already occurred and zero pressure is established. Biboulet *et al.* [BIB13] give the cavitation abscissa as a function of the starvation level for the smooth case.

$$X_b = 0.6719\sqrt{1 - 1/(1 + 0.3418X_a^{3/2} + 0.2533X_a^3)} \tag{3.8}$$

Figure 3.9 shows where the assumption is valid for the smooth case by comparing Equation 3.8 to $X_b = X_a/2$. The assumption is valid for $X_a \geq 0.6$ in the smooth case. In the grooved case, some pressure generation may occur after the cavitation position. For example, at the right of Figure 3.5, there is a small increase of the pressure after the cavitation position due to the presence of grooves. For deep and large grooves they may continue to generate pressure after the fixed X_b position. However, the generated LCC can be neglected compared with the main LCC. In addition, physically, it is not possible to continue generating pressure after the cavitation position [ORG 07].

The problem becomes thus a five parameter problem. The four microgeometric parameters describing the grooves (α, A, Λ and D_1) and the parameter that determines the starvation degree (X_a).

3.3.3 Mesh-size

The numerical accuracy of the computed LCC depends on the mesh choice. The smaller the mesh, the better the approximation. Unfortunately, choosing a very small mesh will naturally

increase the number of points. For example, reducing the mesh size by a factor of 2 will multiply the number of points by 4 and consequently the calculation time at least by 8. Thus an adequate mesh size is a mesh size that guarantees a sufficiently precise approximation in a reasonable calculation time. Table 3.2 compares several mesh sizes for two different cases. A moderate case is chosen with $\Lambda = 0.15$, $A = 4$, $\alpha = 25°$, and $D_1 = 1$. The second case (extreme case) contains very deep grooves, the values are $\Lambda = 0.2$, $A = 32$,$\alpha = 25°$, and $D_1 = 1$. The LCC for each mesh is compared to the 1/384 mesh size taken as a reference (W_{1ref}). A choice that guarantees a good accuracy to time ratio is 128 meshes per length unit. This enables a comparison between results even if in extreme cases (very narrow and/or very deep) the calculations will be less accurate.

Mesh size		**1/24**	**1/48**	**1/96**	**1/128**	**1/192**	**1/384**
Moderate case	W_1	0.248	0.199	0.184	0.182	0.180	0.179
	error	38%	11%	2.8%	1.6%	0.6%	-
Extreme case	W_1	3.02e-1	7.71e-2	2.93e-2	2.30e-2	1.95e-2	1.68e-2
	error	680%	358%	75%	36%	16%	-

Table 3.2: *Accuracy of W_1 for different mesh sizes*

3.3.4 Influence of the groove parameters

3.3.4.1 The parameters choice

The calculation input is formed by five parameters: the four microgeometric parameters describing the grooves (α, A, Λ and D_1) and the parameter that determines the starvation degree (X_a). Figure 3.10 describes these parameters. The output of each calculation is W_1 as described by Equation 3.7.
A first set of calculations is performed for a fixed X_a. The choice of $X_a = -4$ corresponds to a moderately starved condition (Figure 3.4). To give an order of magnitude, this value corresponds to $x_b - x_a = 600\mu m$ for $R_x = 10mm$ and $h_0 = 1\mu m$.
To cover a large domain, the depth range is from 2^{-3} to 2^4, doubling each time the value. This gives 8 values. The angle varies between 10° and 40° with a step of 5°. The pair (Λ, D_1) has 36 different values. Figure 3.11 shows the distribution of these cross-hatching parameters. This leads to a total number of calculations of 2016.

3.3.4.2 Groove depth

The depth A is a major parameter for the pressure drop. Figure 3.12 shows that for small A values the pressure profile resembles a smooth line hydrodynamic pressure profile, the fluctuations are small with almost parallel horizontal lines (for isobar lines). For deeper grooves the straight horizontal lines start to disappear giving way to a diamond shape. The diamonds correspond to the groove footprint. For the rightmost profile, where the depth is 32, the pressure is only build up on the plateaux.
The resulting relative LCC is analysed for various cases. Figure 3.13 shows the relative LCC W_1/W_{1s} (s for smooth) as a function of $1/A$ for $D_1 = 1$ (blue) and $D_1 = 2$ (red), $\alpha = 25°$ and for three values of Λ 0.025 (circles), 0.1 (squares) and 0.2 (triangles). The

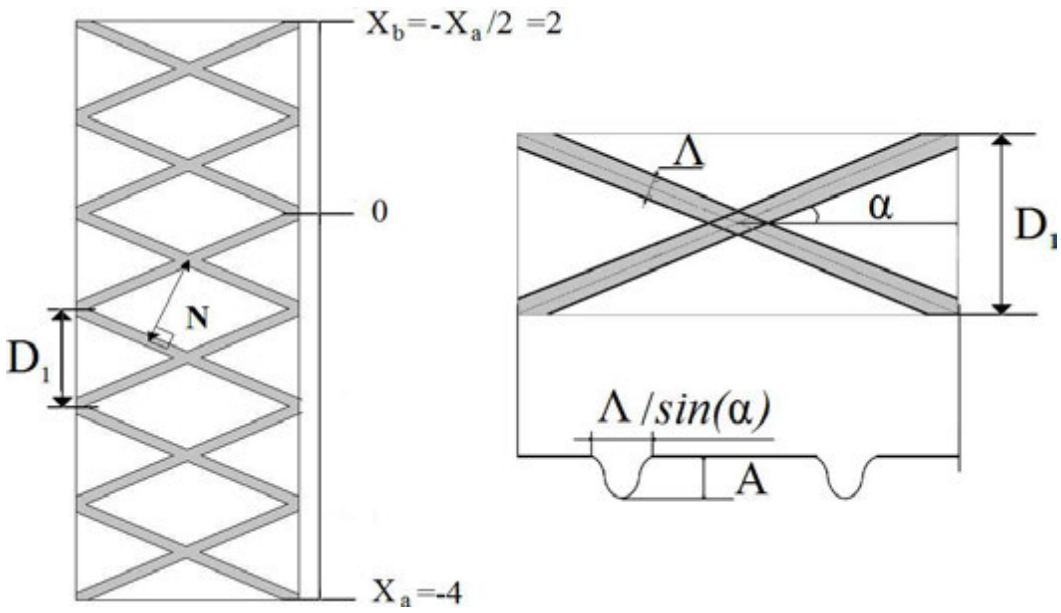

Figure 3.10: *The dimensionless microgeometric parameters and the dimensionless starvation degree parameter*

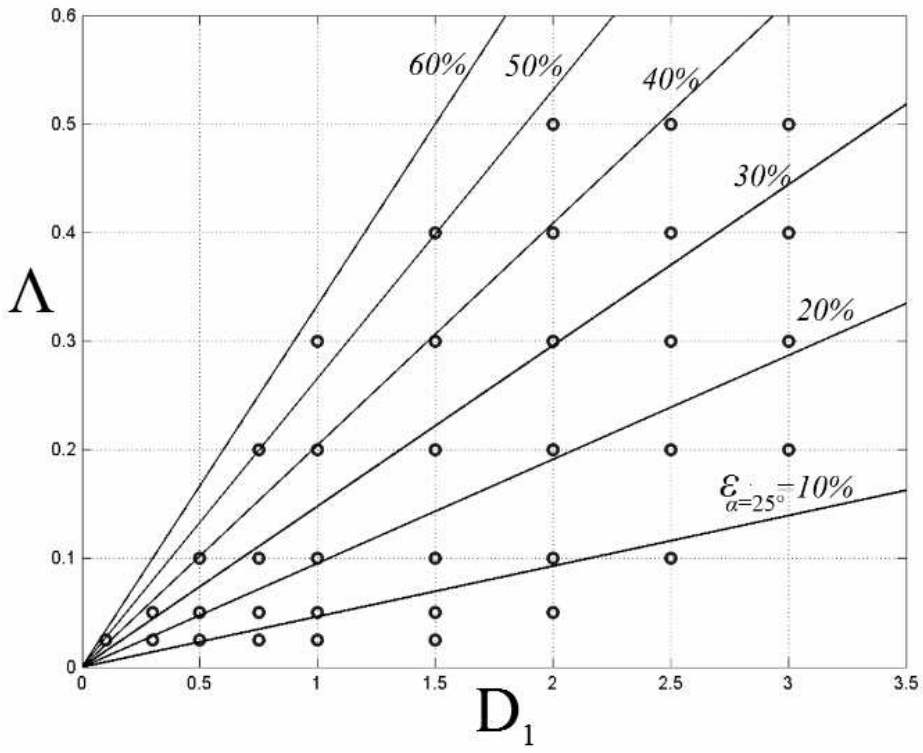

Figure 3.11: *Distribution of* Λ *and* D_1

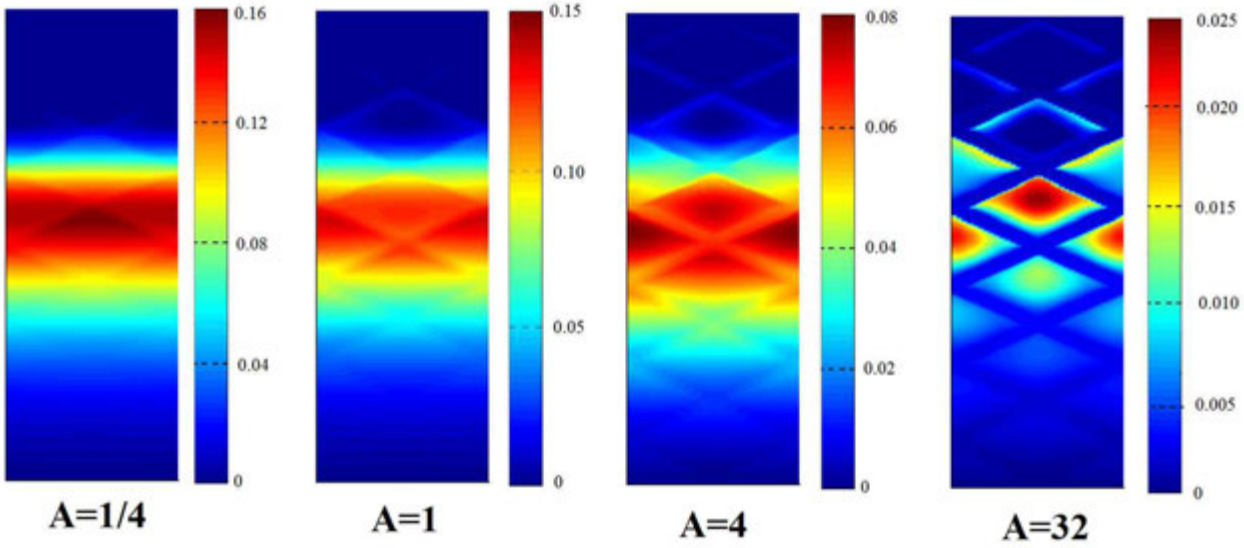

Figure 3.12: *Pressure distribution for different depth values A*

LCC is significantly affected by the change of the depth. The shallower the groove, the closer the relative LCC to the asymptotic value 1. All the shallow grooves merge with this asymptote. Otherwise, the slope is different for the five cases shown, which means that the other parameters are also important to quantify the relative LCC.

3.3.4.3 Groove density

D_1, α and Λ are written into a single parameter ϵ defined by Equation 3.9. This parameter corresponds exactly to the groove surface ratio.

$$\epsilon = \frac{\Lambda}{D_1 \cos(\alpha)}\left(2 - \frac{\Lambda}{D_1 \cos(\alpha)}\right) \tag{3.9}$$

Figure 3.14 shows the relative LCC for different angles (from 10° to 40°). For a given angle, five values of the pair (Λ, D_1) are used: (0.1,0.5), (0.2,1), (0.3,1.5), (0.4,2) and (0.5,2.5). This leads to a constant ϵ for each angle. In fact, the ratio Λ/D_1 is constant for these pairs (*cf.* equation 3.9).
Results in Figure 3.14 show that for the same groove density, with different (Λ, D_1) couples, the relative LCC is nearly the same. In other words, the LCC depends on the groove density, but not Λ and D_1 for this range of values.
One can assume that ϵ is a major parameter, roughly independent of the value of its constituents.

3.3.4.4 Master curve

A master curve is a curve that permits an instantaneous approximation of the LCC starting from a given set of the cross-hatching parameters. A single parameter regrouping all the parameters is then elaborated. Bouassida *et al.* [BOU 14] detail the components of this

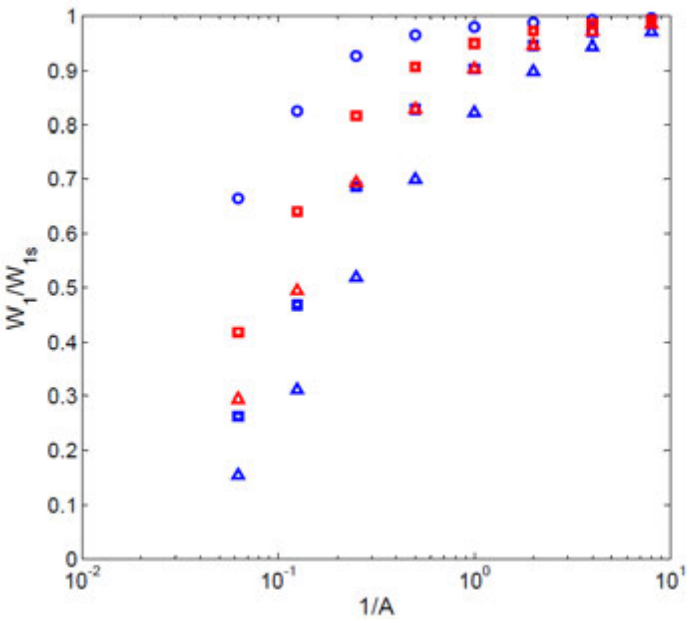

Figure 3.13: *Relative LCC as a function of* $1/A$ *for* $D_1 = 1$ *(blue) and* $D_1 = 2$ *(red),* $\alpha = 25°$ *and* $\Lambda = 0.025,\ 0.1,\ 0.2$ *(respectively circles, squares and triangles)*

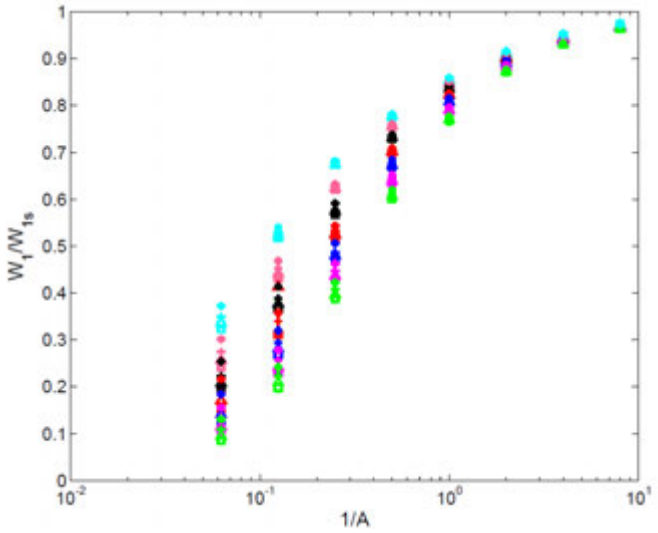

Figure 3.14: *Relative LCC as a function of* $1/A$ *for different angles* $\alpha = 10°,\ 15°,\ 20°,\ 25°,\ 30°,\ 35°,\ 40°$ *(colors) and pairs* $(\Lambda, D_1) = (0.1, 0.5),\ (0.2, 1),\ (0.3, 1.5),\ (0.4, 2)$ *and* $(0.5, 2.5)$ *(markers)*

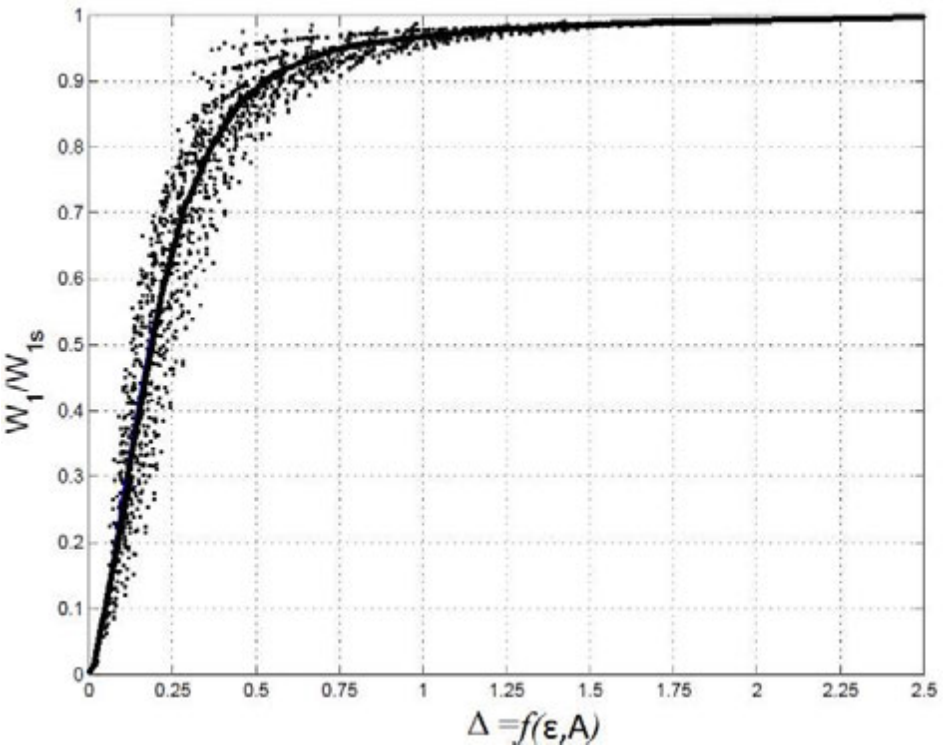

Figure 3.15: *Relative LCC as a function of* Δ*: the calculations results(markers) and the curve fit (solid line)*

single parameter called Δ (also in appendix C). Equation 3.10 gives its expression. This parameter is mainly composed of two terms: a term containing the groove density and a term containing the depth. This reinforces the idea that these two parameters are the two major parameters.

$$\Delta = -log(\epsilon)\frac{1 + A + 3A^2/8}{(1 + A)^{2.5}} \tag{3.10}$$

Figure 3.15 shows the relative LCC as a function of Δ for all 2016 calculations. Each marker corresponds to a calculational result. The scattered plot obtained shows that above a value of Δ about 0.7, all the grooves generate a LCC close to the smooth LCC. In other words, small values of ϵ and A give a relative LCC close to 1. The deep and dense grooves are on the contrary gradually approaching the zero value. A curve fit based on exponentials is carried out. The form proposed in Equation 3.11 correspond to the solid line drawn in Figure 3.15

$$W_1/W_{1s} = 1 - e^{-9.2\Delta} - e^{-5.4\Delta} - e^{-1.9\Delta} + e^{-13.5\Delta} + e^{-2.1\Delta} \tag{3.11}$$

3.3.5 Starvation influence

The previous calculations were carried out with X_a equals to 4. To extend relation 3.11 for other starved conditions, additional calculations are performed with X_a ranging from 1 to 32. The value of 1 corresponds to relatively severe starvation conditions and the value 32 to close to fully flooded conditions. Figure 3.16 shows results for $X_a = 1$ ($\triangle$), $X_a = 4$ ($\circ$) and

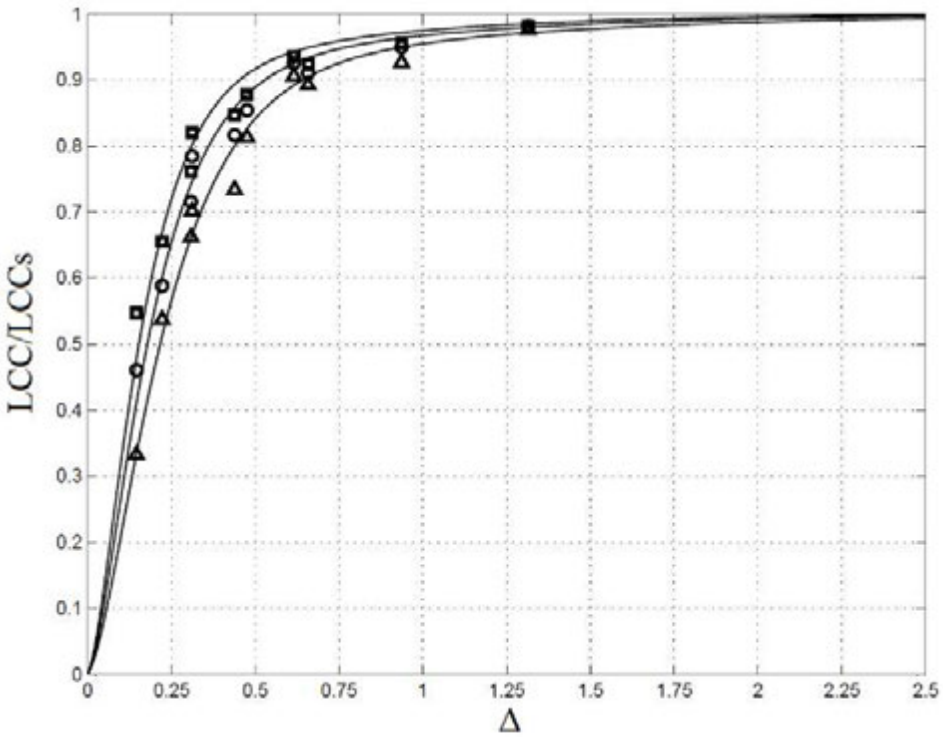

Figure 3.16: *Fitted curves for $X_a = 1$ ($\triangle$), $X_a = 4$ ($\circ$) and $X_a = 32$ ($\boxdot$)*

$X_a = 32$ ($\boxdot$). The curve fits proposed in Equation 3.12 are based on the Equation 3.11 with the introduction of a parameter f corresponding to the starvation degree X_a according to the table 3.3. f is called starvation curve fit factor.

$$W_1/W_{1s} = 1 - e^{-9.2\,f\,\Delta} - e^{-5.4\,f\,\Delta} - e^{-1.9\,f\,\Delta} + e^{-13.5\,f\,\Delta} + e^{-2.1\,f\,\Delta} \tag{3.12}$$

$-X_a$	1	2	4	8	16	32
f	0.85	0.85	1.03	1.15	1.20	1.20

Table 3.3: *Starvation curve fit factor f*

3.3.6 Interpretation

In this subsection, the starting point is Figure 3.2 which shows the starvation influence in smooth case for three cylinder positions (TDC, MS, BDC). One can go further and analyse the influence of cross-hatched grooves in these cases. The objective here is to compare different groove influences and to evaluate the LCC decrease. The microgeometry is the same for the three positions, only the viscosity and the velocity change. Since the LCC is proportional to the product of the viscosity and the velocity, the LCC is shifted vertically.

Figure 3.17 shows the load carrying capacity as a function of the central film thickness for

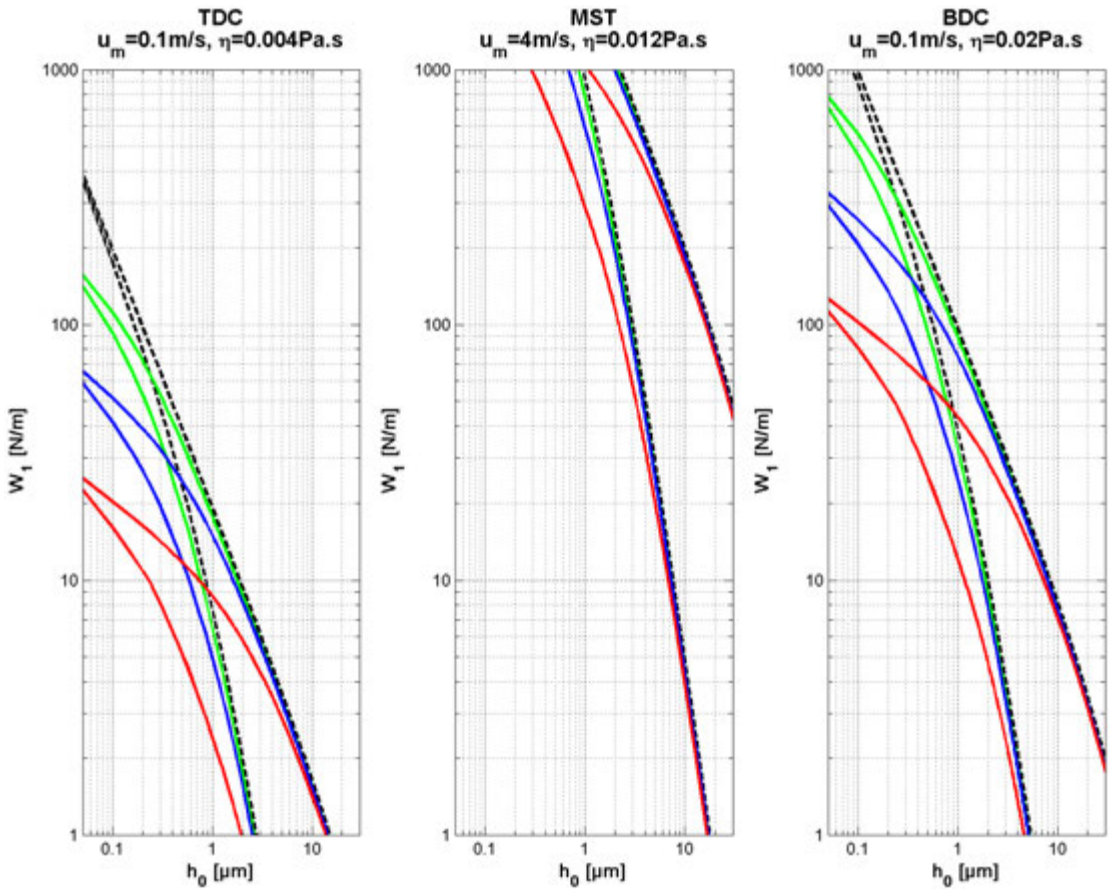

Figure 3.17: *Load carrying capacity per unit length as a function of the film thickness (solid lines: grooved, dashed: smooth), $a = 0.25\mu m, \epsilon = 50\%$ (green solid), $a = 1\mu m, \epsilon = 50\%$ (blue solid) and $a = 4\mu m, \epsilon = 50\%$ (red solid)*

the TDC, MS and BDC as in Figure 3.2. It compares the smooth case (dashed lines) with three grooved cases with the same density $\epsilon = 50\%$ and different depths $a = 0.25\,\mu m$ (green), $a = 1\,\mu m$ (blue) and $a = 4\,\mu m$ (red), for each depth, results for two starvation degrees are shown (bottom to top respectively $x_a = 0.2\,mm$ and $x_a = 1.6\,mm$).
To analyse this figure, two observations have to be kept in mind:
- The load is assumed to be around $250\,N/m$, since the pretension of the rings is of the same order of magnitude.
- Around and below $0.6\mu m$, the central film thickness reaches the mixed regime, assuming that the surface roughness σ is about $0.2\,\mu m$ and applying the well known law that says that above 3σ the lubrication regime is fully hydrodynamic.
Both the TDC and BDC are in the mixed regime. In fact, the LCC generated by the oil is insufficient to bear the load in this example. This LCC is getting worse when the grooves are very deep ($a = 4\,\mu m$). The proportion of the hydrodynamic LCC of the total load in the mixed regime is determined by the depth. The deeper the groove, the lower this proportion. Meanwhile for MS, the same load can easily be carried by the hydrodynamic LCC and the film thickness is between 1 and $10\mu m$ depending on the starvation degree. The influence of the grooves for these conditions is minimal even for deep grooves.

Figure 3.18 compares the LCC for different groove densities. As for depth, the density greatly influences the LCC in TDC and BDC. Thus, it determines also the hydrodynamic proportion in mixed regime.

3.4 Oil control ring: flat shape

3.4.1 Objectives

For a smooth liner, the OCR's LCC is very low compared with the one generated by the top ring (Figure 3.2). Nevertheless, both carry almost the same load (order of magnitude $250N/m$). That suggests that the mechanism that generates hydrodynamic pressure differs in both rings. While the top ring is characterised by its curvature and the pressure is build up by the wedge term (Equation 1.1), the OCR is considered flat and the pressure is generated by the grooves. The objective of this section is to analyse the LCC generated by the grooves through 2D hydrodynamic calculations.

3.4.2 The parameters

The OCR model exposed in chapter 2 and the analytical surface model are considered. The model is completely described by five parameters. The number of microgeometric parameters is reduced from 4, for the top ring, to 3 parameters for the OCR. Considering the fact that the groove width λ is the dimensionless parameter for the length scale, the dimensionless groove width Λ is equal to 1. The 3 groove parameters are then: the relative depth A, the distance D_1 and the groove angle α. Both boundaries of the calculation window X_a and X_b are also parameters to be considered.

As mentioned in the paragraph 3.3.2.1, the period in the pressure profile is the half of a cross-hatching pattern. It is more convenient to focus on what is happening in only the half of a cross-hatching pattern ($D_1/2$) and then generalise to more than that. In fact, central patterns LCC's are not affected by the boundary conditions in sliding direction and then

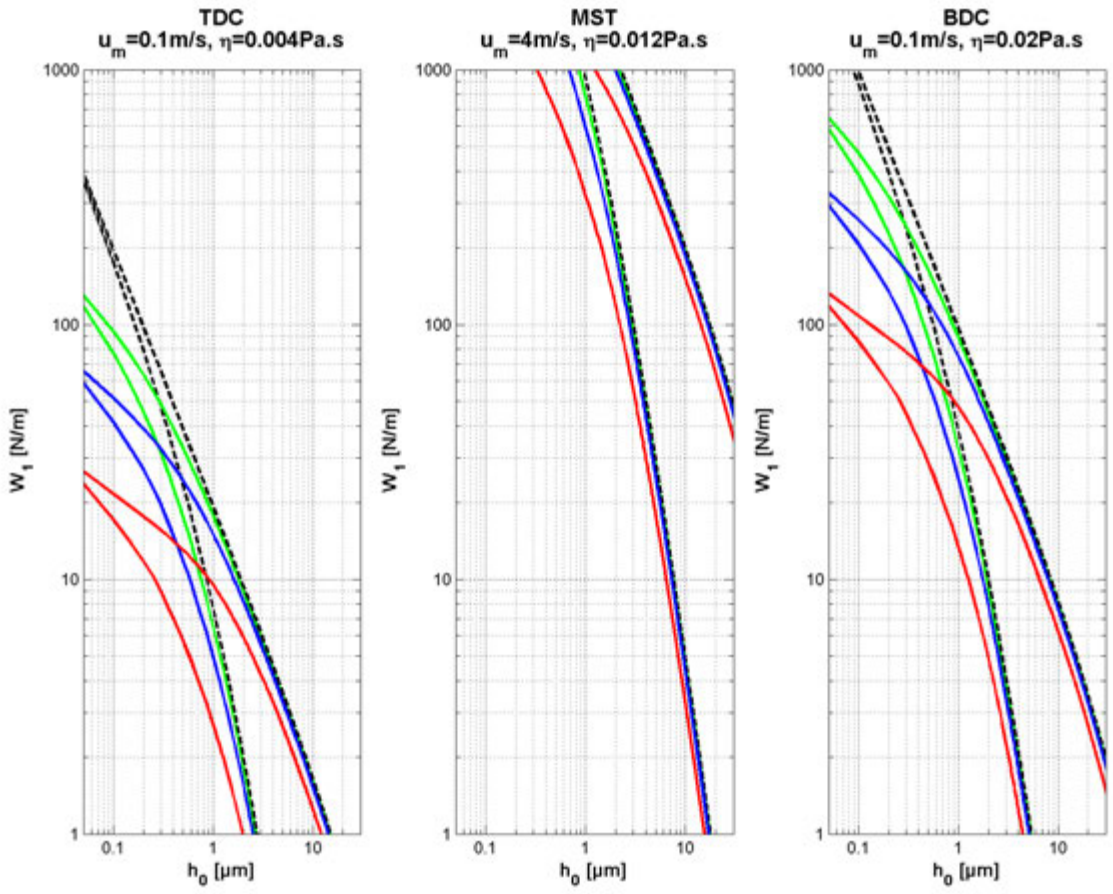

Figure 3.18: *Load carrying capacity per unit length as a function of the film thickness (solid lines: grooved, dashed lines: smooth), $a = 1\mu m, \epsilon = 30\%$ (green solid), $a = 1\mu m, \epsilon = 50\%$ (blue solid) and $a = 1\mu m, \epsilon = 70\%$ (red solid)*

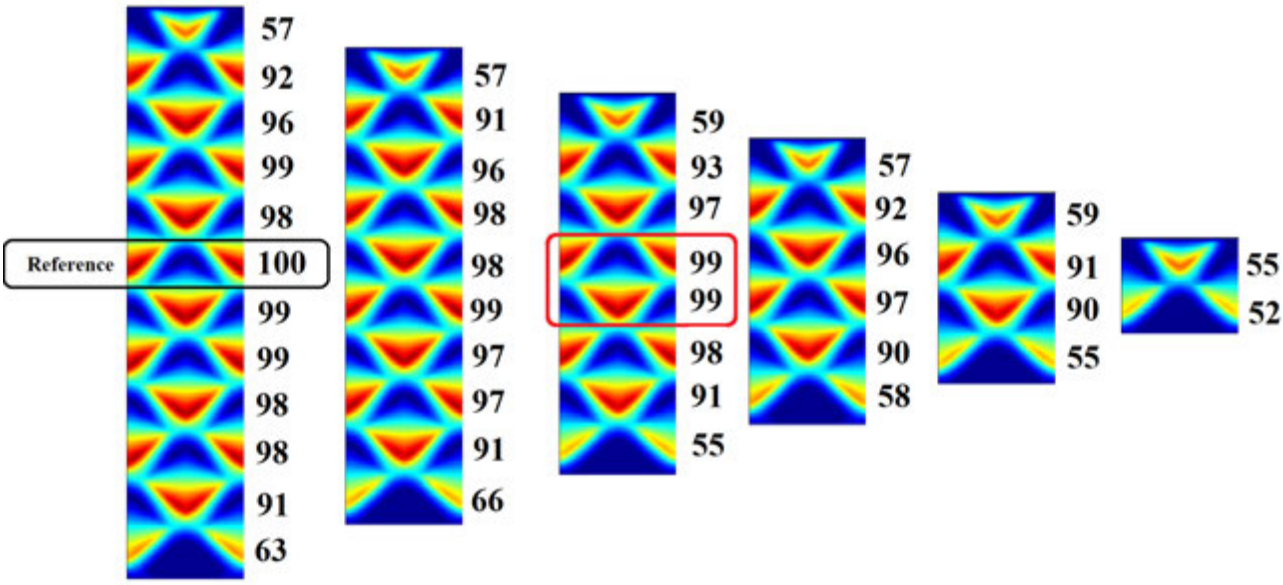

Figure 3.19: *Typical pressure profiles (left to right 6 to 1 pattern length) and the value of the LCC proportion for each half pattern in percentage compared with the reference (black box)*

considered the same. Figure 3.19 shows pressure profiles for 1 to 6 patterns.
The reference pattern is a half of a central pattern (black box). Figure 3.19 shows that except for the boundary halves, the LCC is nearly the same (more than 90%).
This permits one to consider the case of a 4 pattern length domain as a reference case for the calculations. In other words $X_b - X_a = 4D_1$. This length ensures that the central pattern LCC is not affected by the boundary conditions in sliding direction.
The calculated result is the LCC generated in the central pattern (red rounded in Figure 3.19). Considering $X_b = -X_a = 2D_1$, the input parameters become only the three groove parameters (A,D_1 and α).
To analyse the results, the 1D analytical model results by Biboulet *et al.* [BIB 14b] are used. Biboulet found that the maximum pressure is twice the mean pressure. Figure 3.20 explains briefly the 1D model with a simplified geometry. The distance between two parallel grooves N is used in this model. The analytical solution found by Biboulet is:

$$P_M = \frac{A\big(A(N-1)+N-1/2\big)^2}{(1+A)\big((1+A)(N-1)+1\big)\big(2(N-1)(1+A)^2+A+2\big)} \tag{3.13}$$

For 2D model, the parameter N is exactly the distance between two parallel grooves (*cf.* Figure 3.10). It can replace D_1 for the analysis with $N = D_1\cos(\alpha)$. The input parameters become A,N and α.

Figure 3.21 shows examples of the pressure profile for different groove depths. The pressure is integrated over the central pattern to obtain the load carrying capacity. For convenience, the output W_1 of the 2D calculations is divided by the distance D_1, corresponding to the mean pressure. Thus, one can obtain the double of this value. This value is incorrectly called the maximum pressure P_M.

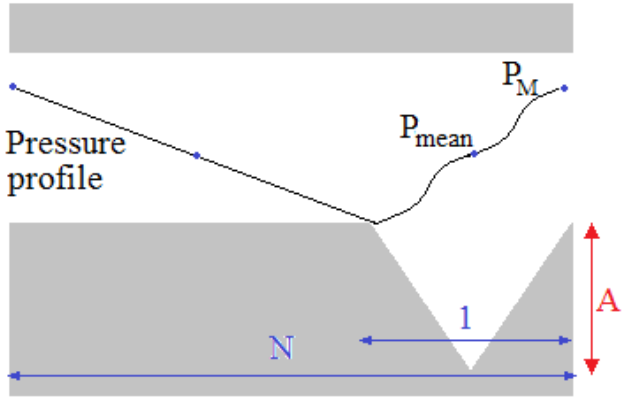

Figure 3.20: *1D model and the pressure profile [BIB 14b]*

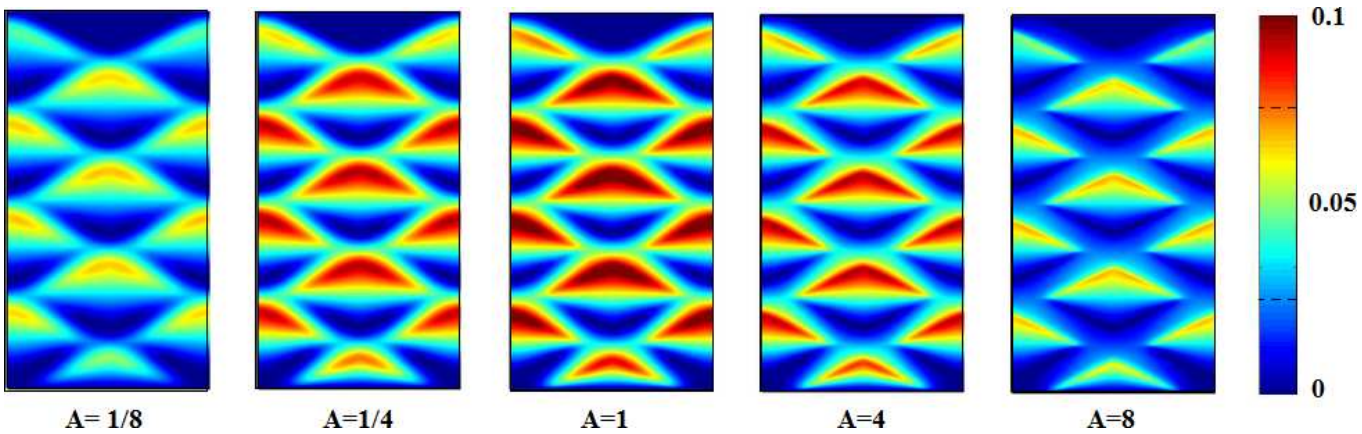

Figure 3.21: *Pressure profile for different groove depths*

Depth A	$\mathbf{2^{-5}}$	**1**	**2**	**4**	**8**	**16**	**32**
$Mesh_{ref}$	1/96	1/96	1/96	1/192	1/384	1/384	1/384
W_{1ref}	0.0162	0.142	0.121	0.0833	0.0509	0.0276	0.0141
$Mesh$	1/48	1/48	1/48	1/96	1/192	1/192	1/192
W_1	0.0163	0.141	0.119	0.0811	0.0496	0.0277	0.0157
$(W_1 - W_{1ref})/W_{1ref}$	0.2%	0.8%	1.5%	2.6%	2.6%	0.4%	11%
$Mesh$	1/24	1/24	1/24	1/48	1/96	1/96	1/96
W_1	0.0165	0.1431	0.122	0.0829	0.0489	0.0299	0.0209
$(W_1 - W_{1ref})/W_{1ref}$	1.7%	0.4%	1.1%	0.5%	3.8%	8%	47%
$Mesh$	1/12	1/12	1/12	1/24	1/48	1/48	-
W_1	0.0172	0.159	0.150	0.104	0.0551	0.0420	-
$(W_1 - W_{1ref})/W_{1ref}$	6%	12%	24%	25%	8%	52	-
$Mesh$	1/6	1/6	1/6	1/12	1/24	-	-
W_1	0.0193	0.212	0.237	0.187	0.0890	-	-
$(W_1 - W_{1ref})/W_{1ref}$	18%	48%	95%	125%	74%	-	-

Table 3.4: *Accuracy of W_1 for different mesh sizes*

3.4.3 Mesh-size

As in paragraph 3.3.3, the accuracy of the LCC is studied as a function of the mesh size. Table 3.4 shows the relative error compared with the reference case of the LCC for a very fine mesh (first row in the table). The calculations were performed for $\alpha = 25°$ and $N = 2.5$.The mesh size depends on the slope Λ/A with $\Lambda = 1$. That means that the deeper the groove, the finer the mesh has to be.

The third row meshes are sufficient meshes to guarantee a good approximation except for $A = 32$ and a little $A = 16$. Unfortunately, taking a 1/192 mesh for $A = 32$ (instead of 1/96 for the third row) will impact the computing time and the memory used. In fact, for the case where $\alpha = 15°$ and $N = 10$ the domain size is $4N/\cos(\alpha) \times N/\sin(\alpha) \simeq 41 \times 38$ and thus the number of points is about 7872×7296 which is a huge number even for multigrid method!

The calculations are performed with respect to the mesh sizes of the third row. That means that for a depth less than 4, the mesh size is 1/24, for $A = 4$ it is 1/48 and for more than 4 it is 1/96.

3.4.4 Influence of the groove parameters

3.4.4.1 Groove density

Knowing that $D_1 = N/\cos(\alpha)$ and that $\Lambda = 1$, the groove density or the groove surface ratio ϵ becomes:

$$\epsilon = \frac{1}{N}(2 - \frac{1}{N}) \tag{3.14}$$

Equation 3.14 shows that for $N = 1$ the grooves cover all the surface and there is no plateaux. For $N \gg 1$ the grooves are very sparse. The calculations are performed for $N = 2.5$, 3, 3.5, 4, 5, 6, 8 and 10 corresponding respectively to $\epsilon = 64\%$, 55%, 49%, 43%, 36% 30%, 23%, and 19%.

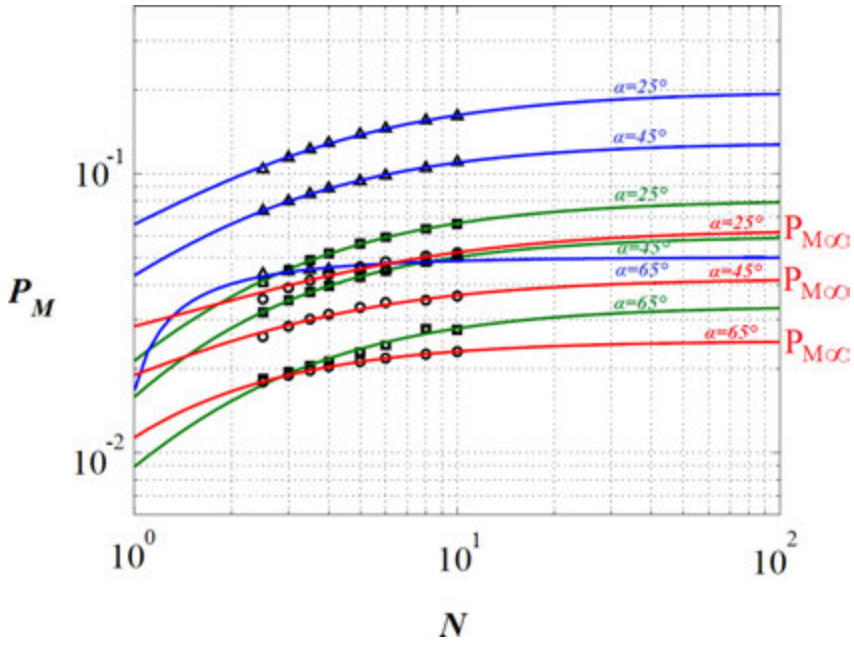

Figure 3.22: *Maximum pressure as a function of the groove density N for $\alpha = 25°$, $45°$ and $65°$ (top to bottom) and for $A = 1/8$ ($\circ$), $A = 1$ ($\triangle$), and $A = 8$ ($\boxdot$)*

In Figure 3.22 P_M is curvefitted using Equation 3.13. Only a few angles and depths are shown ($\alpha = 25°$, $45°$, $65°$ and $A = 1/8$, 1, 8). The results show that there is a horizontal asymptote for $N \gg 1$ for each case. The groove LCC is maximal and the maximum pressure is noted $P_{M\infty}$. The curve fit permits to extract each value of $P_{M\infty}$.

3.4.4.2 Groove angle

The calculations were performed for various angles (from 5° to 65° in 10° steps). After curvefitting P_M as a function of N, one obtain asymptotic values $P_{M\infty}$. Figure 3.23 shows with markers these $P_{M\infty}$ as a function of the angle α and the depth A. When analysing these results, one can observe that the maximum pressure decreases when the angle becomes large. In fact, for 90° the grooves are parallel to the sliding direction suggesting that the LCC is nil and $P_M = 0$. A cosine sign correspond to this behaviour. Equation 3.15 curve fits the numerical results. $P_{M\infty 0}$ is the value at $\alpha = 0°$.

$$P_{M\infty} = P_{M\infty 0}.\cos^{7/5}(\alpha) \tag{3.15}$$

3.4.4.3 Groove depth

The markers in Figure 3.24 present the values of $P_{M\infty 0}$ found by the angle curve-fitting. The depth is curvefitted using Equation 3.13 when $N \to \infty$ (sparse grooves). The maximum pressure $P_{M\infty 0}$ reads:

$$P_{M\infty 0} = \frac{1}{2}\frac{1.73\,A}{(1 + 1.18\,A)^2} \tag{3.16}$$

The LCC has a maximum at $A = 1/1.18 = 0.84$. In other words, at this position the groove that carries the highest load is the groove corresponding to $A = 0.84$, which means

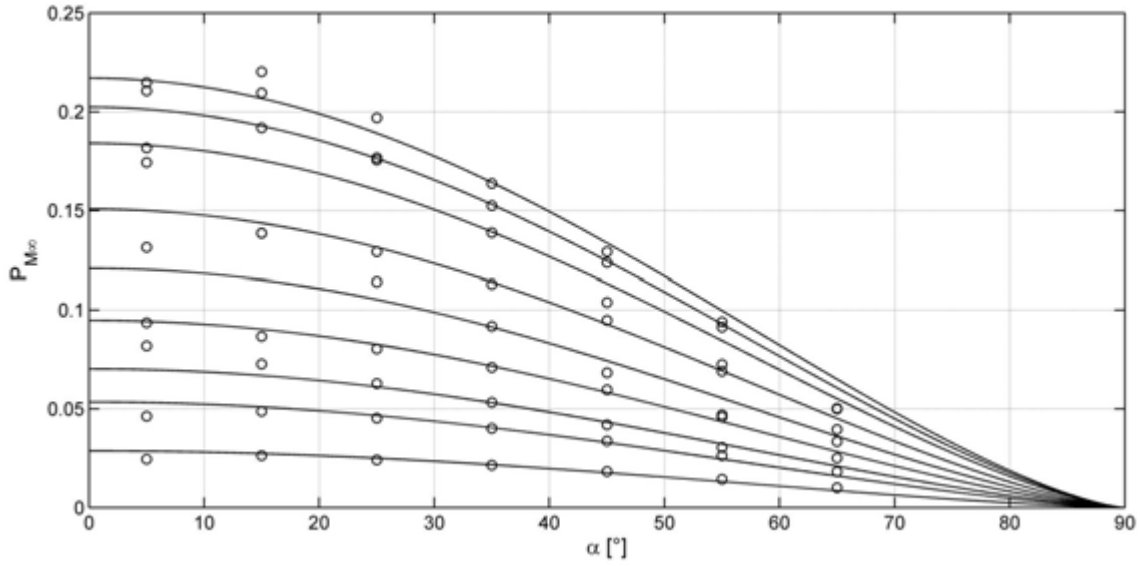

Figure 3.23: *Maximum pressure for very sparse grooves $P_{M\infty}$ as a function of the angle α: from top to bottom $A = 1, 1/2, 2, 1/4, 4, 1/8, 8, 1/16, 1/32$*

$a/h_0 = 0.84$. As a consequence, for a given film thickness h_0, the groove that carries the highest load is the groove with a depth $a = 0.84\, h_0$.

3.4.5 Boundary effects

Thanks to the curve-fits, the value of P_M can be predicted for a set of groove parameters. The LCC in a single central pattern for this microgeometry can be deduced and is simply $P_M/2 \times D_1$. As mentioned in section 3.4.2, the total LCC is the sum of the LCC of all patterns. While the central patterns are well approximated by $P_M/2 \times D_1$ (better than 90%), the patterns located near both boundaries, depending in which position they are, generate less LCC. To approximate the total LCC, various calculations are performed with the boundary patterns changing position. Table 3.5 shows, for three different cases, the ratio between a central LCC multiplied by the number of patterns and the average LCC calculated including the boundaries. For example for $X_b - X_a = 4D_1$, the LCC reads:

$$W_1 = 0.88 \times 4 \times \frac{P_M D_1}{2} \tag{3.17}$$

For less than one pattern, the load carrying capacity drops rapidly. For example for $X_b - X_a = 0.5D_1$, the resulting LCC is about 30% of the curve-fitted value.

3.4.6 Interpretation

In this subsection the example of the microgeometry seen in subsection 3.3.6 is analysed. The groove parameters are $\alpha = 25°$, and $N = 3.5$. The choice of $d_1 = 100\mu m$ leads to $\lambda = 25.9\mu m$ which gives an ϵ of 50%. The depth of the grooves is taken as $0.25\mu m$, $1\mu m$

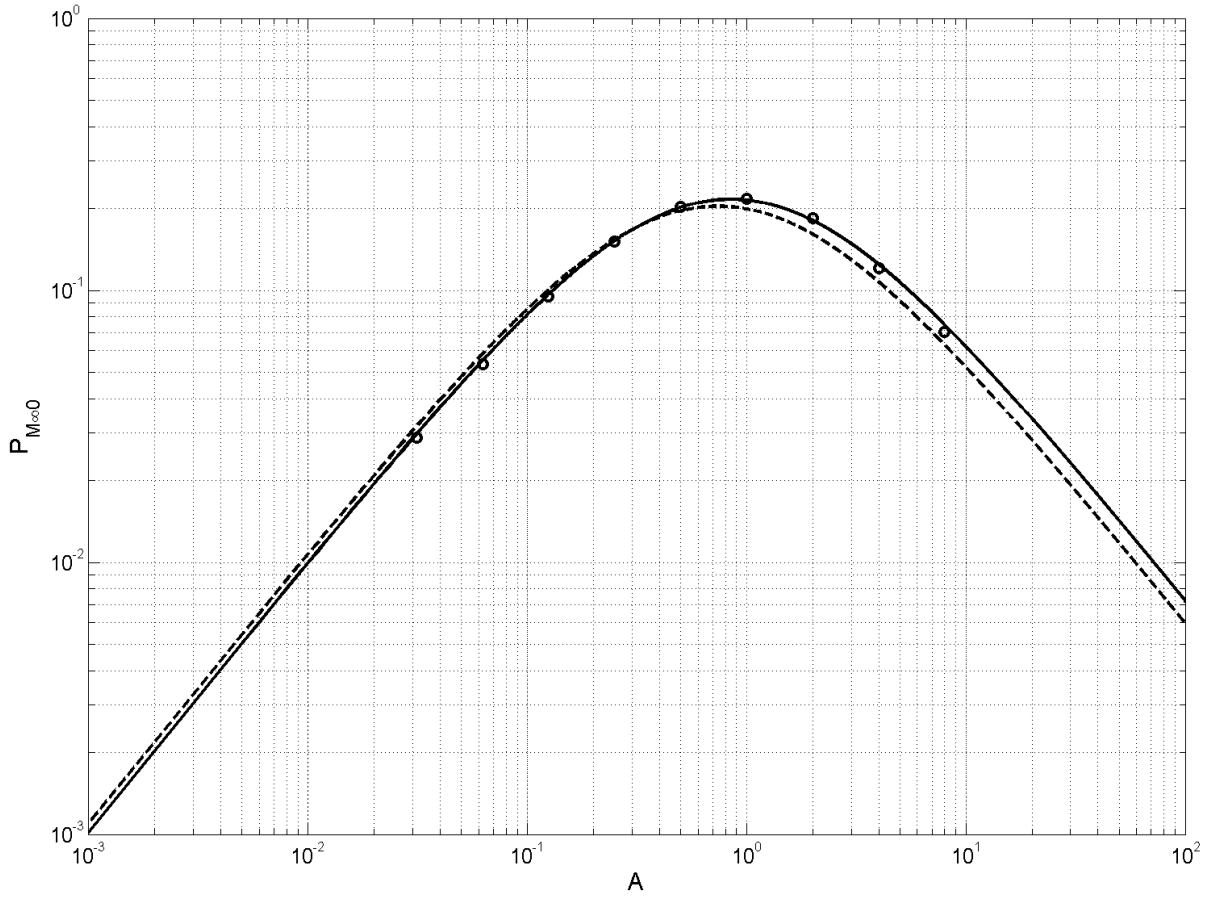

Figure 3.24: *Maximum pressure for sparse grooves and zero angle $P_{M\infty 0}$ as a function of A (solid line for curve fit and dashed line for Biboulet formula [BIB 14b])*

Nb patterns	4	3	2	1.5	1	0.5
$A = 1$, $\alpha = 25°$ **and** $N = 2.5$	87%	83%	75%	67%	55%	29%
$A = 1$, $\alpha = 25°$ **and** $N = 5$	88%	85%	76%	69%	56%	32%
$A = 1$, $\alpha = 45°$ **and** $N = 2.5$	89%	85%	77%	70%	59%	37%

Table 3.5: *Percentage of the total LCC as a function of the number of patterns*

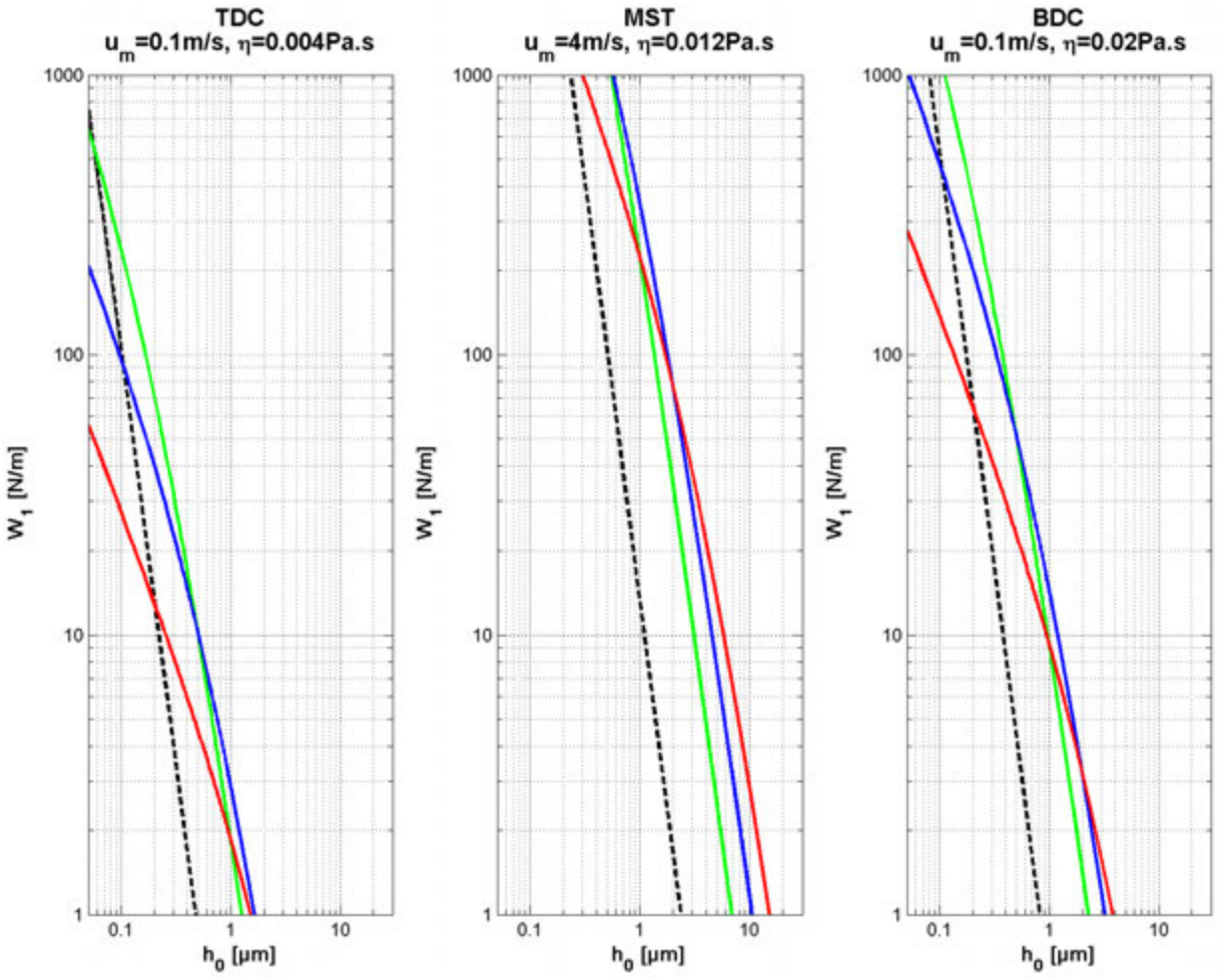

Figure 3.25: *Load carrying capacity per unit length as a function of the film thickness for four microgeometries:* $a = 0.25\mu m$, $N = 3.5$ *and* $\alpha = 25°$ *(green solid),* $a = 1\mu m$, $N = 3.5$ *and* $\alpha = 25°$ *(blue solid),* $a = 4\mu m$, $N = 3.5$ *and* $\alpha = 25°$ *(red solid) and the smooth case (dashed line).*

and $4\mu m$. Assuming that $x_a = 200\mu m$, the domain length in the sliding direction is $4 \times d_1$. Figure 3.25 shows the LCC generated by the same microgeometry for three different lubrication conditions: close to TDC ($\eta = 0.004Pa.s$ $u_m = 0.1m/s$), MST ($\eta = 0.012Pa.s u_m = 4m/s$) and close to BDC ($\eta = 0.02Pa.s u_m = 0.1m/s$).

The first observation is that the level of the LCC of a smooth surface (with a curvature) is very low compared with the one generated by the grooves. The flat surface model is confirmed.

The second observation concerns the importance of the groove depth in carrying the load. In fact, as seen from Equation 3.16, to each film thickness corresponds an optimum groove depth that carries the highest load.

Figure 3.26 shows the LCC for three other sets of groove parameters, keeping $\alpha = 25°$, and $a = 1\mu m$ and changing N to 2.2, 3.5 and 6.1 corresponding to $\epsilon = 70\%$, 50% and 30%. Even if there is a difference between the different cases, the LCC for sparse grooves and dense ones are close to each other. The groove density is important to determine the load level but for

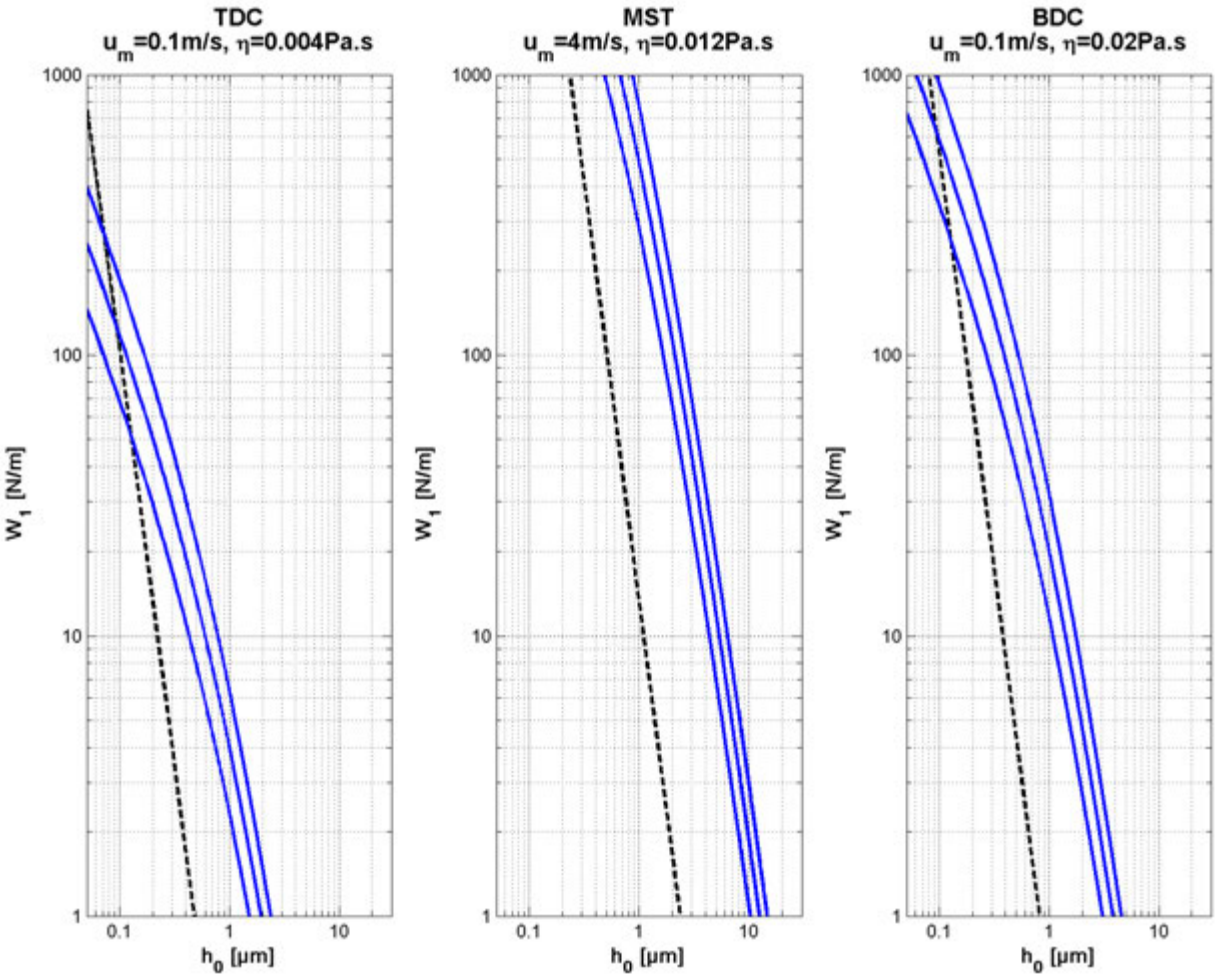

Figure 3.26: *Load carrying capacity per unit length as a function of the film thickness for four microgeometries:* $a = 1\mu m$, $N = 2.2$ *and* $\alpha = 25°$, $a = 1\mu m$, $N = 3.5$ *and* $\alpha = 25°$, $a = 1\mu m$, $N = 6.1$ *and* $\alpha = 25°$ *(solid lines bottom to top) and the smooth case (dashed line).*

a given film thickness the depth will be more determinant.

3.5 Conclusion

Three PRCL models were investigated in this chapter via the load carrying capacity - film thickness relation. First, the smooth case was explored in the fully flooded regime (Moes [MOE 00]) and in the starved regime (Biboulet [BIB 13]). The importance of the starvation degree was highlighted for both compression and oil control ring. Second, the LCC generated by the top ring was investigated with the presence of cross-hatched grooves. A master curve was deduced from a single parameter regrouping all the microgeometric parameters. This prediction allows a fast approximation of the load carrying capacity for a given range of film thicknesses. Finally, the flat ring case was studied. The LCC is generated by the grooves in that case. The influence of the cross-hatching parameters has been studied. As for the top

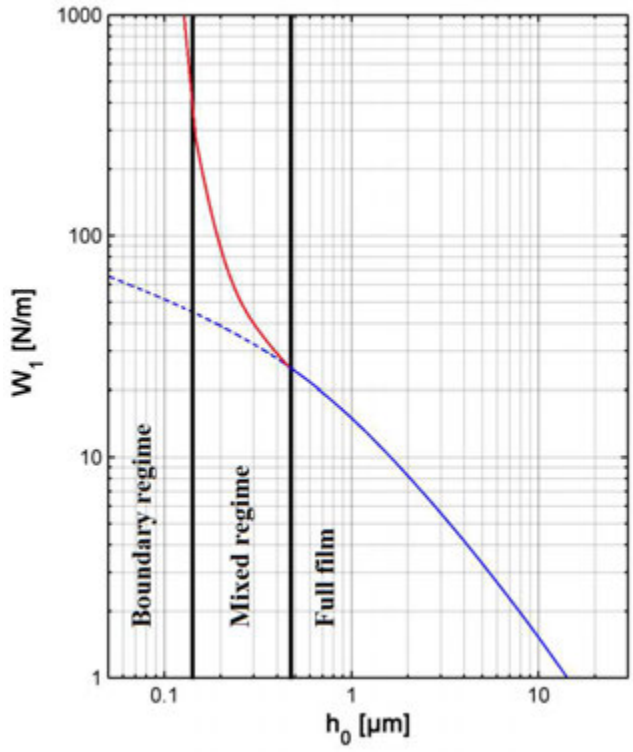

Figure 3.27: *Load carrying capacity per unit length as a function of the film thickness: Example of the force generation in the mixed regime*

ring, the LCC can be predicted.
As a perspective, the prediction of the load carrying capacity can be completed by an asperity contact model (notably Greenwood [GRE 66] [GRE 70] [GRE 82] and for more details about models Beheshti and Khonsary [BEH 12]) leading to a three regime curves (hydrodynamic, mixed and boundary regimes). Figure 3.27 illustrates such a curve. The red line represent the asperity contact and the blue one represents the hydrodynamic force.

Chapter 4

Measured surface calculations: Prediction and validation

Contents

4.1 Introduction

The ultimate objective of the liner hydrodynamic analysis is to optimise the microgeometry in order to enhance the engine performance. The predictions from Chapter 3 allow such an optimization. In fact, starting from microgeometry data, the load carrying capacity is predicted. As a consequence the tribological performance can be deduced (oil availability, friction...). The scope of the current chapter is to validate the chapter 3 prediction model. Measured surface calculations are used for this validation.
Chapter 3 dealt with analytical liner surfaces. These surfaces are idealized models of the real surface. The real surfaces are rough and wavy (macroscopic curvatures). The real grooves are not uniform (neither constant width, depth or angle). This chapter links the analytical model to the real surface model through measured surface calculations. The prediction of the load carrying capacity starts from the liner microgeometry parameters. The model used in Chapter 3 has a unique set of parameters for each surface. However, measurements show that real surfaces are not that uniform. For validation purposes, three steps are necessary for each measured surface:
- extract the parameter distribution,
- link the distribution to a unique set of parameters,
- compare the prediction with the measured surface result.

The first part of this chapter compares both geometries, the analytical one and the measured one. The second part concerns the parabolic shaped rings (notably the top ring) and the validation of the corresponding prediction. The last part is dedicated to the validation of the flat ring (oil control ring) prediction model.

4.2 Geometry: Analytical vs Measured

This section starts by describing the measured surfaces samples. This description highlights the major differences between a measured surface and an idealised one. A second part is dedicated to the identification of the grooves from the measured surface samples. The extracted information will be used to create an intermediate model, linking the measured surface to the model predictions of Chapter 3.

4.2.1 Measured surface

A cylinder liner which was run for a considerable period under fired conditions is used for the measurements. It permits to evaluate the tribological performance under real conditions. Along the engine stroke the measured surfaces are worn to a different degree. In fact, near the top dead center (TDC) and near the bottom dead center (BDC) the wear is more pronounced than in the mid stroke (MST). This is due to the speed which is close to nil in both extremities and consequently due to the lubrication regime. The mixed and the boundary lubrication regimes can lead to important material removal (plastic deformation of asperity peaks could also occur). The reference position (REF) in Figure 4.1 clearly shows the difference between worn and unworn surfaces (the same height scale is used). Two qualitative observations are deduced:
- the plateau zones are smoother for worn surfaces,
- the cross-hatched grooves are deeper, larger and denser for the unworn surfaces.

The measured surfaces are treated with the software *Mountains*® to remove macrocur-

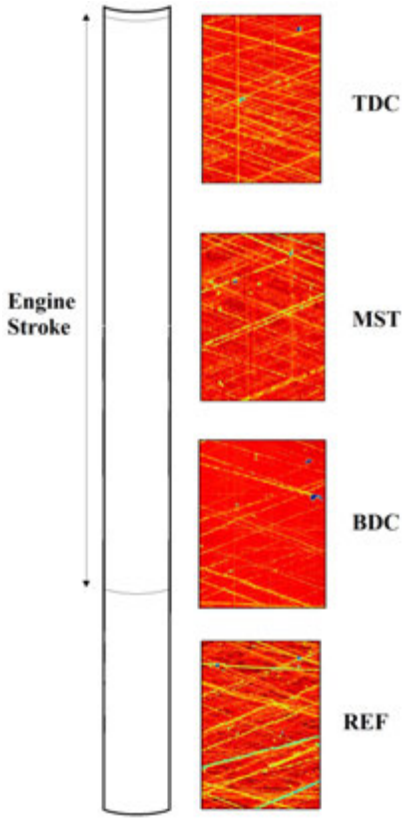

Figure 4.1: *Measured surface positions*

vature with a second degree polynomial form and to fill in the unmeasured points that are generally located on/near high slope zones (*cf.* paragraph 2.2.2.3).
In this chapter, two typical surfaces are analysed: a heavily worn and a normal worn surface (located respectively near BDC and near MST). Figure 4.2 shows both surfaces.
A thorough visual inspection of the surfaces permits to deduce important observations in addition to the previous ones:
- There are some vertical grooves that are probably the result of a piston skirt contact (continuing to the REF zone). These vertical grooves can generate "Dirichlet Boundary Conditions". In fact, if they are sufficiently deep to create a tunnel under the ring, zero pressure is generated.
- Very deep and very small local grooves are measured (blue color). These grooves can interfere with the pressure generation.
- Straight grooves are not always continuous. Some discontinuities occur.
- Small bumps occur on MST plateaux (dark colors).

4.2.2 Groove identification

4.2.2.1 The topic

The optical comparison is not sufficient to quantify the surfaces. An identification of the grooves permits to quantify two major data inherent to each surface: the groove statistics (number of the grooves and their geometry) and the plateau roughness (cf. [GAD 02] for

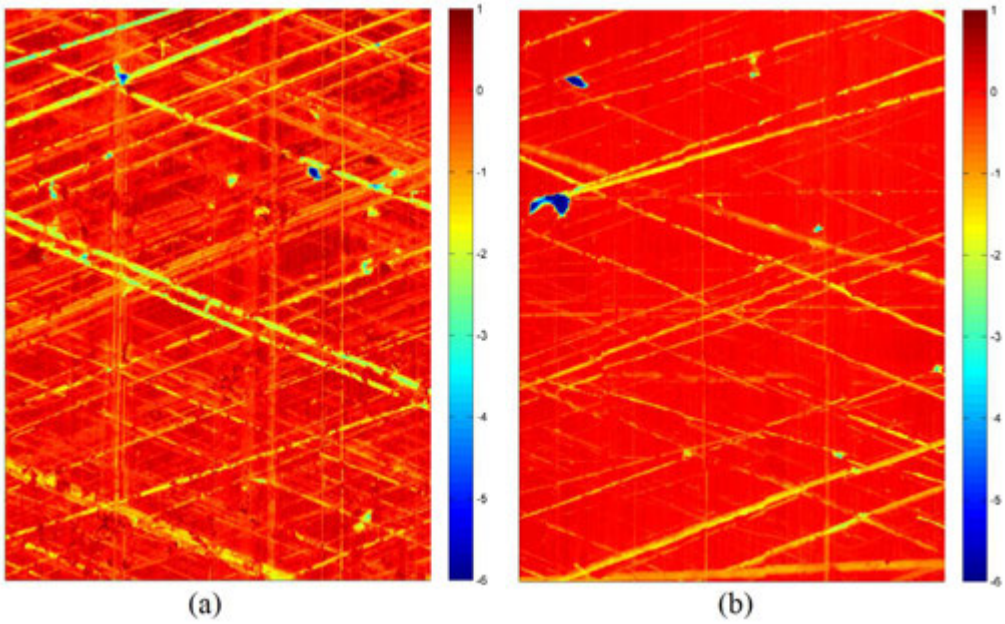

Figure 4.2: *Measured surfaces: (a) Mid-stroke (b) Bottom dead center*

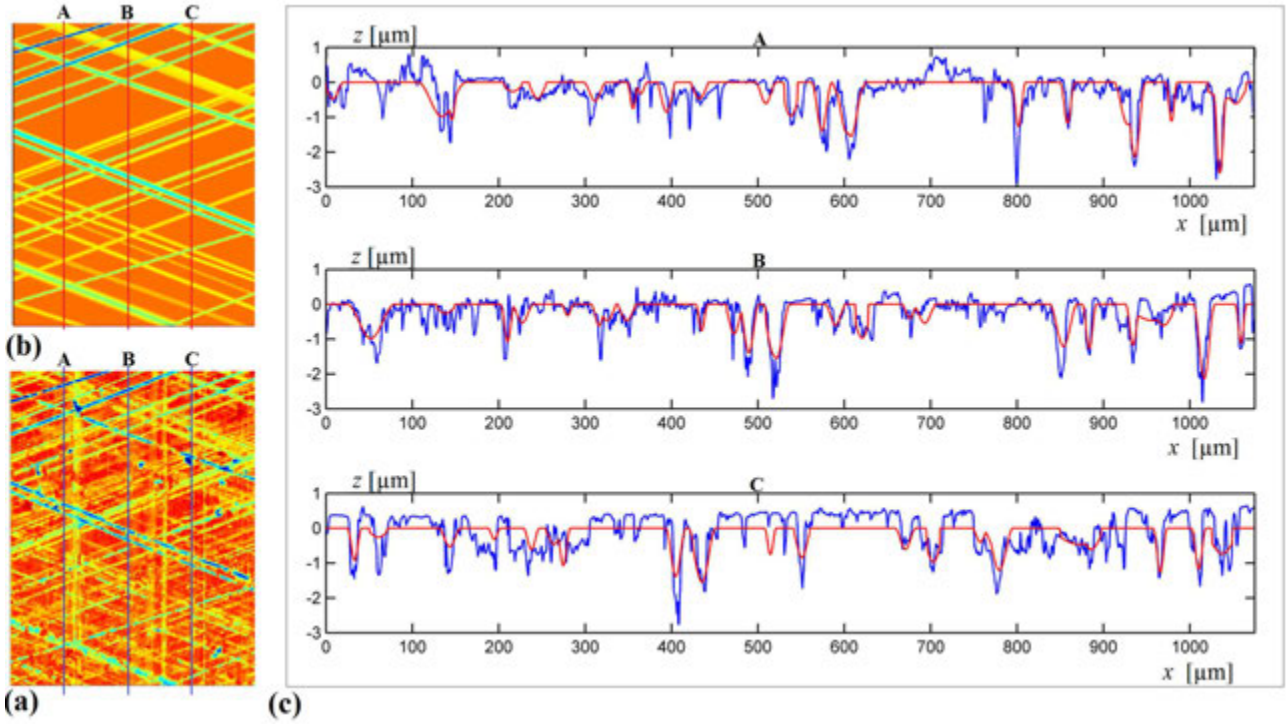

Figure 4.3: *Groove identification at MST: (a) Measured surface (b) Intermediate analytical surface (c) 1D comparison between measured (blue) and intermediate analytical (red)*

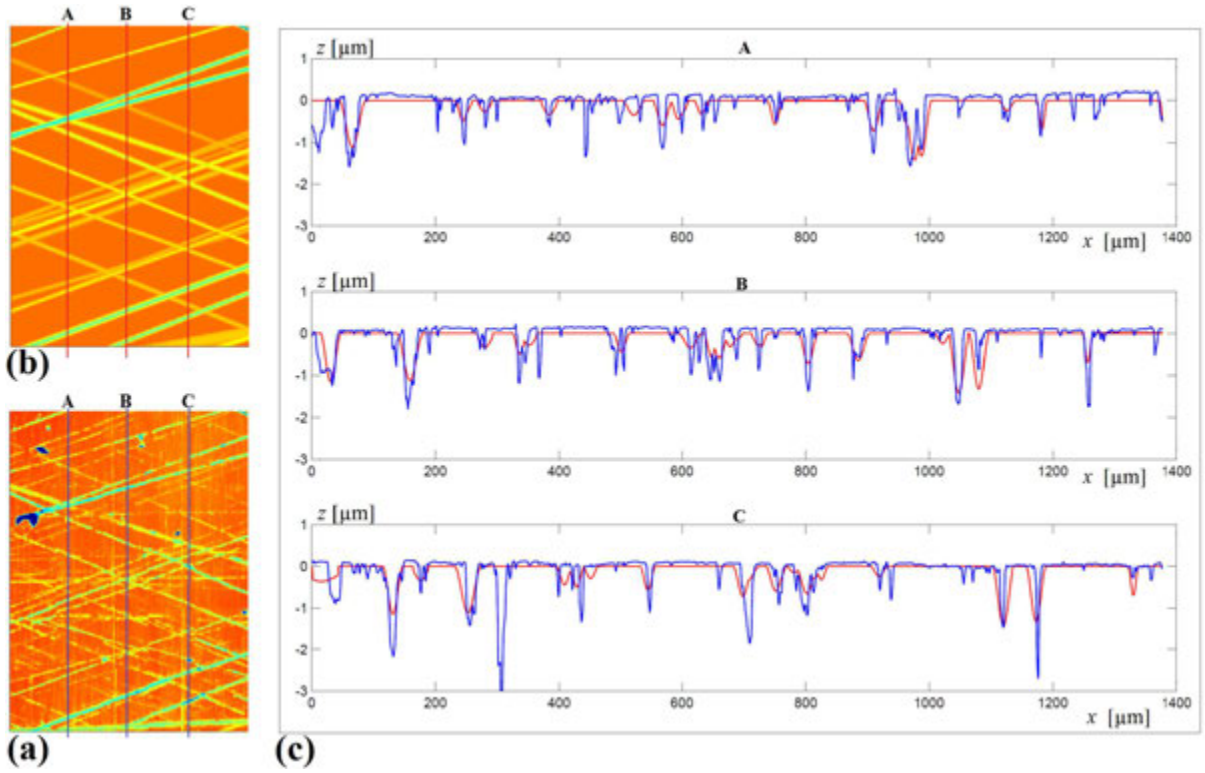

Figure 4.4: *Groove identification at BDC: (a) Measured surface (b) Intermediate analytical surface (c) 1D comparison between measured (blue) and intermediate analytical (red)*

roughness parameters). The extracted data permits a better description of the surface. It is useful for various kind of analysis (wear analysis, hydrodynamic analysis, asperity contact analysis, *etc*,). This study focuses the hydrodynamic part related to the microgeometry effect on the load carrying capacity. Thanks to the predictions of Chapter 3, one can evaluate the load carrying capacity whatever the film thickness. The HL computing time for a given value of the film thickness and a given starvation degree can reach 24 hours even with the multigrid method, while the identification permits an instantaneous evaluation of the LCC (for any value of film thickness and starvation degree).

A code that automatically identifies the grooves was developed by Biboulet [BIB14a]. It aims to extract as much microgeometry data as possible. This identification assumes the same cosine form of the groove described in Chapter 3. A straight groove with the three associated parameters (the angle α, the depth a and the width λ) is fitted to the cross-hatched grooves. The position of each groove is stored to generate the intermediate surfaces (Figure 4.3(b) and Figure 4.4(b)). These generated surfaces are the analytical equivalent of the real measured surface where the plateaux are smooth and the grooves are sinusoidal. The height scale (color) is the same, simplifying an optical comparison with Figure 4.3(a) and Figure 4.4(a).

Figure 4.3(c) and Figure 4.4(c) show the superposition of the measured surface (blue) and the intermediate surface (red). It can be concluded that all the major grooves are identified in both position and that the depth and the width approximations are correct.

Figure 4.5: *Mean line displacement*

4.2.2.2 Plateau recognition

The plateaux constitute the rough surface between the different cross-hatched grooves. The groove identification permits one to isolate these plateaux. Assuming that all the plateaux are of the same level (heights), the mean plateau position is then defined as the mean value of the non identified zone, including all the imperfections.

In this identification process it is assumed that all the cross-hatched grooves are identified. Unfortunately, the small grooves (narrow and shallow) are hard to detect. An undetected groove will tend to lower the plateau height. Figure 4.5 illustrates the displacement of the mean height caused by unidentified grooves. Other phenomena contributing to an incorrect location of the plateaux are:

- the very deep and very small local grooves,
- the macrocurvature which can not be completely eliminated.

Table 4.1 shows the mean height value $\overline{R}$ and the value of the roughness parameters R_a and R_q for both the entire measured surface and the plateau (the measured surface without identified grooves). The groove identification process moved the mean line by $0.19\,\mu m$ in MST and $0.10\,\mu m$ in BDC. It also acts on the values of R_a and R_q. These parameters are corrected, and can indicate in a better way the surface finish (eventually for a peak analysis in the mixed regime...).

		$\overline{R}\,in\,\mu m$	$R_a\,in\,\mu m$	$R_q\,in\,\mu m$
MST	only plateau	0	0.280	0.370
	all the surf.	-0.190	0.417	0.570
BDC	only plateau	0	0.132	0.371
	all the surf.	-0.105	0.258	0.482

Table 4.1: *Mean height and roughness parameters on plateaux and complete surface*

4.2.2.3 Groove parameters

The groove identification process generates a set of microgeometrical parameters that can now be analysed. The objective is to relate the measured surface and the intermediate surface to the Chapter 3 model which has a single value of each parameter. Figure 4.6 and Figure 4.7 show the distributions of the depth, the width and the angle.

Figure 4.6(a) and Figure 4.7(a) show the number of identified grooves for different depth ranges, where the depth correspond to the curve-fitted value (cf. Figure 4.3(c) and Figure 4.4(c)). The deepest identified grooves are $2.7\mu m$ and $2.2\mu m$ deep for receptively MST and BDC and the mean values are respectively $0.93\mu m$ and $0.66\mu m$.

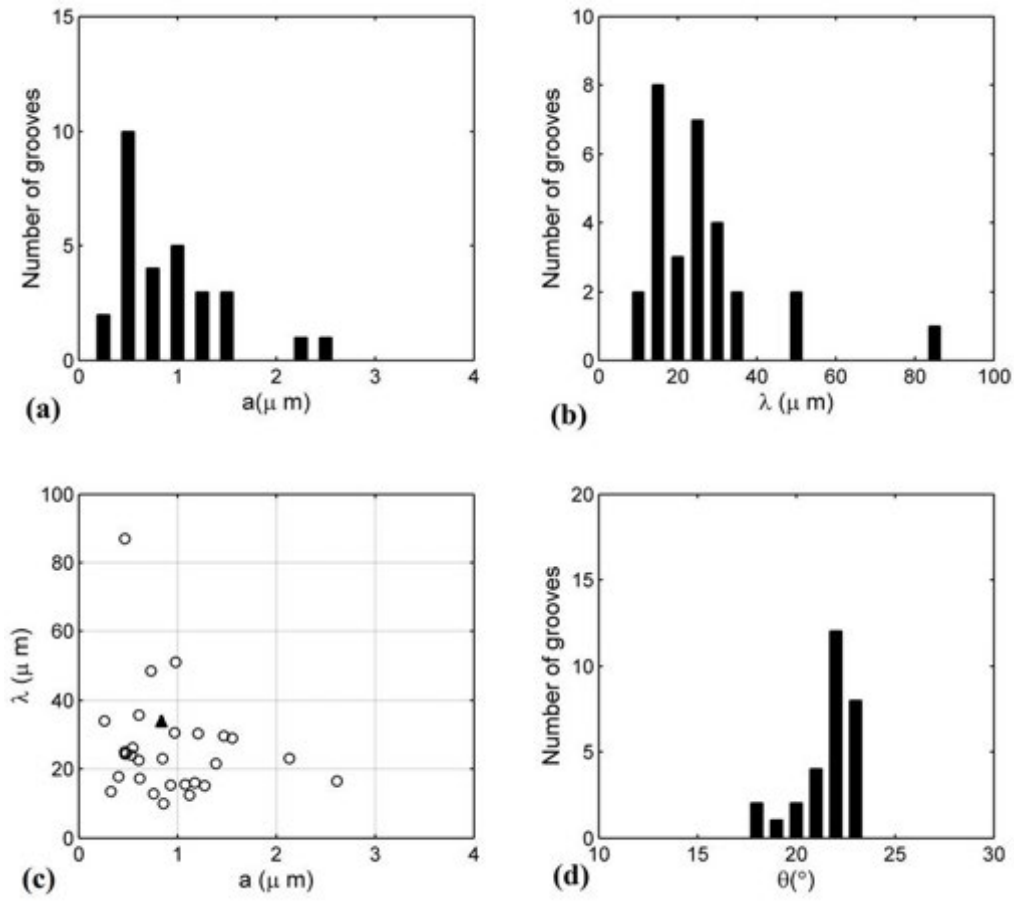

Figure 4.6: *MST grooves parameters: (a) Depth distribution (b) Width distribution (c) Width over depth slope distribution (d) Angle distribution*

For the width λ, Figure 4.6(b) and Figure 4.7(b) show the number of grooves identified. The mean value found after identification is around $30\mu m$ for both surfaces. Two very wide grooves of over $80\mu m$ wide are identified, one for each surface. For the MST, the groove is the large yellow colored groove at the right top of Figure 4.3(a). Actually, two grooves are in this location and very close to each other (as seen in measured surface Figure 4.3(b)). Both grooves are identified as one. For the BDC, the proximity of the picture corner affected the identification process.
Figure 4.6(c) and Figure 4.7(c) permit a better comparison between MST and BDC. They show the distribution of the width over depth (the inverse of the slope).
Figure 4.6(d) and Figure 4.7(d) concern the angle distribution. The average value is about 22° for both surfaces. Comparing the depth and the width distributions, other observations can be made:
- The drop of the number of the shallow grooves and also the number of narrow grooves is not physical. In fact, the groove identification is hard when its dimensions are close to the plateau roughness.
- There is a small shift to the left in width and depth values from the MST to BDC. In fact, the material removal, caused by the boundary lubrication regime in BDC, makes the grooves smaller (shallower and narrower).

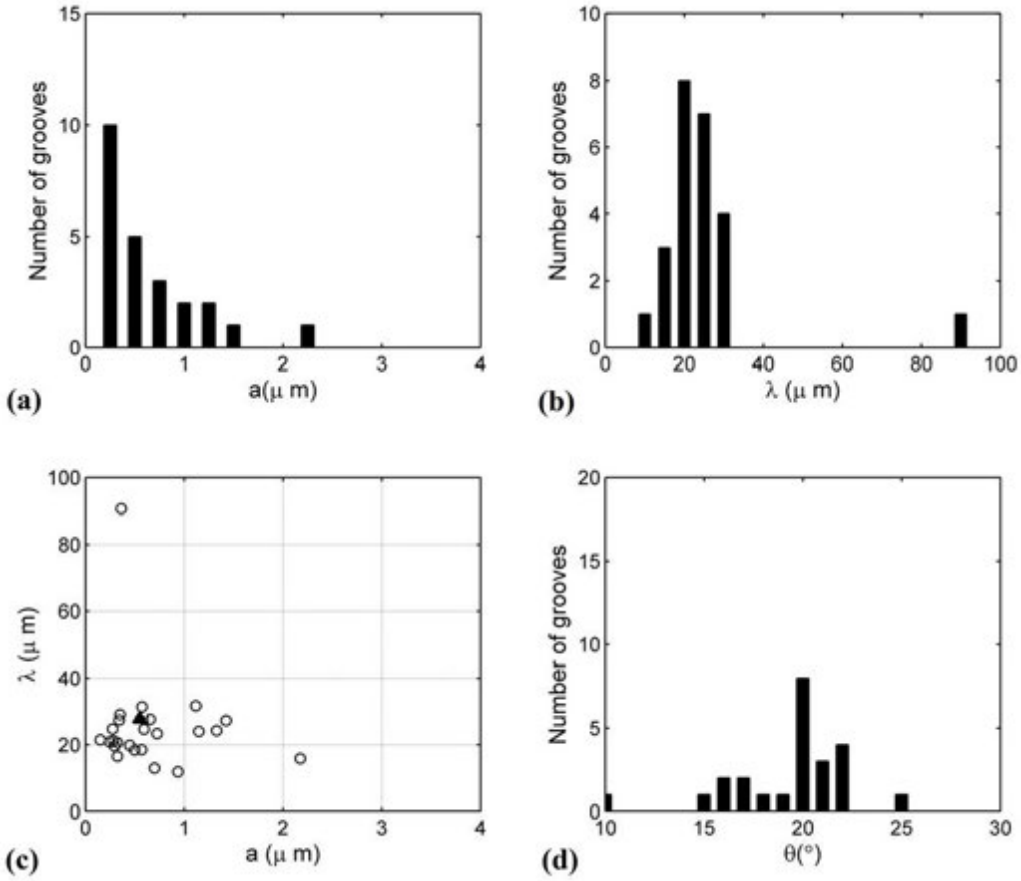

Figure 4.7: *BDC grooves parameters: (a) Depth distribution (b) Width distribution (c) Width over depth slope distribution (d) Angle distribution*

- Statistically, the number of the grooves is small. It only indicates a tendency, no generalization can be made.
- The angle distribution contains no particular information, unless the fact that the distribution is relatively wide (15° to 25°). This is due to the honing process.

There are several ways to combine parameters. The simplest way is to average the distributions. More complicated models can be considered including a combined interaction between different depth ranges, *etc.* In this study, the simplest model is chosen: an averaging of the microgeometry distribution.

To associate with each surface a single value of each of the parameters (zero sub script), one has to take into account the density of the grooves. In fact, to each groove i a density ϵ_i is associated ($\Sigma\epsilon_i \neq \epsilon_{total}$ due to cross-overs). The parameters are averaged using ϵ_i, for example $a_0 = \Sigma(\epsilon_i a_i / \Sigma\epsilon_i)$. The solid triangle marks in Figure 4.6 (c) and Figure 4.7 (c) represent this associated set of parameters. Table 4.2 resumes the set of parameters.

	MST	**BDC**
a_0	$0.848\mu m$	$0.590\mu m$
α_0	$21.98°$	$18.98°$
λ_0	$34.09\mu m$	$27.63\mu m$
ϵ_{tot}	54.10%	40.15%

Table 4.2: *Associated set of paramters*

	MST ($u_m = 4m/s$, $\eta = 0.012Pa.s$)				**BDC** ($u_m = 0.1m/s$, $\eta = 0.02Pa.s$)			
Surface	Smooth		Grooved		Smooth		Grooved	
BC	Periodic	Dirichlet	Periodic	Dirichlet	Periodic	Dirichlet	Periodic	Dirichlet
$h_0 = 0.25\mu m$	-	-	-	-	363	353 (3%)	266	254 (5%)
$h_0 = 0.5\mu m$	4066	3863(5%)	2803	2588(8%)	169	161 (5%)	139	130 (7%)
$h_0 = 1\mu m$	1776	1629(9%)	1405	1262(11%)	74	67 (10%)	65	59 (10%)
$h_0 = 1.5\mu m$	-	-	-	-	43	38 (12%)	39	35 (11%)
$h_0 = 2\mu m$	695	606(13%)	599	516(14%)	-	-	-	-
$h_0 = 4\mu m$	229	188(18%)	209	170(19%)	-	-	-	-

Table 4.3: *Comparison between the LCC generated in MST and BDC with Dirichlet BC and periodic BC for smooth surfaces and grooved ones (values of the LCC are in N/m and errors between parenthesis)*

4.3 Top ring

4.3.1 Boundary conditions

The Dirichlet BC for the lateral sides alters the pressure generation compared to an infinitely large 1D contact. It is obvious that for sufficiently distant boundaries, the Dirichlet BC have no influence on the central pressure in the contact (to avoid this problem Dalissier [DAL 12] duplicates the measured grooves to use periodic boundary conditions). The objective of this paragraph is to estimate the influence of Dirichlet BC. The smooth case is taken as a reference. Table 4.3 shows the load carrying capacity of a contact with Dirichlet BC compared with the infinitely large 1D contact for both smooth and grooved surface in MST and BDC. The grooves parameters correspond to table 4.2. The calculated LCC for Dirichlet BC cases is a time and y-direction averaged value. Only the center of the contact, $3/4^{th}$ of the domain width, is taken into account for comparison.
The error shown between parenthesis in Table 4.3 is less than 20% for the worst case. One can take less than $3/4^{th}$ of the domain width to ameliorate this value, but this will give less surface covered and fewer grooves analysed. The choice is to keep this value of $3/4^{th}$ for the next analysis and it is considered as sufficiently correct to evaluate the averaged LCC.

4.3.2 Film thickness-LCC relation

In this paragraph, three types of surfaces are compared with the prediction and the reference smooth case for both MST and BDC. The compared cases are:
- the measured rough surface noted MS (Figure 4.3(a) and Figure 4.4(a)),

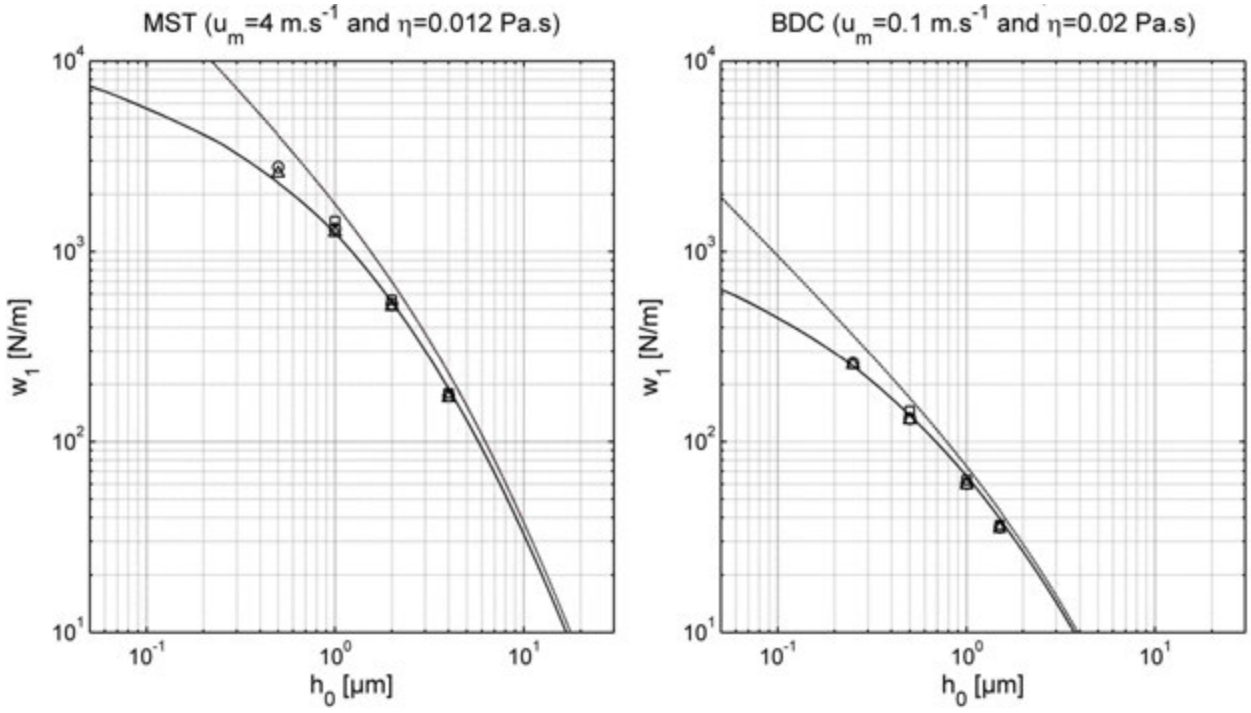

Figure 4.8: *The LCC for a parabolic ring (w_1) as a function of the film thickness (h_0) for MST and BDC conditions: (⊡) for MS,(○) for IS, (△) for AS, (solid line) for prediction and (dashed line) for 1D smooth.*

- the intermediate analytical surface with smooth plateaux and sinusoidal grooves noted IS shown in Figure 4.3(b) and Figure 4.4(b) (generated by groove identification),
- the analytical surface with a single set of parameters defined in Table 4.2 and noted AS (as in Chapter 3 model),
- the prediction which corresponds to the Chapter 3 prediction (Equation 3.12),
- the smooth line contact corresponding to Equation 3.3.

Transient hydrodynamic calculations are performed on the surfaces with $x_a = 400\,\mu m$ for four values of h_0 ($h_0 = 0.5, 1, 2, 4\,\mu m$ for MST and $h_0 = 0.25, 0.5, 1, 1.5\,\mu m$ for BDC). Knowing that the maximum roughness values are $0.8\,\mu m$ for MST and $0.34\,\mu m$ for BDC, only three values of h_0 are calculated on the measured surfaces. Actually, to avoid extremely thin films or asperity contact, the lowest value of h_0 calculated for the measured surfaces is $1\,\mu m$ for MST and $0.5\,\mu m$ for BDC. The mesh size that gives a sufficient accuracy is $\sim 0.78\,\mu m$.

Figure 4.8 shows the load carrying capacity as a function of the film thickness. The averaged values obtained by HL calculations are shown in this figure. The square is for MS, the circle for IS and the triangle for AS. The curves are, from bottom to top, the prediction and the smooth surface. Some observations are deduced:

- The three markers corresponds perfectly for large h_0 while for $1\,\mu m$ at MST and for $0.5\,\mu m$ at BDC the measured surface (MS) has slightly higher LCC. In fact when approaching the plateaux roughness, the peaks influence the pressure profile in a non linear manner. Figure 4.9 shows an example of these peak effects. Since the final result is averaged over time, this effect vanishes or at least is greatly reduced. Table 4.4 details the calculated values and the

	MST ($u_m = 4m/s$, $\eta = 0.012Pa.s$)					**BDC** ($u_m = 0.1m/s$, $\eta = 0.02Pa.s$)				
Surfaces	Sm.	MS	IA	AS	Pred.	Sm.	MS	IA	AS	Pred.
$h_0 = 0.25\mu m$	-	-	-	-	-	363	-	259	245	250
error	-	-	-	-	-	+45%	-	+3%	+1%	-
$h_0 = 0.5\mu m$	4066	-	2785	2588	2294	169	145	132	130	137
error	+77%	-	+21%	+12%	-	+23%	+5%	−4%	−6%	-
$h_0 = 1\mu m$	1776	1446	1312	1262	1256	74	63	60	59	66
error	+41%	+15%	+5%	+0%	-	+12%	−5%	−10%	−11%	-
$h_0 = 1.5\mu m$	-	-	-	-	-	43	36	35	35	39
error	-	-	-	-	-	+10%	−8%	−11%	−11%	-
$h_0 = 2\mu m$	695	557	531	516	574	-	-	-	-	-
error	+27%	+1%	−3%	−6%	-	-	-	-	-	-
$h_0 = 4\mu m$	232	179	174	170	189	-	-	-	-	-
error	+17%	−10%	−13%	−15%	-	-	-	-	-	-

Table 4.4: *Comparison of LCC for MST and BDC conditions, for MS (measured surface), IS(intermediate surface), AS (analytical surface), prediction (Pred.)and 1D smooth(Sm.).*

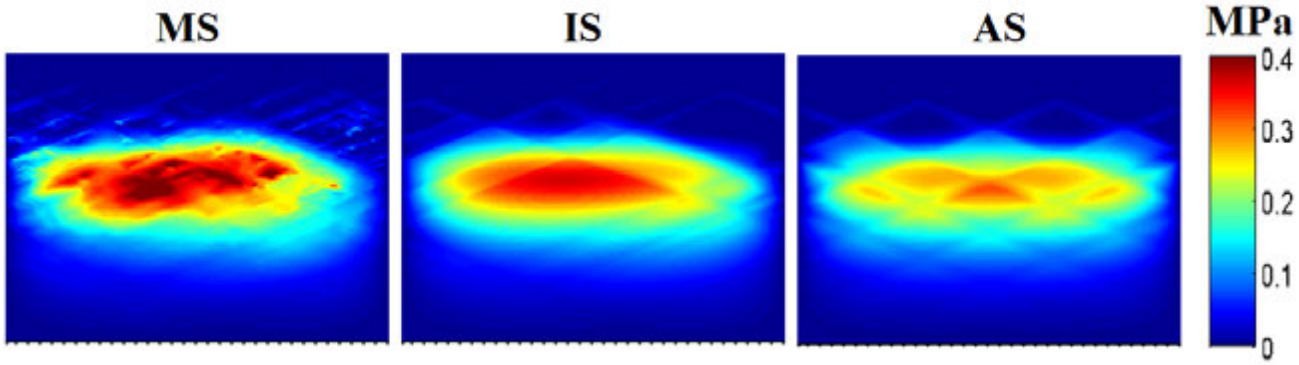

Figure 4.9: *Pressure distribution in MST with $h_0 = 1\mu m$ at $t = \Delta t$ (surfaces left to right: MS, IS and AS).*

error relative to prediction.

- The pressures for the measured surface (⊡) are higher than those of the intermediate analytical surfaces (○). This is mainly due to the bad height location of the plateaux in certain areas. Even with this error the approximation is still good enough to correctly model the performance of the measured surface.

- Comparing the analytical surfaces (△) and the intermediate analytical surfaces (○) permits to validate the associated set of parameters (Table 4.2). Table 4.4 reports the values of LCC. It is concluded that the averaging done to obtain these parameters is sufficient to approximate the surface. It is worth noting that for a surface that contains a sparser distribution or with one very deep groove the same approach as previous will be less accurate. In fact, one should give more weight to deep grooves.

- The difference between the calculated analytical surfaces (△) and the prediction (bottom line) is less than 15% (in absolute value). This difference is due to the curve-fitting and is

considered acceptable.

4.4 Oil control ring

4.4.1 Boundary conditions

As for the parabolic shaped ring, the flat ring is analysed. The measured surface is also compared to predicted results. These calculations are performed for the same values of h_0 as the parabolic ring (for MST $h_0 = 0.5$, 1, $2, 4\,\mu m$ and for BDC $h_0 = 0.25$, 0.5, 1, $1.5\,\mu m$). The same mesh size as top ring is used for calculations ($\sim 0.78\,\mu m$).
The surfaces are the same as in the parabolic shaped ring case. The calculations are stationary and the whole surface is calculated at once. The whole domain is $1070\mu m$ long. The resulting LCC is calculated proportionally for $x_b - x_a = 400\mu m$ ($\times 400/1070$). The boundary conditions in $x = x_a$ and $x = x_b$ can alter this proportionality but this is simply neglected. The results are shown in Figure 4.10 for a $400\mu m$ land, corresponding to a single land length of a twin land OCR. In this figure the square is for MS ($\boxdot$),the circle for IS ($\circ$), triangle for AS ($\triangle$),plus sign for Analytical and periodic BC ($+$) and the prediction is a solid line.
The triangle markers and the cross markers fit perfectly. They correspond to the analytical surface with respectively Dirichlet and periodic BC. In fact, with flat rings the effect of the zero pressure boundaries vanishes rapidly, as for a given film height the pressure generation is much less than for the parabolic ring.

4.4.2 Film thickness-LCC relation

The comparison between different surfaces is done gradually from the prediction to the measured surface.
- Prediction (solid line) vs Analytical Surface AS($\triangle$)
Using the set of parameters defined in Table 4.2 for MST and for BDC, and then respectively equation 3.16, equation 3.15 and also an interpolation function of the N number, one can obtain the w_1 - h_0 relation. This prediction is shown in solid lines in Figure 4.10. The prediction line is about 40% higher than the analytical values for the MST and 20% for BDC. This is due to the combined action of the approximation of the boundary conditions in sliding direction and the curve-fitting.
- Analytical Surface AS($\triangle$) vs Intermediate Surface IS ($\circ$)
The set of parameters defined in Table 4.2 remained the same for the analytical surface despite the fact that the pressure generation for flat ring is more complicated than for parabolic rings. In fact, when the range of the film thickness variation is relatively large, the grooves that are carrying most of the load are different in each region of this range which contradicts the simplification to use a single set of parameters. MST in Figure 4.10 illustrates this fact, for $h_0 = 0.5\,\mu m$ and $h_0 = 1\,\mu m$ AS and IS load carrying capacities correspond, while for $h_0 = 2\,\mu m$ and $h_0 = 4\,\mu m$ an error starts to form. The averaged value of the depth is $0.848\,\mu m$ while there are two grooves of more than $2\,\mu m$ deep. These deep grooves generate more pressure than those of $0.848\,\mu m$ depth around the film thickness of $2\,\mu m$. The same fact can be observed in BDC, the error is greater when the film thickness is greater.
- Intermediate Surface IS($\circ$) vs Measured Surface MS ($\boxdot$)

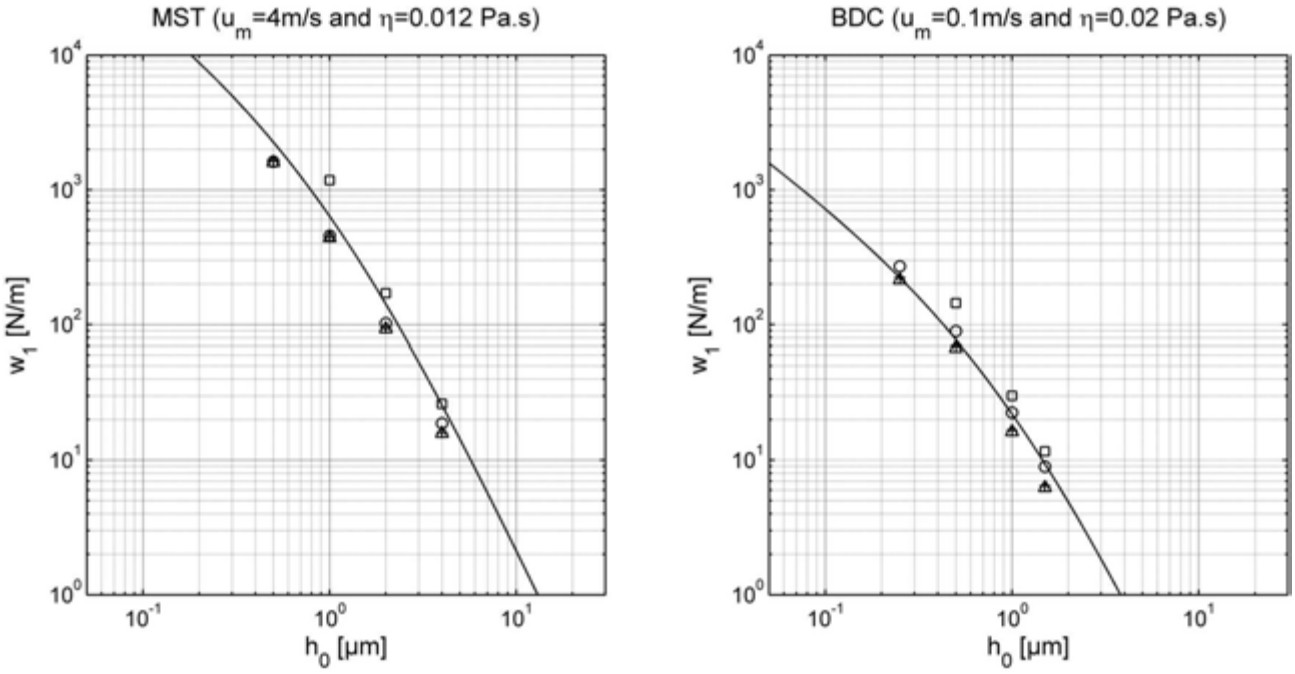

Figure 4.10: *The LCC of a flat ring as a function of the film thickness h_0 in MST and BDC conditions: (⊡) for MS,(○) for IS, (△) for AS, (+) for Analytical and periodic BC, (solid line) for Prediction.*

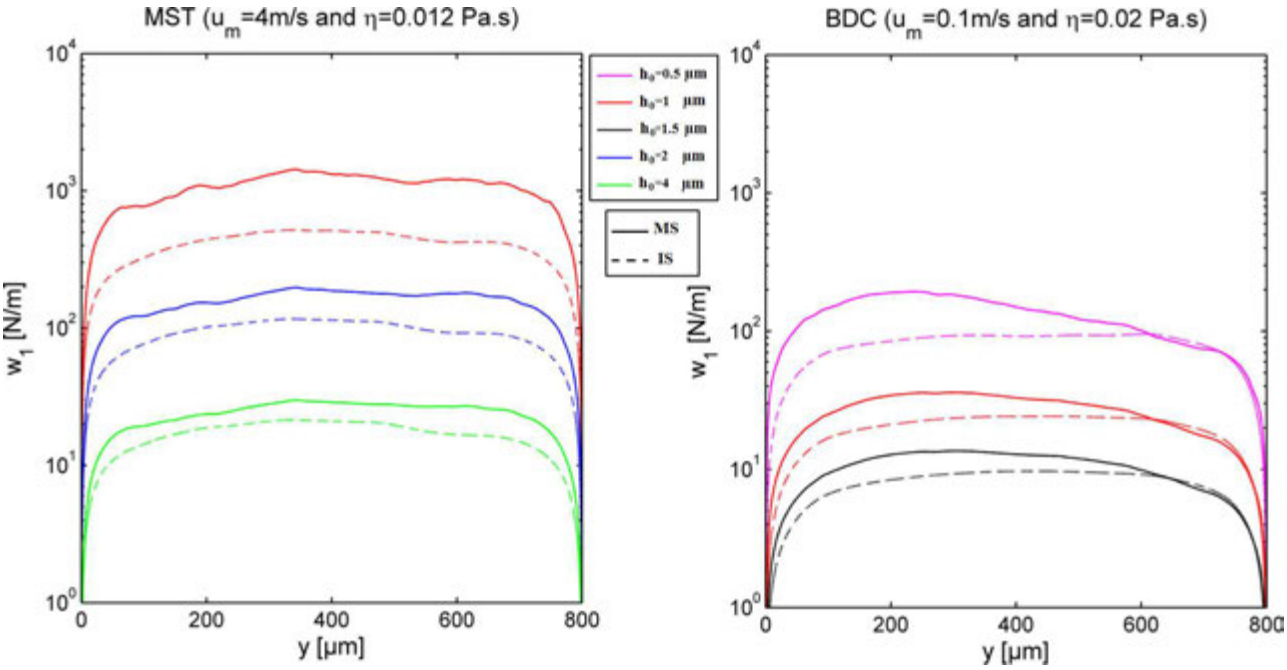

Figure 4.11: *The LCC as a function of y for MST (top to bottom $h_0 = 1, 2, 4$) and BDC (top to bottom $h_0 = 0.5, 1, 1.5$) and for both measured surfaces and intermediate surfaces (top to bottom).*

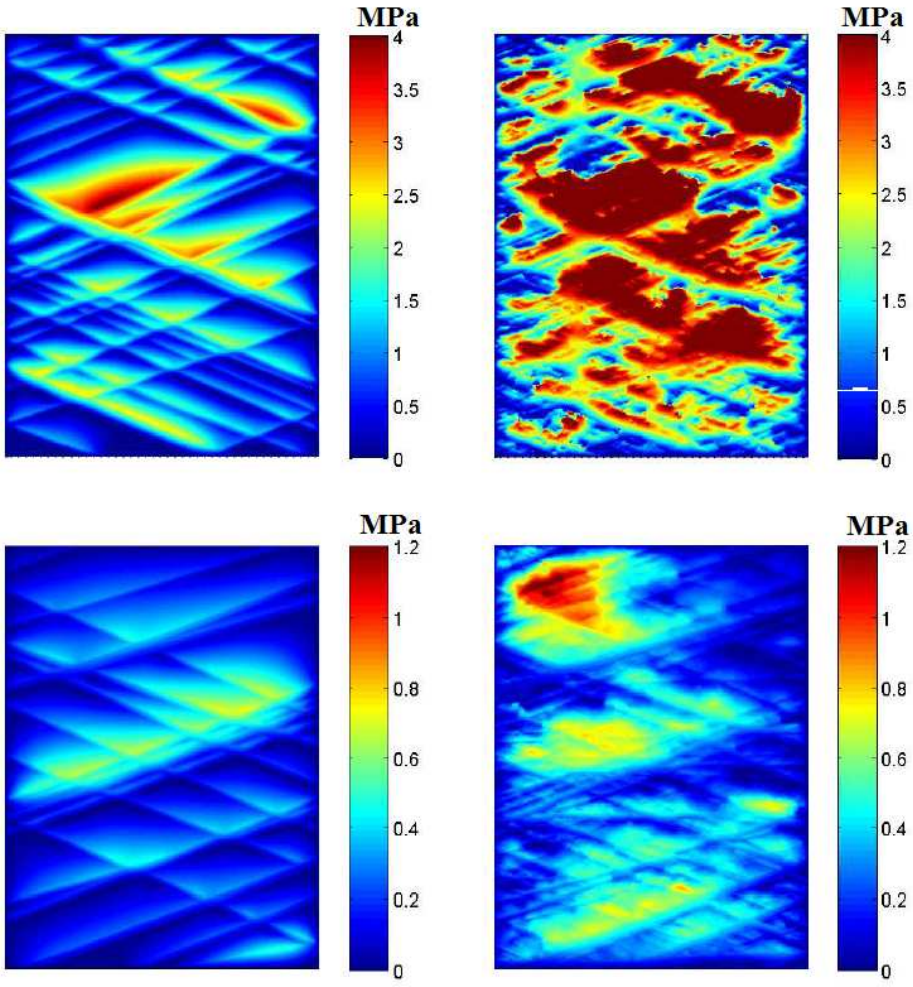

Figure 4.12: *Pressure profiles in MST (top, $h_0 = 1\mu m$) and BDC (bottom, $h_0 = 0.5\mu m$) for Intermediate Surface (left) and Measured Surface (right)*

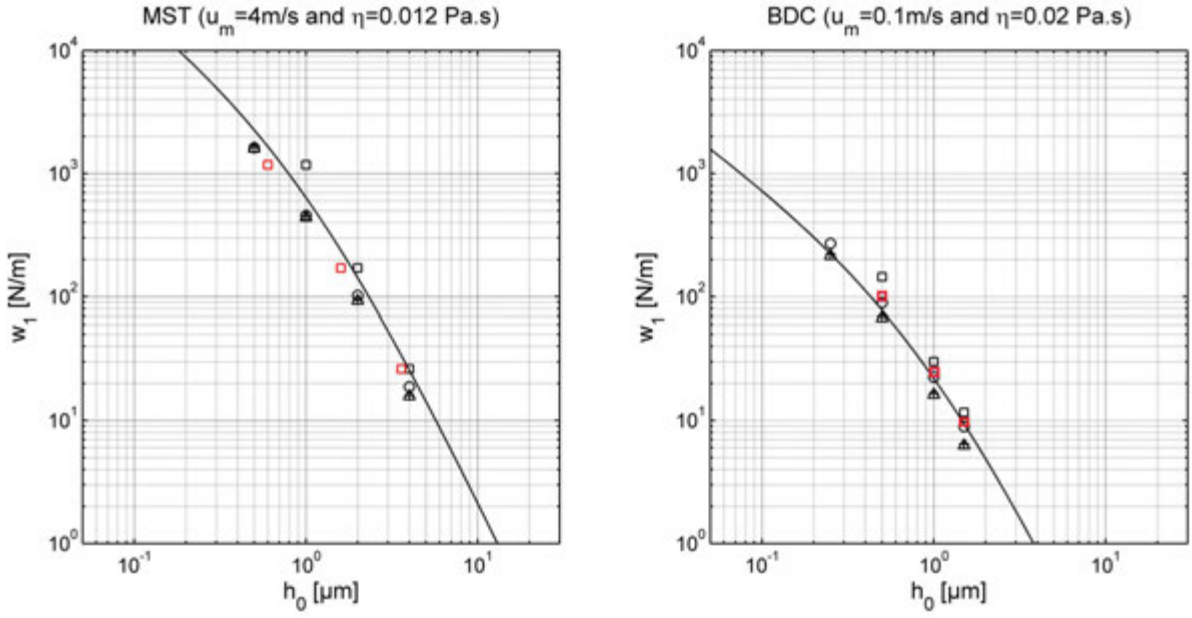

Figure 4.13: *Corrections in w_1-h_0 relation due to the plateau position (red) and to the deep grooves (blue)*

To compare the measured surface (squares) with the intermediate corresponding surface (circles), one has to visualize the LCC as a function of the longitudinal abscissa y (Figure 4.11) and then for more details the pressure profile (Figure 4.12) and keeping in mind the roughness profiles (Figure 4.3 and Figure 4.4).

Two observations concerning the origin of the difference between circles (IS) and squares (MS) in Figure 4.10:

- for MST, Figure 4.11 shows that the shape is approximately the same but there is a global shift of the LCC. Figure 4.12 shows that the pressure is everywhere higher by a certain factor. The shift becomes bigger when approaching the surface as if the plateaux in measured surface are higher. In fact, this can be explained by the incorrect location of the plateau globally (explained previously in subsection 4.2.2.2). Visualizing Figure 4.3 suggests a $+0.4\mu m$ shift of the plateau. This shift, if applied to the LCC-h_0 curve gives the red squares in Figure 4.13. With this correction, the squares (MS) perfectly follow the slope of the circles (IS).
- for BDC, Figure 4.11 shows that in addition to a very small global shift there is a bump on the left of the curve that is exceeding the mean value. Figure 4.12 shows at the top left corner that the pressure generated is relatively high. In fact, exactly at this location, there is a very deep groove with a $8\mu m$ measured depth (cf. Figure 4.4). The flat ring LCC is very sensitive to this kind of grooves, it generates over-pressure. This perturbation can be eliminated with considering only the right half of the surface. The corrected values are in red squares in Figure 4.13. This correction permits to fit the squares (MS) to the circles (IS).

4.5 Conclusion

The main objective of this chapter is to validate predictions of chapter 3 via measured surface calculations. The major difference between the analytical model (used for prediction) and the measured model is the microgeometry. The first one has smooth plateaux and the second has rough and wavy plateaux. The first one also has a unique set of groove parameters while the second has a distribution of grooves that are not uniform. For the comparison of the surfaces, a procedure was used to extract microgeometrical parameters from the measured surfaces. The parameters distribution has been studied. Thus, the extracted data was linked to a unique set of parameters. This single set was used for prediction, according to Chapter 3 predictions, permitting then a comparison with the measured surface results. The performance of the parabolic ring and the flat ring in term of load carrying capacity (LCC) in a measured surface was compared to the corresponding prediction for two kind of surfaces (located at midstroke and at bottom dead center). This comparison led to the prediction validation. The prediction is an instantaneous way to approximate the LCC for a large range of film thickness and starvation degree, while a transient code will run for 24 hours even with the efficient multigrid method for only a single value of film thickness and a single starvation condition.

Conclusion

The understanding of the phenomena that are acting in piston ring cylinder liner (PRCL) contact permits the enhancement of the whole engine performance, reducing the oil consumption and respecting the environment constraints. In fact, the PRCL contact contributes to more than 30% of the energy loss by friction and contributes also to the lubricant consumption.
The liner texturing is of great importance in the PRCL contact and consequently to the tribological performance. It influences the film thickness, acting on ring behaviour. The liner surface features a special microgeometry. The scope of the thesis is to study the effect of this particular microgeometry on the load carrying capacity- film thickness relation.
The texturing that is the most common is the cross-hatching pattern obtained by the honing process. This texturing is highly directional with two major components: the plateaux and the cross-hatched grooves. Statistical methods such as the Patir and Cheng method are not able to distinguish both components. The deterministic method is a straightforward method to analyse the effect of such a microgeometry. The correct description of the surface needs a large number of points. Classical solution methods such as Jacobi or Gauss Seidel relaxation are too slow to permit a reasonable computing time. An efficient and robust method does exist and is the Multigrid method. The use of the Multigrid method drastically reduces the computing time.
The PRCL model starts by distinguishing the flat ring (oil control ring precisely) and the parabolic shaped rings (top ring and scrapper ring: compression rings). The liner surface is modelled by three different models: the first is the classical smooth surface which has been widely studied, the second is the analytical surface which is a simplified model that assumes periodicity of the geometry with smooth plateaux, the third model is the measured surface. A code based on multigrid methods is developed. It permits a fast 2D transient hydrodynamic calculations, taking into account the microgeometry. This code permits, via an analytical surface model, to perform more than 2000 transient calculations for the top ring and more than 1000 calculations for the flat ring. This parametric study, takes into account the different parameters defining the microgeometry notably the groove depth, the groove width, the groove angle and the groove density. It also considers the starvation degree. These calculations serve to predict via analytical expression the load carrying capacity as a function of the different parameters and the starvation degree. Predictions for compression ring and the oil control ring load carrying capacity are build. These predictions reinforce the idea that the pressure generation is very different for both cases. In fact, for the top ring the grooves contribute only in the load carrying capacity decrease and for the OCR the grooves generate the load carrying capacity.
The measured surface calculations permit the validation of these predictions. To link both models, a procedure that identifies cross-hatched grooves is used. The obtained information

is analysed and a single set of parameters is deduced. This set is used for prediction. Thus, both results can be compared. This comparison led to the prediction validation.
Some perspectives and future work can be considered:

- Short term perspectives:
  - Experiments should be held to validate the predictions with a test campaign including sufficient surface measurements for various liners and various positions. The experiments should start by differentiating the flat case and the parabolic case since the mechanism that generates the pressure is not the same.
  - The study of the case of a huge radius R_x will link between both models.

- Mid-term perspectives:
  - The starvation remains an important problem that is not well understood or quantified in textured surfaces. It should be detailed more and more.
  - One of the problems that are related to multigrid method is the coarse grid introduced error. The microgeometry is not well described by this grid. More suitable description should be found (cf. Alcouffe et al. [ALC 81] and Noutary et al. [NOU 12]).

Bibliography

[ALC 81] Alcouffe R., Brandt A., Dendy J. J., Painter J.
The multi-grid method for the diffusion equation with strongly discontinuous coefficients. *SIAM J. Sci. Statist. Comp.*, vol. 2, 1981, Page 430.

[ALM 11] Almqvist A.
Homogenization of the Reynolds equation governing hydrodynamic flow in a rotating device. *Journal of tribology*, vol. 133, 2011.

[AUS 13] Ausas R., Jai M., Ciuperca I., Buscaglia G.
Conservative one-dimensional finite volume discretization of new cavitation model for piston ring lubrication. *Tribology international*, vol. 57, 2013, p. 54-66.

[BAY 05] Bayada G., Martin S., Vasquez C.
An average flow model of the Reynolds roughness including a mass-flow preserving cavitation model. *Transactions of the ASME, Journal of tribology*, vol. 127, 2005, p. 793-802.

[BEH 12] Beheshti A., Khonsari M.
Asperity micro-contact models as applied to the deformation of rough line contact. *Tribology International*, vol. 52, 2012, p. 61-74.

[BIB 10a] Biboulet N., Houpert L.
Hydrodynamic force and moment in pure rolling lubricated contacts. Part 1: line contacts. *Proc. IMechE Part J: Journal of Engineering Tribology*, vol. 224, 2010, p. 765-775.

[BIB 10b] Biboulet N., Houpert L.
Hydrodynamic force and moment in pure rolling lubricated contacts. Part 2: point contacts. *Proc. IMechE Part J: Journal of Engineering Tribology*, vol. 224, 2010, p. 777-787.

[BIB 13] Biboulet N., Colin F., Lubrecht A.
Friction in starved hydrodynamically line lubricated contacts. *Tribology International*, vol. 58, 2013, p. 1-6.

[BIB 14a] Biboulet N., Bouassida H., Cavoret J., Lubrecht A.
Determination of fundamentals parameters of the cross-hatched cylinder liner micro-geometry. *Proc. IMechE Part J: Journal of Engineering Tribology*, , 2014.

[BIB 14b] Biboulet N., Bouassida H., Lubrecht A.
Cross hatched texturing influence on the load carrying capacity of an OCR. *Tribology International*, , 2014.

[BOL 05] Bolander N., Steenwyk B., Sadeghi F., Gerber G.
Lubrication regime transitions at the piston ring-cylinder liner interface. *Proc. IMechE Part J: Journal of Engineering Tribology*, vol. 219, 2005, p. 19-31.

[BOU 14] Bouassida H., Biboulet N., Sainsot P., Lubrecht A.
Piston ring load carrying capacity: Influence of cross-hatching parameters. *Proceedings of the Institution of Mechanical Engineers, Part J: Journal of Engineering Tribology*, , 2014, Page 1350650114522779, SAGE Publications.

[BRA 77] Brandt A.
Multi-level adaptive solutions to boundary-value problems. *Mathematics of computation*, vol. 31, n° 138, 1977, p. 333–390.

[BRI 87] Briggs W.
A Multigrid tutorial. SIAM, 1987.

[BRI 00] Briggs W., Henson V., McCormick S.
A multigrid Tutorial- Second Edition. SIAM, 2000.

[BRU 86] Brun R.
Science et technique du moteur diesel industriel et de transport. Editions OPHRYS, 1986.

[CAC 06] Caciu C.
Analyse et optimisation des surfaces des chemises de moteurs thermiques. cole nationale suprieure des mines (Paris), PhD thesis, 2006.

[CAS 98] Casey S. M.
Analysis of lubricant film thickness and distribution along the piston-ring/liner interface in a reciprocating engine. Massachusetts Institute of Technology, Master thesis, 1998.

[CHA 10] Charles P.
Rhologie double-newtonienne dans le contact segment-piston-chemise. INSA de Lyon, PhD thesis, 2010.

[CHE 08] Chen H.
Modeling of liner finish effects on oil contro lring lubrication in internal combustion engines based on deterministic method. Massachusetts Institute of Technology, Master thesis, 2008.

[CHE 11] Chen H.
Modeling the lubrication of the piston ring pack in internal combustion engines using the deterministic method. Massachusetts Institute of Technology, PhD thesis, 2011.

[COM 03] Comfort A.
An Introduction to Heavy-Duty Diesel Engine Frictional Losses And Lubricant Properties Affecting Fuel Economy Part I. *SAE Technical Paper 2003-01-3225*, , 2003.

[DAL 12] Dalissier E.
Optimisation des tats de surface et nouveau modle de cavitation pour un coulement lubrifi. INSA de Lyon, PhD thesis, 2012.

[DOB 09] Dobrica M., Fillon M.
About the validity of Reynolds equation and inertia effects in textured sliders of infinite width. *Proceedings of the Institution of Mechanical Engineers, Part J: Journal of Engineering Tribology*, vol. 223, n° 1, 2009, p. 69–78, SAGE Publications.

[DOB 10] Dobrica M., Fillon M., Pascovici M., Cicone T.
Optimizing surface texture for hydrodynamic lubricated contacts using a mass-conserving numerical approach. *Proceedings of the Institution of Mechanical Engineers, Part J: Journal of Engineering Tribology*, vol. 224, n° 8, 2010, p. 737–750, SAGE Publications.

[DOB 12] Dobrica M., Fillon M.
Performance degradation in scratched journal bearings. *Tribology International*, vol. 51, 2012, p. 1–10, Elsevier.

[DOW 95] Dowson D.
Elastohydrodynamic and micro-elastohydrodynamic lubrication. *Wear*, vol. 190, 1995, p. 125-138.

[ETS 05] Etsion I.
State of the Art in Laser surface texturing. *Journal of tribology*, vol. 127, 2005, p. 248-253.

[FEL 07] Felter C.
Lubrication of Piston rings in large 2 and 4 stroke Diesel engines. Technical university of Denmark, 2007.

[FRE 90] Frene J., Nicolas D., Degueurce B., Berthe D., Godet M.
Lubrification hydrodynamique. Collection de la Direction des Etudes et Recherches dElectricit de France, 1990.

[GAD 02] Gadelmawla E.S.and Koura M., Maksoud T., Elewa I., Soliman H.
Roughness Parameters. *Journal of material processing technology*, vol. 123, 2002, p. 133-145.

[GAM 03] Gamble R., Priest M., Taylor C.
Detailed analysis of oil transport in piston asssembly in gasoline engine. *Tribology Letters*, vol. 14, 2003, p. 147-156.

[GOS 07] Goswami D. Y., Kreith F.
Handbook of energy efficiency and renewable energy. Crc Press, 2007.

[GRA 10] Grabon W., Pawlus P., Sep J.
Tribological characteristics of one-process and two-process cylinder liner honed surfaces under reciprocating sliding conditions. *Tribology International*, vol. 43, 2010, p. 1882-1892.

[GRE 66] Greenwood J. A., Williamson J. B. P.
Contact of Nominally Flat Surfaces. *Proceedings of the Royal Society A*, vol. 295, 1966, p. 300-319.

[GRE 70] Greenwood J., Tripp J.
The contact of two nominally flat rough surface. *Proceedings of the Institution of Mechanical Engineers*, vol. 185, 1970, p. 625-633.

[GRE 82] Greenwood J.
The contact of real surfaces. *Proceedings of International Symposium on Contact Mechanics and Wear of Wheel/Rail Systems, University of British Columbia, Vancouver, Canada*, vol. ., 1982, p. 21-37.

[HEY 88] Heywood J. B.
Internal combustion engine fundamentals. Mc Graw-Hill, 1988.

[HU 94] Hu Y., Cheng H., Arai T., Kobayashi Y., S. A.
Numerical simulation of piston ring in mixed lubrication - A Nonaxiseymmetrical analysis. *Journal of tribology*, vol. 116, 1994, p. 470-478.

[JEN 96] Jeng Y.
Impact of plateaued surfaces on tribological performance,. *STLE Tribology Transactions*, vol. 39, No. 1, 1996, p. 351-361.

[JIA 09] Jia K.
A coupled model for ring dynamics, gas flow, and oil flow through the ring grooves in IC engines. Massachusetts Institute of Technology, Master thesis, 2009.

[JOC 05] Jocsak J.
The effects of surface finish on piston ring-pack performance in advanced reciprocating engine systems. Massachusetts Institute of Technology, Master thesis, 2005.

[JOH 08] Johansson S., Nilsson P., Ohlsson R., Anderberg C., Rose'n B.
New cylinder liner surfaces for low oil consumption. *Tribology International*, vol. 41, 2008, p. 854-859.

[KLI 05] Kligerman Y., Etsion I., Shinkarenko A.
Improving tribological performance of piston rings by partial surface texturing. *Transaction ef the ASME, Journal of Tribology,*, vol. 127, 2005, p. 632-638.

[KOV 05] Kovalchenko A., Ajayia O., Erdemira A., Fenskea G., Etsion I.
The effect of laser surface texturing on transitions in lubrication regimes during unidirectional sliding contact. *Tribology International*, vol. 38, 2005, p. 219-225.

[LAR 09] Larsson R.
Modelling the effect of surface roughness on lubrication in all regimes. *Tribology International*, vol. 42, 2009, p. 512-516.

[LEC 07] Lecompte M.
Etude exprimentale des sprays d'huile dans un moteur combustion interne : Influence de lcoulement de blow-by et participation la consommation dhuile. La facult des sciences et techniques de l'universit de Rouen, 2007.

[LI 11] Li Y.
Multiphase oil transport at complex micro geometry. Massachusetts Institute of Technology, PhD thesis, 2011.

[LIA 13] Liao K., Liu Y., Kim D.and Urzua P., Tian T.
Practical challenges in determining piston ring friction. *Proc. IMechE Part J: Journal of Engineering Tribology*, vol. 227(2), 2013, p. 112-125.

[LIU 01] Liu K., Tonder K.
The behaviour of inlet roughness in lubrication of piston ring-cylinder liner. *Science in China (Series A)*, vol. 44, 2001, p. 14-19.

[MA 01] Ma C., Zhu H.
An optimum design model for textured surface with elliptical-shape dimples under hydrodynamic lubrication. *Tribology International*, vol. 44, 2001, p. 987-995.

[MCC 21] McCoull N., Walther C.
Viscosity-temperature chart. *Lubrication, June*, , 1921.

[MCC 86] McCool
Comparaison of models for the contact of rough surfaces. *Wear*, vol. 107, 1986, p. 37-60.

[MCC 07] McClure F.
Numerical modeling of piston secondary motion and skirt lubrication in internal combustion engines. Massachusetts Institute of Technology, 2007.

[MEZ 12] Mezghani, Demirci, Zahouani, Mansori E.
The effect of groove texture patterns on piston-ring pack friction. *Precision Engineering*, vol. 36, 2012, p. 210-217.

[MEZ 13] Mezghani, Demirci, ElMansori, Zahouani
Energy efficiency optimization of engine by frictional reduction of functional surfaces ofcylinderringpacksystem. *Tribology International*, vol. 59, 2013, p. 240-247.

[MIC 95a] Michail S. K., Barber G. C.
The effects of roughness on piston ring lubrication- Part 1: Model development. *STLE Tribology Transactions.*, vol. 38,, 1995, p. 19-26.

[MIC 95b] Michail S. K., Barber G. C.
The effects of roughness on piston ring lubrication- Part 2: The relationship between cylinder wall surface topography and oil film thickness. *STLE Tribology Transactions.*, vol. 38,, 1995, p. 193-177.

[MIC 11] Michalski, Wos
The effect of cylinder liner surface topography on abrasive wear of pistoncylinder assembly in combustion engine. *Wear*, vol. 271, 2011, p. 582-589.

[MIL 02] Millar C., Asenov A., Watling J.
Excessive over-relaxation method for multigrid poisson solvers. *Journal of Computational Electronics,*, vol. 1 (3)., 2002, p. 341-345.

[MIS 12] Mishra P. C.
Tribodynamic modeling of piston compression ring and cylinder liner conjunction in high-pressure zone of engine cycle. *International Journal of Advanced Manufacturing Technology.*, vol. 66(5-8), 2012, p. 1075-1085.

[MOE 00] Moes H.
Lubrication and beyond. *UT lecture notes*, , n° 115531, 2000.

[MOR 97] Mortier R., Orszulik S.
Chemistry and technology lubricants. Blackie academic & professional, 1997.

[NOU 12] Noutary M., Venner C., Lubrecht A.
Grid generation in HL and EHL using AMG. *Proc. IMechE Part J: Journal of Engineering Tribology*, vol. 226(5), 2012, p. 343-349.

[ORG 07] Organisciack M.
Optimisation de la microgomtrie des chemises des moteurs combustion interne. INSA de Lyon, PhD thesis, 2007.

[PAS 09] Pascovici M., Cicone T., Fillon M., Dobrica M.
Analytical investigation of a partially textured parallel slider. *Proceedings of the Institution of Mechanical Engineers, Part J: Journal of Engineering Tribology*, vol. 223, n° 2, 2009, p. 151–158, SAGE Publications.

[PAT 78] Patir N., Cheng H.
An Average Flow Model for Determining Effects of Three-Dimensional Roughness on Partial Hydrodynamic Lubrication. *Transaction ef the ASME, Journal of Lubrication Technology*, vol. 100, 1978, p. 12-17.

[PAT 79] Patir N., Cheng H.
Application of average flow model to lubrication between rough sliding surfaces. *Transaction ef the ASME, Journal of Lubrication Technology*, vol. 101, 1979, p. 220-229.

[PAW 11] Pawel Wos J. M.
Effect of Initial Cylinder Liner Honing Surface Roughness on Aircraft Piston Engine Performances. *Tribology Letters*, vol. 41, 2011, p. 555-567.

[PET 83] Petrov N.
Friction in Machines and the Effect of the Lubricant. *Inzherernii Zhurnal*, vol. 1, 1883, p. 71–140.

[PRI 99] Priest M., Dowson D., Taylor C.
Predictive wear modelling of lubricated piston rings in a diesel engine. *Wear*, vol. 231, 1999, p. 89-101.

[PRI 00] Priest M., Taylor C.
Automobile Engine Tribology- Approaching the Surface. *Wear*, vol. 241, 2000, p. 193-203.

[RAB 01] Rabut R., Tian T.
Challenges involved in piston top ring designs for modern SI engines. *Trans. ASME, Journal of engineering for gas turbines and power*, vol. 123(2),, 2001, p. 448-459,.

[RAH 07] Rahmani R., Shirvani A., Shirvani H.
Optimization of partially textured parallel thrust bearings with square-shaped micro-dimples. *Tribology Transactions*, vol. 50, n° 3, 2007, p. 401–406, Taylor & Francis.

[RAM 13] Ramesh, Akram, Mishra, Cannon, Polycarpoua, King
Friction characteristics of microtextured surfaces under mixed and hydrodynamic lubrication. *Tribology International*, vol. 57, 2013, p. 170-176.

[REY 86] Reynolds O.
On the Theory of Lubrication and Its Application to Mr. Beauchamp Tower's Experiments, Including an Experimental Determination of the Viscosity of Olive Oil. *Proceedings of the Royal Society of London*, vol. 40, n° 242-245, 1886, p. 191–203, The Royal Society.

[RIC 00] Richardson D. E.
Review of Power Cylinder Friction for Diesel Engines. *Transactions of the ASME,Journal of Engineering for Gas Turbines and Power*, vol. 122, 2000, p. 506-519.

[ROH 80] Rohde S.
A mixed friction model for dynamically loaded contacts with application to piston ring lubrication. *Proceedings of the 7th Leeds lyon Symposium on Tribology, Westbury house*, vol. 262, 1980, p. 355-365.

[RON 01] Ronen A., Etsion I., Kligerman Y.
Friction -reducing surface texturing in reciprocating automotive components. *STLE Tribology Transactions*, vol. 44, 2001, p. 359-366.

[SAB 10] Sabri L.
Dvelopement et mise en oeuvre d'une mthodologie d'analyse multi-chelle du procd de rodage en production de srie. Ecole Nationale Suprieure d'Arts et Mtiers, 2010.

[SAH 05a] Sahlin F.
Hydrodynamic Lubrication of rough surfaces. Lulea university of Technology Sweden, PhD thesis, 2005.

[SAH 05b] Sahlin F., Almqvist A., Glavatskih S., Larsson R.
Two-dimensional CFD-Analysis of micro-patterned surfaces in hydrodynamic lubrication. *Journal of tribology*, vol. 127, 2005, p. 96-102.

[SAH 07a] Sahlin F., Almqvist A., Larsson R., Glavatskih S.
A cavitation algorithm for arbitrary lubricant compressibility. *Tribology International*, vol. 40, 2007, p. 1294-1300.

[SAH 07b] Sahlin F., Almqvist A., Larsson R., Glavatskih S.
Rough surface flow factors in full film lubrication based on a homogenization technique. *Tribology International*, vol. 40, 2007, p. 1025-1034.

[SEN 07] Senzer E.
Piston ring pack design effect on production spark ignition engine oil consumption: A simulaton analysis. Massachusetts Institute of Technology, Master thesis, 2007.

[SEN 12] Senzer E.
Oil transport inside the oil control ring grove and its interaction with surrounding areas in internal combustion engines. Massachusetts Institute of Technology, PhD thesis, 2012.

[SPE 10] Spencer A., Almqvist A., Larsson R.
A numerical model to investigate the effect of honing angle on the hydrodynamic lubrication between a combustion engine piston ring and cylinder liner. *Proceedings of the Institution of Mechanical Engineers, Part J: Journal of Engineering Tribology*, vol. 225, 2010, p. 683-689.

[SPE 11] Spencer A. A. A. . L. R.
A semi-deterministic texture-roughness model of the piston ring-cylinder liner contact. *Proc. IMechE Part J: Journal of Engineering Tribology*, vol. 225, 2011, p. 325-333.

[STE 92] Stepina V., Vesely V.
Lubricants and special fluids. Elsevier, 1992.

[SUT 09] Sutaria B.M. Bhatt D. M. K.
Simulation and Modeling of Friction Force and Oil Film Thickness in Piston Ring Cylinder Liner Assembly of an I. C. Engine. *Proceedings of the World Congress on Engineering 2009 Vol II*, , 2009.

[TAK 06a] Takata R.
Effects of lubricant viscosity and surface texturing on ring-pack performance in Internal combustion engines. Massachusetts Institute of Technology, Master thesis, 2006.

[TAK 06b] Takata R., Li Y., Wong V.
Effects of liner surface texturing on ring/liner friction in large bore IC engines. *ICEF2006-1525 paper,Proceedings of ICEF06, ASME Internal Combustion Engine Division 2006 Fall Technical Conference Sacramento, California, November 5-8, 2006.*, , 2006.

[TAY 93] Taylor C.
Engine Tribology. Elsevier, 1993.

[THI 01] Thirouard B.
Characterization and modeling of the fundamental aspects of oil transport in the piston ring pack of internal combustion engines. Massachusetts Institute of Technology, PhD thesis, 2001.

[THI 03a] Thirouard B., Tian T.
Oil Transport in the Piston Ring Pack (Part I): Identification and Characterization of the Main Oil Transport Routes and Mechanisms. rapport, 2003, SAE Technical Paper.

[THI 03b] Thirouard B., Tian T.
Oil Transport in the Piston Ring Pack (Part II): Zone Analysis and Macro Oil Transport Model. rapport, 2003, SAE Technical Paper.

[TIA 97] Tian T.
Modeling the performance of piston ring pack in internal combustion engines. Massachusetts Institute of Technology, PhD thesis, 1997.

[TIA 00] Tian T., Wong V.
Modeling the lubricaton, dynamics, and effects of piston dynamic tilt of twin land oil control rings in internal combustion engines. *Trans. ASME, Journal of engineering for gas turbines and power*, vol. 122, 2000, p. 119-129.

[TIA 02a] Tian T.
Dynamic behaviours of piston rings and their practical impact. Part 1: ring flutter and ring collapse and their effects on gas flow and oil transport. *Proc. IMechE Part J: Journal of Engineering Tribology*, vol. 216,, 2002, p. 209-227.

[TIA 02b] Tian T.
Dynamic behaviours of piston rings and their practical impact. Part 2: oil transport, friction, and wear of ring/liner interface and the effects of piston and ring dynamics. *Proc. IMechE Part J: Journal of Engineering Tribology*, vol. 216, 2002, p. 229-247.

[TOM 01] Tomanik E., Nigro F.
Piston ring pack and cylinder wear modelling. *SAE Techncal Paper 2001-01-0572*, , 2001.

[TOM 03] Tomanik E., Chacon H., Teixeira G.
A simple numerical procedure to calculate the input data of Greenwood-Williamson model of asperity contact for actual engineering surfaces. *Tribology Series*, vol. 41, 2003, p. 205-215.

[TOM 08] Tomanik E.
Friction and wear bench tests of different engine liner surface finishes. *Tribology International*, vol. 41, 2008, p. 1032-1038.

[TOM 13] Tomanik E.
Modelling the hydrodynamic support of cylinder bore and piston rings with laser textured surfaces. *Tribology international*, vol. 59, 2013, p. 90-96.

[TOW 83] Tower B.
First report on friction experiments. *Proceedings of the institution of mechanical engineers*, vol. 34, n° 1, 1883, p. 632–659, SAGE Publications.

[VEN 00] Venner C., Lubrecht A.
MultiLevel Methods in Lubrication, vol. 37. Elsevier Tribology Series,, 2000.

[VIC 06] Vicente J. d., Stokes J., Spikes H.
Rolling and sliding friction in compliant, lubricated contact. *Proc. IMechE Part J: Journal of Engineering Tribology*, vol. 220, 2006, p. 55-63.

[VIN 08] Vincent C., Monteil G., Barriere T., Gelin J. C.
Control of the quality of laser surface texturing. *Microsystem Technologies*, vol. 14, n° 9-11, 2008, p. 1553–1557, Springer.

[VOK 04] Vokac A.
An experimental study of the oil evolution in critical piston ring pack regions and the effects of piston ring designs in internal combustion engine utilizing two dimensional laser induces fluorescence and the impact on maritim ecomnomics. Massachusetts Institute of Technology, Master thesis, 2004.

[WAK 92] Wakuri Y., Hamatake T., M. S., Kitahara T.
Piston ring friction in internal combustion engine. *Tribology international*, vol. 25, 1992, p. 299-307.

[WON 07] Wong V., Tian T., Smedley G., Moughon L., Takata R., Jocsak J., Stanglmaier R., Bestor T., Defoort M., Quillen K., Evans K.
Low engine friction technology for advanced natural gas reciprocating engines. Massachusetts Institute of Technology, 2007.

[WU 01] Wu J.
The properties of aspereties of real surfaces. *Transaction ef the ASME, Journal of Tribology*, vol. 123, 2001, p. 872-883.

[YIL 03] Yilmaz E.
Sources and characteristics of oil consumption in a spark-ignition engine. Massachusetts Institute of Technology, PhD thesis, 2003.

[YUA 11] Yuan S., Huang W., Wang X.
Orientation effects of micro-grooves on sliding surfaces. *Tribology International*, vol. 44(9), 2011, p. 1047-1054.

Appendix A

Reynolds equation derivation

This appendix details how the Reynolds equation is derived for both the parabolic and the flat ring.

Generalised Reynold equation

The Reynolds equation is based on the thin film assumption between two moving surfaces 1 and 2. An elementary volume between these surfaces is considered. Figure A.1 (a) shows the coordinate system x, y, z and the velocity for both surfaces 1 and 2, respectively U_1, V_1, W_1 and U_2, V_2, W_2.

Using the definition of the viscosity η, the pressure gradient for x reads

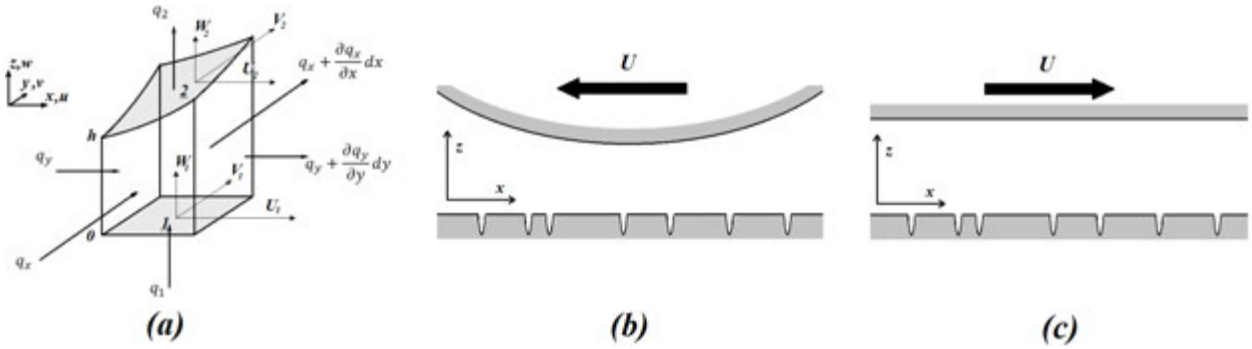

Figure A.1: *(a) An elementary fluid volume (b) Parabolic ring sliding direction (c) Flat ring sliding direction*

$$\frac{\partial p}{\partial x} = \eta \frac{\partial^2 u}{\partial z^2} \tag{A.1}$$

The integration with respect to z gives

$$u = \frac{1}{\eta}\frac{\partial p}{\partial x}\frac{z^2}{2} + C_1 z + C_2 \tag{A.2}$$

where C_1 and C_2 are determined using boundary conditions

$$C_1 = \frac{1}{\eta}\frac{\partial p}{\partial x}\frac{h}{2} + \frac{U_2 - U_1}{h} \quad \text{and} \quad \mathrm{C_2 = U_1} \tag{A.3}$$

Thus

$$u = \frac{-1}{2\eta}\frac{\partial p}{\partial x}(hz - z^2) + U_1 + \frac{z}{h}(U_2 - U_1) \tag{A.4}$$

By the same way

$$v = \frac{-1}{2\eta}\frac{\partial p}{\partial y}(hz - z^2) + V_1 + \frac{z}{h}(V_2 - V_1) \tag{A.5}$$

The different volume flows read

$$q_x = \int_0^h u\, dydz = \frac{-h^3}{12\eta}\frac{\partial p}{\partial x}dy + \frac{U_2 + U_1}{2}hdy \tag{A.6}$$

$$q_y = \int_0^h v\, dxdz = \frac{-h^3}{12\eta}\frac{\partial p}{\partial y}dx + \frac{V_2 + V_1}{2}hdx \tag{A.7}$$

$$q_1 = W_1 dxdy \tag{A.8}$$

$$q_2 = W_2 dxdy - U_2\frac{\partial h}{\partial x}dxdy - V_2\frac{\partial h}{\partial y}dxdy - \frac{\partial h}{\partial t}dxdy \tag{A.9}$$

Equalling the entering flows with the exiting ones, one obtains the generalized form of the Reynolds equation

$$\begin{aligned} W_1 - W_2 = &-\frac{1}{12\eta}\frac{\partial}{\partial x}\big(h^3\frac{\partial p}{\partial x}\big) - \frac{1}{12\eta}\frac{\partial}{\partial y}\big(h^3\frac{\partial p}{\partial y}\big) \\ &+ \frac{U_2 + U_1}{2}\frac{\partial h}{\partial x} + \frac{V_2 + V_1}{2}\frac{\partial h}{\partial y} \\ &+ \frac{h}{2}\frac{\partial}{\partial y}(V_2 + V_1) + \frac{h}{2}\frac{\partial}{\partial x}(U_2 + U_1) - \frac{\partial h}{\partial t} \end{aligned} \tag{A.10}$$

Reynold equation for the parabolic ring

Figure A.1 (b) shows the parabolic ring and its sliding direction x (it means that $W_1 = W_2 = V_1 = V_2 = 0$). The liner is motionless, and the ring is moving in the decreasing x direction. The velocity of the ring is noted U. One obtains $U_2 = -U$. Thus

$$\frac{U_2 + U_1}{2} = \frac{-U + 0}{2} = -U_m \tag{A.11}$$

Considering that the velocity U is constant, the Reynolds equation is reduced to

$$\frac{1}{12\eta}\frac{\partial}{\partial x}\big(\frac{h^3\partial p}{\partial x}\big) + \frac{1}{12\eta}\frac{\partial}{\partial y}\big(\frac{h^3\partial p}{\partial y}\big) = -U_m\frac{\partial h}{\partial x} + \frac{\partial h}{\partial t} \tag{A.12}$$

The film thickness h is written according to the fixed frame related to the liner (motionless). It reads

$$h(x,t) = h_0(t) + \frac{(x + Ut)^2}{2R_x} + R(x) = h_0(t) + \frac{x^2}{2R_x} + \frac{U^2t^2}{2R_x} + \frac{xUt}{R_x} + R(x) \tag{A.13}$$

The Couette term becomes

$$-U_m\frac{\partial h}{\partial x} = -U_m\frac{x}{R_x} - U_m\frac{Ut}{R_x} - U_m\frac{\partial R}{\partial x} \tag{A.14}$$

And the transient term becomes

$$\frac{\partial h}{\partial t} = \frac{\partial h_0}{\partial t} + \frac{U^2 t}{R_x} + \frac{xU}{R_x} \tag{A.15}$$

Adding these two terms leads to

$$-U_m\frac{\partial h}{\partial x} + \frac{\partial h}{\partial t} = U_m\frac{x}{R_x} + U_m\frac{Ut}{R_x} - U_m\frac{\partial R}{\partial x} + \frac{\partial h_0}{\partial t} \tag{A.16}$$

One can re-write Equation A.16 according to a frame that is fixed to the moving ring. The variable x is changed to x_1 according to the following relation

$$x = x_1 - Ut \tag{A.17}$$

Knowing that $\partial x = \partial x_1$, Equation A.16 becomes

$$-U_m\frac{\partial h}{\partial x} + \frac{\partial h}{\partial t} = U_m\frac{x_1}{R_x} + \frac{\partial h_0}{\partial t} - U_m\frac{\partial R}{\partial x} \tag{A.18}$$

The velocity can be expressed

$$U = -\frac{\partial x}{\partial t} \tag{A.19}$$

Thus

$$U\frac{\partial R}{\partial x} + \frac{\partial R}{\partial t} = 0 \tag{A.20}$$

Consequently

$$U_m\frac{\partial R}{\partial x} + \frac{\partial R}{\partial t} = -U_m\frac{\partial R}{\partial x} \tag{A.21}$$

Equation A.18 becomes

$$-U_m\frac{\partial h}{\partial x} + \frac{\partial h}{\partial t} = U_m\frac{x_1}{R_x} + \frac{\partial h_0}{\partial t} + U_m\frac{\partial R}{\partial x} + \frac{\partial R}{\partial t} \tag{A.22}$$

The film thickness reads

$$h(x_1, t) = h_0(t) + \frac{x_1^2}{2R_x} + R(x_1, t) \tag{A.23}$$

and

$$U_m\frac{\partial h}{\partial x} = U_m\frac{x_1}{R_x} + U_m\frac{\partial R}{\partial x} \;\; and \;\; \frac{\partial h}{\partial t} = \frac{\partial h_0}{\partial t} + \frac{\partial R}{\partial t} \tag{A.24}$$

Finally the Reynolds equation reads

$$\frac{1}{12\eta}\frac{\partial}{\partial x}\big(h^3\frac{\partial p}{\partial x}\big) + \frac{1}{12\eta}\frac{\partial}{\partial y}\big(h^3\frac{\partial p}{\partial y}\big) = U_m\frac{\partial h}{\partial x} + \frac{\partial h}{\partial t} \tag{A.25}$$

Reynolds equation for the flat ring

Figure A.1 (c) shows the flat ring and its sliding direction. Similar to the parabolic case $W_1 = W_2 = V_1 = V_2 = 0$. However, $U_2 = U$. The film thickness reads

$$h(x, t) = h_0(t) + R(x) \tag{A.26}$$

Thus the Reynolds equation reads

$$\frac{1}{12\eta}\frac{\partial}{\partial x}\big(h^3\frac{\partial p}{\partial x}\big) + \frac{1}{12\eta}\frac{\partial}{\partial y}\big(h^3\frac{\partial p}{\partial y}\big) = U_m\frac{\partial h}{\partial x} + \frac{\partial h_0}{\partial t} \tag{A.27}$$

Appendix B

Numerical solutions and pre-relaxation operator

This appendix details some of the numerical solutions to converge or to enhance the convergence speed for the PRCL Multigrid solver.
An example of a flat ring - grooved liner is shown in this appendix. The analytical model of Chapter 2 is used. The solution for a 1/10 mesh size is shown in Figure B.1. The pressure is generated by the grooves, its profile is shown in this figure through colors, the shape corresponding to the roughness profile. The multigrid solver was used. A four grid successive

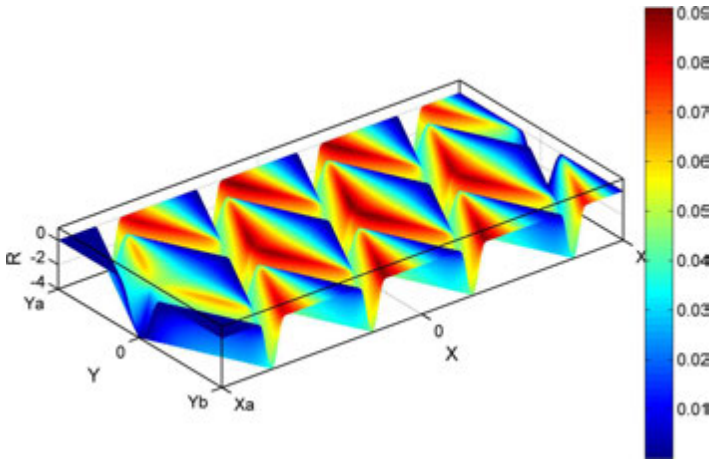

Figure B.1: *Dimensionless pressure profile on a grooved analytical surface (colormap) for a flat ring with* $N = 4$, $\alpha = 25$ *and* $A = 4$.

V(4,2)-cycle scheme is used. Some improvements were made since there are several obstacles to overcome. The convergence is altered near the cavitation zone. The solution used by Venner and Lubrecht [VEN00] was to introduce local point relaxations in this particular zone before performing each of the global relaxations sweeps. These local point relaxations are called pre-relaxations. Figure B.2 shows the mean residual for each performed V-cycle. The top curve is the one with these pre-relaxations. The residual is blocked at a certain level, the convergence failed. Figure B.3(a) shows the residual over the entire surface. It is clear that there is an additional convergence problem inside the grooves. In fact, the coarse grid introduced errors when interpolating at this location. One of the possible solutions is not

to interpolate (correct) inside the grooves and locally where the residual is relatively large. Figure B.2 shows that the second curve (from the top) is going to converge. It corresponds to the performed calculation with point pre-relaxation and with partial interpolation. Figure B.3 (b) shows clearly that the level of the residual is diminishing by a factor of 100, starting from the 7^{th} cycle where the partial interpolation is performed. The point relaxation can be

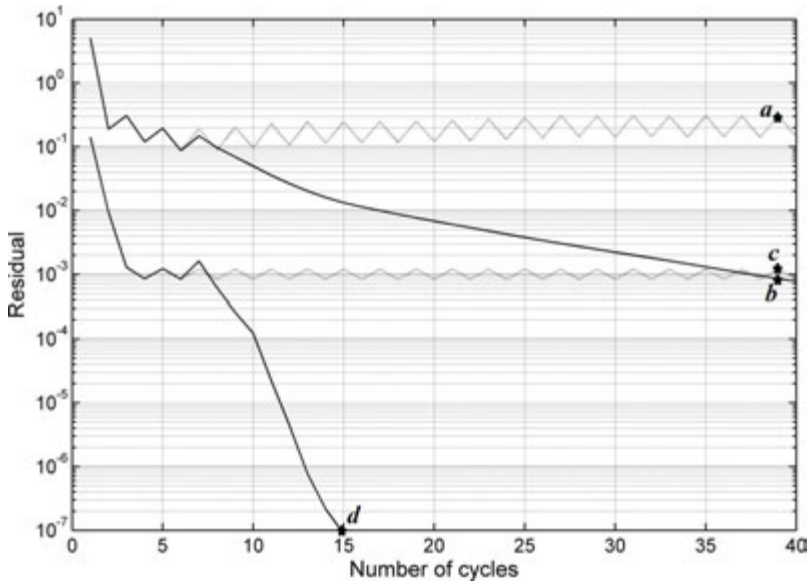

Figure B.2: *The mean residual as a function of the number of cycles, from bottom to top: block pre-relaxation + partial interpolation, block pre-relaxation + full interpolation , point pre-relaxation + partial interpolation and point pre-relaxation + full interpolation.*

replaced by the block relaxation (*cf.* line relaxation [VEN00]). The principle of the block relaxation method is simple: instead of relaxing point by point, one relaxes block by block. The whole block is solved at once by a direct method. In this work the LU decomposition is used as a direct solver. The block relaxation is more efficient than the point relaxation but it uses costly computing time and memory. This block relation is used for pre-relaxing. Blocks should be small (5×3 in this work) to ensure a reasonable computing time but sufficient to solve the problem. Figure B.2 shows that the block pre-relaxation diminishes the residual level and converges within a few cycles when using the partial interpolation. Figure B.3 (d) shows that the residual is relatively well distributed over the surface. This means that the local problems were overcome. The block pre-relaxation permit fast convergence regarding the number of cycles and regarding the work units, as defined in Chapter 2. The definition does not take into account the pre-relaxation which is reasonable when using the point relaxation. With the block relaxation, it has a cost and is unpredictable and is a function of the size of a single block, of the largest value of the residual, of the number of neighbouring points to the cavitation zone, of the number of points inside the grooves (or the highest slopes),... All this means that the computing time can, in some cases, be better for point pre-relaxation than for the block pre-relaxation (not in the case studied in this appendix), but for robustness purposes the block relaxation is always used.

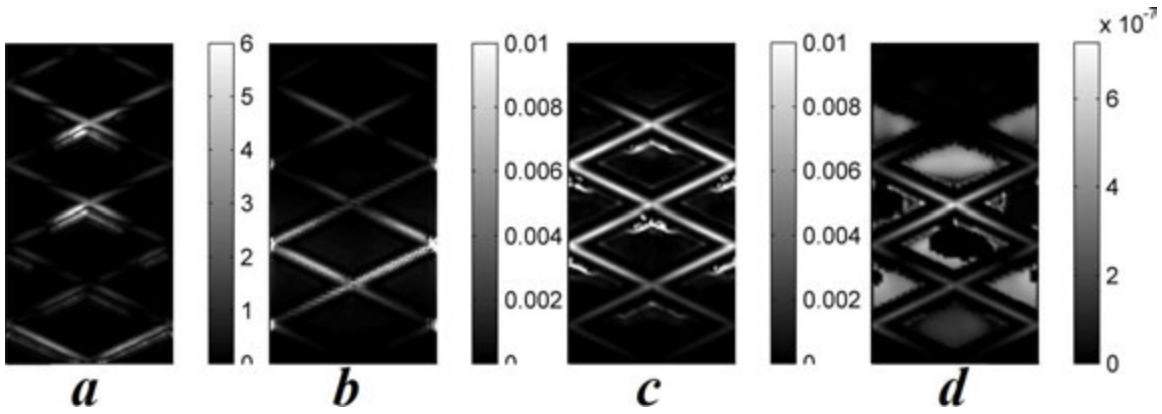

Figure B.3: *Residual profile at the end of the calculations (a) point pre-relaxation + partial interpolation (b) point pre-relaxation + full interpolation (c) block pre-relaxation + partial interpolation (d) block pre-relaxation + full interpolation*

Appendix C

The single parameter Δ

This appendix details how the single parameter Δ is derived.
The objective of the parameter Δ is to regroup both the groove density ϵ and the groove depth A in one single parameter with

$$\Delta = f(A) \times g(\epsilon) \tag{C.1}$$

The effect of the groove depth is analysed in this paragraph, independently of its density (which regroups three parameters that are D_1, Λ and α). For this purpose, a 1D groove is considered with a unit width (Figure C.1). The expression of this groove is

$$R(x) = -\frac{A}{2}(1 + \cos(2\pi x)) \tag{C.2}$$

The effect of this groove is compared with the smooth case. The film thickness for the

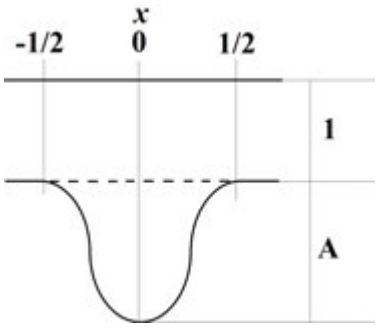

Figure C.1: *Unit groove*

grooved case reads

$$H(x) = 1 + \frac{A}{2}(1 + \cos(2\pi x)) \tag{C.3}$$

and for the smooth case

$$H(x) = 1 \tag{C.4}$$

The terms in H^3 in the Reynolds equation indicate the conductivity of the contact in term of Poiseuille flow. Thus, the inverse of this value is the resistance that the geometry opposes

to this flow, noted R^*. To compare the groove to the smooth case, the local resistance is integrated for x from -1/2 to 1/2. For the grooved case

$$R^* = \int_{-1/2}^{1/2} \frac{1}{H^3} dx = \int_{-1/2}^{1/2} \frac{1}{\left[1 + A(1 + \cos(2\pi x))/2\right]^3} dx \tag{C.5}$$

This integration leads to

$$R^* = \frac{1 + A + 3A^2/8}{(1 + A)^{5/2}} \tag{C.6}$$

And for the smooth case

$$R^*_{smooth} = \int_{-/2}^{1/2} \frac{1}{H^3} dx = \int_{-1/2}^{1/2} \frac{1}{\left[1\right]^3} dx = 1 \tag{C.7}$$

Finally

$$R^*/R^*_{smooth} = \frac{1 + A + 3A^2/8}{(1 + A)^{5/2}} \tag{C.8}$$

Assuming that $f(A) = R^*/R^*_{smooth}$, $g(\epsilon)$ ($cf.$ Equation C.2) is determined by looking for a function that decreases when the density increases. In fact, knowing that very dense grooves and very deep grooves have almost the same effect on load carrying capacity, the value of Δ must be nearly the same for both cases (dense and deep). Equation C.8 shows that when A is increasing Δ decreases. This explains why g has to be a decreasing function. In addition to the decreasing requirement, g has to ensure that the result (LCC as a function of Δ) is not sparse nor scattered. In other words, two given calculated LCC's, of approximatively the same Δ, have to be as close as possible one to each other.
The function $-\log$ fits these requirements. The expression of Δ is

$$\Delta = -\log(\epsilon) \frac{1 + A + 3A^2/8}{(1 + A)^{5/2}} \tag{C.9}$$

Figure C.2 shows Δ as a function of ϵ and A. For deep grooves ($A > 10$) Δ is small, for dense grooves ($\epsilon > 0.8$), Δ is also small. The deep grooves and the dense grooves give the same order of magnitude of Δ. Δ increases when the groove depth decreases and when the density decreases. For very sparse grooves and for very shallow grooves, Δ is large. This meets the idea that those types of grooves have the same behaviour and does not influence much the LCC.

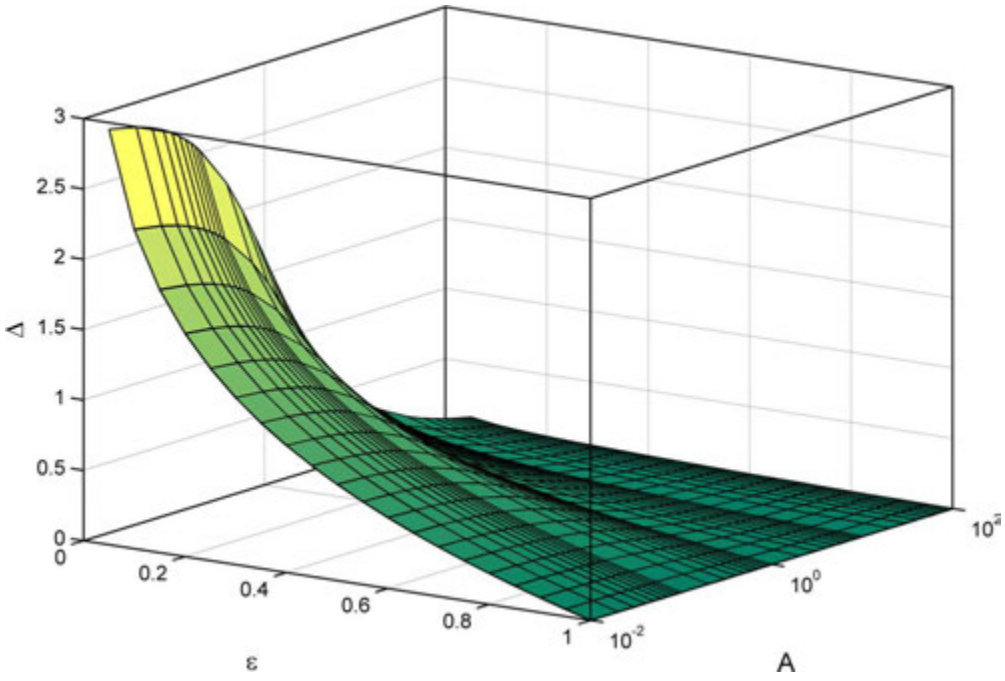

Figure C.2: Δ *as a function of* ϵ *and* A

List of Figures

List of Tables

FOLIO ADMINISTRATIF

THESE SOUTENUE DEVANT L'INSTITUT NATIONAL DES SCIENCES APPLIQUEES DE LYON

NOM : BOUASSIDA DATE de SOUTENANCE : 16 Septembre 2014

Prénoms : HAFEDH

TITRE :
LUBRICATED PISTON RING CYLINDER LINER CONTACT : INFLUENCE OF THE LINER MICROGEOMETRY

NATURE : Doctorat Numéro d'ordre : 2014ISAL0088

Ecole doctorale : MEGA

Spécialité : Mécanique - Génie Mécanique – Génie Civil

RESUME :
La microgéométrie de la surface de la chemise joue un rôle très important dans les pertes par frottement et dans la consommation de l'huile dans un moteur à combustion interne. Une des texturations classiques de cette surface est celle créée par pierrage. Elle se compose de plateaux plus ou moins lisses et de profondes stries croisées. L''épaisseur du film d'huile est influencée fortement par cette texturation.
Un modèle simplifié du contact segment chemise a été créé en la présence de la microgéométrie.
Puis, un code de calcul basé sur la méthode numérique multigrille a été développé. Ce code a été utilisé pour des études paramétriques avec des jeux de paramètres très variés. Les calculs quantifient l'influence de cette microgéométrie particulière sur la relation film d'huile - portance.
Les résultats mettent en évidence deux mécanismes distincts de génération de portance selon le type du segment. Le segment parabolique porte par son convergent et les stries ne font que diminuer cette portance. Inversement, le segment plat ne porte pas et ce sont les stries qui génèrent la portance. Deux modèles de prédiction ont finalement été déduits, un pour les segments paraboliques et un pour les segments plats. Ces deux prédictions ont ensuite été validées par des calculs sur des surfaces mesurées

MOTS-CLES : Texturation, lubrification hydrodynamique, contact segment-chemise, prédiction

Laboratoire (s) de recherche :
Laboratoire de Mécanique des Contacts et des Structures - INSA de Lyon.
LaMCoS - UMR CNRS 5514 - INSA de Lyon
20, avenue Albert Einstein, 69621 Villeurbanne Cedex (FRANCE)

Directeur de thèse: Professeur A.A. LUBRECHT

Président de jury :

Composition du jury :
MAZUYER Denis
MONTEIL Guy
FILLON Michel
TIAN Tian
LUBRECHT Antonius A.
CHARLES Pierre
BIBOULET Nans